Gold Nanoparticle & Photodynamic Therapy Use in

Oropharyngeal Cancer

Thesis submitted in accordance with the requirements of the

University of Liverpool

for the degree of Master's in Philosophy in Cancer Medicine by

Matthew Zammit

June 2023

Supervisors: Mr. Jason Fleming, Dr. Martin Volk

TABLE OF CONTENTS

TABLE OF FIGURES

TABLES

ACKNOWLEDGEMENTS

I want to express my sincere gratitude to everyone who has offered their assistance and support to me throughout my MPhil. Despite its ups and downs, this project has been incredibly fulfilling.

Throughout this journey, my supervisors have been tremendous. Jason presented me with this exciting opportunity to dive into nanomedicine, whilst mentoring me throughout my research and clinical journeys during the past few years. Martin provided me with an indescribable amount of support, time, and patience. It has been a privilege to work for two distinguished academicians at the University of Liverpool and I will do my best to live up to the high standards they have established.

Other members of the Volk group have also helped me throughout the project. Matthew Broadbent was especially helpful in showing me the ropes of nanoparticle synthesis, taking me through different lab-based techniques at the very start of it all. Further special thanks to Harriet, Ellie and Matt Ryan who also contributed to the direction of the project.

The project involved an extensive collaboration between the chemistry and biology departments. I would like to thank Mathias Brust and Jason Parsons for their time to discuss several key issues, as well as Maria, Johnny, Sam and Marta for their guidance and support in the biology and chemistry laboratories.

I'm grateful for my family's unending support and inspiration, including my mum, dad & brother (all the way from Malta!). Special thanks to my son Ethan for always making me laugh and sing, and to my wife Nicola for being my rock and cheerleader when results were not going my way.

LIST OF ABBREVIATIONS

Au/ Au^{3+} – Gold/ Gold ion

AuNP – Gold Nanoparticle

COOH-PEG7-COOH - Poly(ethyelene Glycol) Bis (Carboxylmethyl) Ether

CMS – Cell Membrane Stability

CRT – Chemoradiotherapy

DAMPS - Damage-Associated Molecular Patterns

DCS – Differential Centrifugal Sedimentation

EDC – 1-ethyl-3(3-dimethylaminopropyl) carbodiimide

Glc-NP – Glycosylated Nanoparticle

GLUT – Glucose transporter

HNSCC – Head & Neck Squamous Cell Carcinoma

HPV – Human Papilloma Virus

I_2/KI – Iodine/ Potassium Iodide Solution (etchant)

I_2:Au – Iodine to Gold molecule ratio

ICP-MS - Inductively Coupled Mass Spectroscopy

ICP-OES - Inductively Coupled Plasma Optical Emission Spectroscopy

LSPR - Localised surface plasmon resonance

MES - 2-[morpholino]ethanesulfonic acid

MTT – 3-(4,5-dimethylthiazol-2-yl)-2,5-diphenyltetrazolium bromide

NP – Nanoparticle

OPSCC – Orophrayngeal squamous cell cancer

PAH – Polyallylamine Hydrochloride

PDT – Photodynamic Therapy

PEG - Polyethylene glycol

PEG_5-OH – reference to PEGylated compound with chemical structure $HS-PEG_5-OH$

PEG_6-NH_2 - reference to PEGylated compound with chemical structure $HS-PEG_6-NH_2$

PEG-NP – Gold Nanoparticle with PEGylated capping layer

POCRT – Post-Operative Chemoradiotherapy

PSA – Photosensitising Agent

PSS – sodium Polystyrene Sulfonate

RB- Rose Bengal

RCV – Relative Cell Viability

RMS – Relative Membrane Stability

s-NHS – N-hydroxysulfosuccinimide

UV-vis – Ultra-Violet Visible Spectroscopy

ABSTRACT

Oropharyngeal squamous cell carcinoma (OPSCC) is a debilitating cancer with two evolving patient cohorts: a young & fitter human papilloma virus (HPV) positive subgroup and a more co-morbid HPV negative sub-group. This has raised questions over the current universal treatment strategy for this head and neck cancer, with concerns of over- & under-treating the two cohorts respectively.

This project proposes a targeted vector for photodynamic therapy (PDT) in OPSCCs, accessible through topical application. This may serve as an adjunct to current OPSCC treatment, allowing for treatment descalation or escalation, depending on HPV-subtype. Whilst PDT has been used in clinical trials for head and neck cancer, it lacked specificity. The project explores nanoparticle (NP)- directed PDT as a means of improving specificity.

An initial literature review explored glycosylation as a candidate for NP targeting. The review provided recommendations for structural features and configurations of the conjugating glucose moiety to improve cellular uptake. Proof of NP-mediated receptor endocytosis after glucose-receptor attachment was also illustrated in the review.

A gold NP structure incorporating Rose Bengal (an essential component for PDT) was initially considered for glycosylation. However, an alternative PEGylated approach for synthesising a glycosylated AuNP (Glc-NP) was proposed for this thesis, hypothesised to give a more streamlined chemical structure. A synthesis technique was developed and optimised, introducing Tween-20 to help prevent NP aggregation and loss of NPs during the cleaning process. This displayed encouraging characterisation results from Ultra-violet visible spectroscopy and differential centrifugation sedimentation. A persistent absorbance band and gradual increase in the NP's shell thickness was highly suggestive of NP glycosylation.

To maximise its cytotoxic effect by PDT, Glc-NPs must be internalized into cancer cells as opposed to simply adsorbing to the cell membrane.
To objectively distinguish NP cellular internalisation from cell surface adsorption, an iodine etching process was developed. The iodine system was scrutinized as a gold etchant at millimolar & micromolar concentrations, confirming its etching capacity within a 5-minute interval to reduce its cytotoxicity impact. The toxicity profile for the iodine solution was also re-affirmed with two separate techniques: MTT assay (cell's metabolic activity) and trypan blue experiment (cell membrane stability) on different cell lines. This led to a protocol whereby cell dishes were incubated in a 0.085mM I_2/KI solution for 5 minutes to etch away NPs adsorbed to the cell surface. This was successfully verified in uptake experiments in HeLa & 74A cell lines.

Quantification of Glc-NP uptake was attempted on HeLa & 74A cell lines. Whilst further characterisation of this pathway is required, non-specific Glc-NP uptake was not witnessed. This project has led to a more rigid quantification protocol for improved Glc-NP synthesis protocol & uptake experiments. The current Glc-NP models provides a tumour-selective carrier for the future addition of Rose Bengal to the complex, functionalizing this Glc-NP for PDT.

CHAPTER 1: INTRODUCTION TO OROPHARYNGEAL CANCER & NANOPARTICLE-DIRECTED THERAPY

1.1 BACKGROUND ON OROPHARYNGEAL CANCER

1.1.1 OROPHARYNGEAL CANCER IN ENGLAND & MERSEYSIDE

Head and neck squamous cell carcinoma (HNSCC) is one of the most debilitating cancers present worldwide, due to its historically poor survival rates and negative impact on quality of life.(1,2) The recent increase in HNSCC rates in England is due to the oropharyngeal squamous cell cancer (OPSCC) human papilloma virus (HPV) subtype, accounting for 70% of newly diagnosed OPSCC cases.(2–5) Over a 10 year period, the age-stratified OPSCC incidence in England increased by 60%, from 0.5 (2009) to 0.8 (2019) per 100,000 people.(6) A 40% HNSCC rise (1998-2011) in the Mersey and Cheshire regions was recognised by the UK Cancer Information Services, with Liverpool having a higher than average HNSCC prevalence and mortality rate. Liverpool's peak incidence rate rivals those of India, South Africa, and certain provinces of South America.(1)

Current oncological treatment can result in significant morbidity to a patient's appearance, as well as their ability to speak and swallow. This suggests that novel treatment approaches are urgently required, especially given a lack of further advances in treatment outcomes in recent years.(2–6) The HPV-positive sub-group distinguishes itself from its negative counterpart as it affects a younger, healthier population and has better prognostic outcomes.(3,4) This is a sharp contrast from the previous older, morbid patient group (re-classified as the HPV-negative sub-group) and it has led to a revaluation of current treatment trajectories. De-escalated therapy for OPSCC HPV positive subtypes have gained traction in the medical research field.(4)

The rise in OPSCC incidence, especially in Merseyside, and the need for reconsideration of treatment strategies makes it an ideal disease model for this research project. However, OPSCC's main selling point is its accessibility of oropharyngeal subsites through trans-oral

exposure. This offers a unique possibility of topically applied therapy, serving as a prospective disease model to study within the context of targeted treatments.

The development of OPSCC treatment modalities is summarised in section 1.1.2. This provides a better understanding why photodynamic therapy (PDT) was selected as a potential treatment adjunct for investigation (section 1.2.1).

1.1.2 EVOLUTION OF OPSCC TREATMENT STRATEGIES

OPSCC treatment strategies with a curative-intent typically have a small therapeutic window between preserving cure rates and mitigating adverse effects. OPSCC management has evolved throughout the past decade, from 'aggressive' traditional surgery to more 'targeted' organ preservation strategies.(7)

Radiotherapy, with/ without concurrent chemotherapy (CRT) became a gold standard treatment for head and neck cancer in 1994, following the Veterans Affair study on advanced laryngeal malignancies.(8) The trial witnessed similar loco-regional disease control rates between CRT and radical surgery.(9) The former was preferred over traditional surgical interventions due to reduced rate of severe complications. Subsequently, CRT was trialled in OPSCC by the GORTEC group, where an increased 6.6% survival benefit was seen with additional chemotherapy use.(10) Optimisation strategies in radiotherapy lead to the development of intensity-modulated radiotherapy; narrowing the targeted field and reducing the dose to normal surrounding physiological tissue.(8)

However, CRT still presents short-term complications (such as mucositis and skin reactions) and long-term morbidity due to dysphagia, laryngeal scarring, and a potential tracheostomy requirement.(2) These are severely debilitating with quality-of-life studies highlighting swallowing dysfunction as the main culprit.(11) Trans-oral surgery has emerged as a further alternative to traditional approaches and CRT in early staged cancers. Trans-oral LASER and trans-oral robotic surgery have matched loco-regional control rates when compared with traditional open surgery, whilst maintaining improved functional outcomes compared to CRT. (12)

Standard of care management is based on Tumour, Node and Metastasis staging (TNM), together with patient's preferences, past medical history, and surgical facilities.(2,8) Early staged disease is treated with single modality treatment (radiotherapy or surgery), whilst most patients tend to require multi-modality treatment in more advanced malignancies. A local study reaffirms this, identifying 84.3% (129/153) of patients requiring radiotherapy alone or CRT.(5) Common indicators for post-operative CRT (POCRT) include staging of disease, perineural invasion and extra-capsular spread in related nodal disease.(7) POCRT has demonstrated improved loco-regional control, disease-free and overall survival in OPSCC patients through landmark studies RTOG 9501 and EORTC 22931.(13)

Despite differences in demographics and response to treatment, current recommended treatment guidelines do not distinguish between HPV subtypes.(4,8) The HPV-driven division of the OPSCC cohort has led to enquiries regarding a pathological driven treatment strategy. The rise in HPV positive OPSCC incidence resulted in studies and clinical trials de-escalating therapy for HPV-positive patients: the PATHOS trial within the UK & EU and the ECOG3311 study in the US.(5,8) In contrast, HPV negative OPSCC is being revised for upscaling of treatment protocols. This has faced several barriers, with treatment-related toxicity of CRT limiting intensification protocols, whilst surgical escalation failed to improve survival in a study by Kelly et al.(3) Photodynamic therapy (PDT) was considered in this research project as an adjunct to surgery in the OPSCC setting. This may serve as a de-escalation therapeutic option in HPV positive OPSCC, whilst intensifying treatment in the HPV negative cohort.

1.2 Photodynamic therapy

PDT is a minimally invasive therapeutic option that is gaining popularity in different aspects of biomedicine, including HNSCC treatment. It combines a triad of light, oxygen, and a photosensitising agent (PSA).(14) The therapy revolves around the activation of a PSA through the exposure of light at a particular wavelength. Activated PSA is excited to a temporary *'triplet state'*, subsequently transferring its energy to surrounding oxygen. This leads to the formation of singlet oxygen and other free radicals that are both cytotoxic and vasculotoxic. (15,16)

This chemical reaction is explained in further detail through the Jablonski diagram (figure 1.1).

A PSA in its ground state needs to be activated by specific wavelength illumination (coinciding with its own unique absorption spectrum). This is converted into an excited singlet state due to photon absorption; whereby one of its electrons is promoted to a higher energy level whilst in its same spin orientation. This typically lasts a few nanoseconds, transforming into a more stable triplet state via intersystem crossing (where the promoted electron is in the same spin orientation as the other unpaired electron). Within the microsecond time scale, it undergoes two reactions, both generating reactive oxygen species (ROS):

- Type I pathway: Triplet PSA reacts with nearby cellular components (e.g. plasma membrane) to form radical cation/ anions through the superoxide anion radical.
- Type II pathway: Direct energy transfer to ground-state triplet oxygen to generate the highly reactive singlet oxygen.

When the PSA is in either the excited singlet state or the triplet state, energy could be lost through fluorescence and phosphorescence, as demonstrated in figure 1.1.
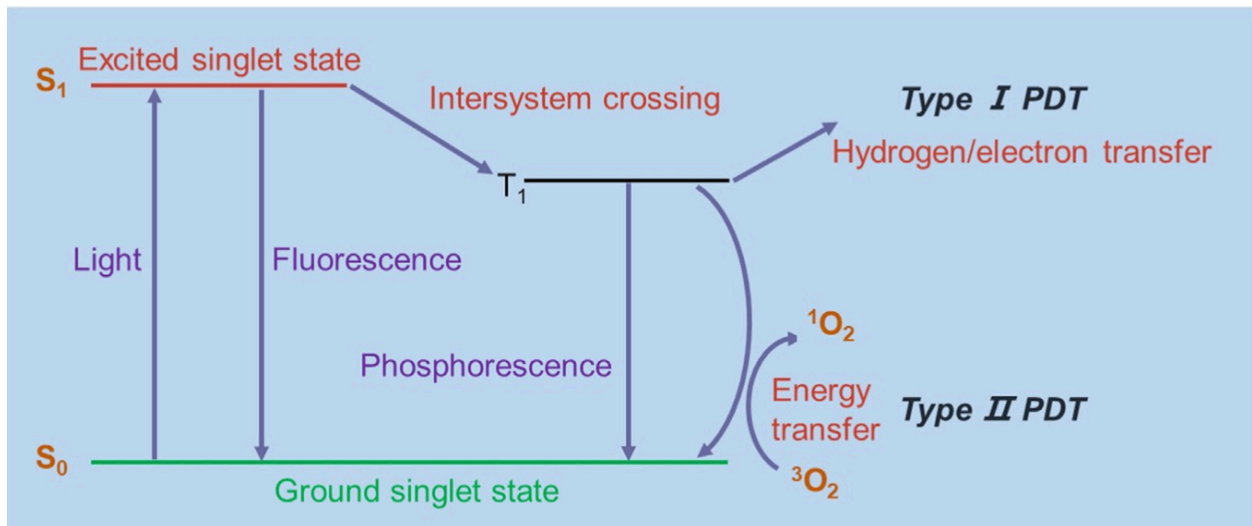
Figure 1.1: Photosensitisation Process, source Hu et al.(17)

Both pathways are dependent on surrounding oxygen concentrations and provide PDT with three anti-tumour mechanisms:(18)

1. Direct cellular death due to apoptotic, autophagic (regulated cell death) and necrotic (non-regulated) mechanisms

2. Indirect cellular insults through stimulation of a localised inflammatory reaction

3. Vascular damage

The role played by each anti-tumour mechanism is determined based on PSA's location in relation to the cancer cells. ROS generated have a short lifespan, with a confined action radius of approximately 100nm.(18,19) This is shorter than the typical length scale of cells, hence only cells containing PSA would be directly affected. Intracellular PSA can instigate cell death through different pathways, depending on the degree of injury inflicted, as well as the organelle/s damaged. Mitochondrial injury may trigger an apoptotic cascade, cell membrane insults instigate necrosis and lysosomic or endoplasmic reticulum targeting provokes autophagy. The degree of imbalance between ROS emergence and the cell's ability to recover from its injuries ultimately triggers different cell death pathways.(18)

Intracellular injuries provoke a strong extra-cellular inflammatory response. Both non-regulated and regulated cell death may release intracellular contents with inflammatory and immunomodulatory properties, known as damage-associated molecular patterns (DAMPs). These are recognised by immune cell receptors, building up a response to DAMPs in cancer cells, with a release of inflammatory mediators, lysosomal enzymes, and chemotactic factors.(18) ROS also damage endothelial cells lining the tumour's vasculature by activating clotting processes and blocking off vessels. (17)

These processes provide different routes for PDT's anti-tumorigenic response. As with every therapeutic option, PDT has its advantages and drawbacks. The upcoming sections review PDT's current progress in the head and neck cancer settings, drawbacks faced and how our proposal seeks to improve upon current PDT models.

1.2.1 PHOTODYNAMIC THERAPY IN THE HEAD & NECK SETTING

From the oncological aspect of medicine, PDT has been approved for clinical treatment of Barrett's oesophagus, oesophageal carcinoma and tracheobronchial carcinoma in the US, using aminolevulinic acid as a PSA.(14) This has been extended to the head and neck setting in Europe, with over 1,500 patients receiving PDT using several different PSAs for a range of various head & neck tumour pathologies.(20,21) This has been utilised as a:

1. Primary modality of curative treatment in early staged cancers

2. Adjuvant modality of curative treatment in attempts to ensure clear margins

3. Palliative treatment modality

The first multi-institutional phase II-III clinical trials evaluating PDT in head and neck cancer demonstrated efficacy in both palliative and early treatment setting. Foscan PDT in primary OPSCC achieved an 85% (97/114) complete response in Tis-T2 OPSCC. At their two-year follow-up, a 77% complete response and 75% disease-free survival was reported. This was comparable to conventional surgical procedures and had less adverse effects.(22) This is echoed in Schweitzer et al's study, utilising dihematoporphyrin (Photofrin)-mediated PDT, with 80% (24/30) patients) having complete remission on follow-up of treated Tis-T2 OPSCC).(21) Lambert et al. achieved similar results with meta-tetra(hydroxyphenyl)chlorin in their 26-patient cohort with oral and oropharyngeal SCC, confirming an immediate complete tumour response in 77%. The inclusion criteria for this study, however, were broader in terms of TNM staging, location of primary and included recurrent disease.(15) Regarding recurrent cancer therapy, only two of the 14 patients with recurrent SCC who had PDT as an intra-operative adjunct developed recurrence in an 11-year follow-up period.(15)

Such trials have further clarified and promoted use of PDT in treating early carcinomas with minimal morbidity and as an adjunct for surgical margins (especially in T3/T4 malignancies). Shortcomings commented on lack of PSA selectivity of cancer cells, photobleaching and low extinction coefficients.(14)

The current literature on PDT in HNSCC shows several advantages over current therapeutic options. In certain cancer stages (Tis-T2), it demonstrates similar response and disease-free survival rates to current surgical and CRT options. However, unlike surgery or CRT, PDT can be repeatedly administered to patients, even in an outpatient setting. The adverse effects of PDT, including generalised oedema and erythema at the site of treatment and mild scarring, are trivial when compared to the life-altering swallowing dysfunction and the other broad range of complications seen with surgery and CRT.

Despite these advantages, PDT has not yet been incorporated as one of our treatment options for HNSCC. The main drawbacks revolve around the limitations of light penetration depth and

PSA tumour specificity. Photo-conversion materials and x-rays without tissue penetration depth limitation are amongst some of the proposed options to resolve the light depth limitation.

However, PSA tumour-specificity is still an unsolved limitation. PSAs do not have a particular predilection for tumour cells and so their accumulation in tumour tissue is arbitrary, uncontrolled and relies on passive mechanisms for their uptake. They can also be taken up by nearby healthy tissue as well as systemically throughout the body when injected intravenously. This is further reflected in the study regimens displayed above. After PSAs were administered, patients were instructed to remain in a darkened room (light bulbs no brighter than 60W) and gradually return to unrestricted light exposure over two to four weeks.

Three generations of PSAs have been developed (summarised in table 1.2). Each generation seeks to improve upon its predecessor to attain the ideal characteristics of a PSA. These include room temperature stability, high photochemical reactivity, minimal cytotoxicity in the dark, easy solubility and high tumour selectivity.(23,24) Third generation PSAs have attempted to rectify the lack of selectivity, using second-generation PSAs attached to targeting moieties. This forms the basis of our research proposal.

PSA GENERATION	PSA EXAMPLE	GENERATIONAL PROPERTIES
FIRST	Photofrin (Sodium Porfirmer)	Low chemical purity, poor tissue penetration and increased risk of skin hypersensitivity
SECOND	Rose Bengal	Improved purity and tissue penetration, increased singlet oxygen production, low water solubility
THIRD	PSA combined with monoclonal antibodies	Combined 1st or 2nd Generation PSA with delivery systems to improve solubility and cellular selectivity

Table 1.1: Photosensitiser Agent Generations

1.3 RESEARCH PROPOSAL

We propose a third generation PSA, using nanoparticles (NPs) as targeting moieties/ delivery systems. The hypothesis combines current OPSCC treatment modalities with targeted PDT use as an adjuvant therapy. Figure 1.2 summarises this approach, with an
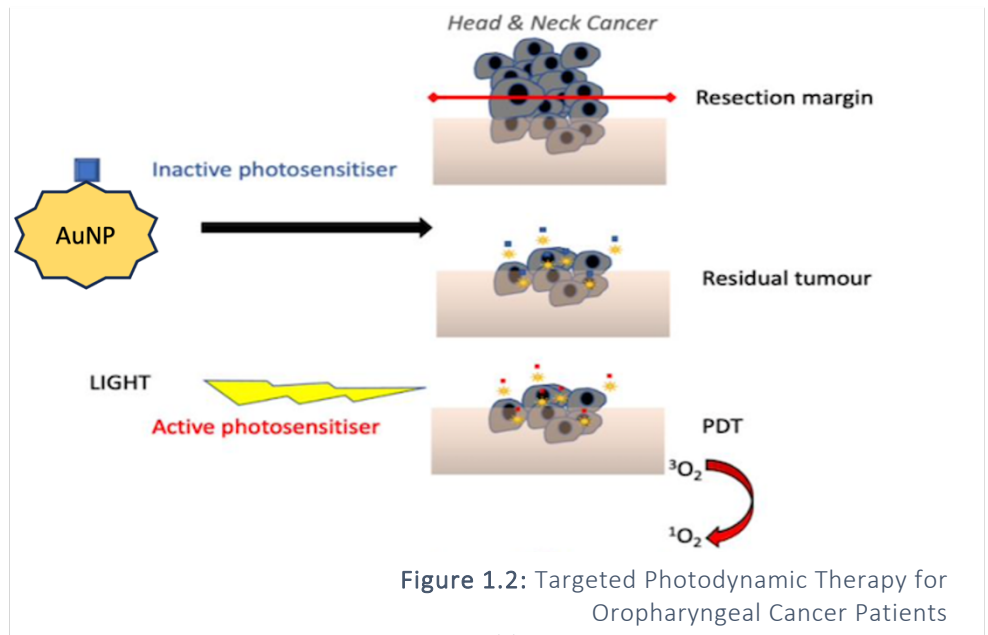
Figure 1.2: Targeted Photodynamic Therapy for Oropharyngeal Cancer Patients
abbreviations: AuNP- Gold Nanoparticle, PDT- Photodynamic therapy

initial resection margin attained with surgery (and/or chemoradiotherapy), follow by targeted PDT. The nanoparticle-PSA complex (NP-PSA) would act as a delivery system for PDT therapy.

However, without the inclusion of a targeting moiety, there is no expectation of cancer cell selectivity. This thesis seeks to exploit the increased number of glucose receptors in cancer cells as a potential targeting system, distinguishing them from nearby physiological cells. Section 1.4 discusses gold nanoparticles' (AuNP) physicochemical characteristics that lend them to be ideal vectors for PDT, whilst section 1.5 outlines the aims and objectives set to achieve the complex's selectivity through glucose ligands.

1.4 GOLD NANOPARTICLES AS A DELIVERY SYSTEM FOR PHOTODYNAMIC THERAPY

AuNPs have been widely considered in several fields of biomedicine, due to their favourable optical and chemical properties.(25,26) Faulk and Taylor introduced metal NPs into the field of medicine in 1970, whereby AuNPs showed superiority in diagnostic imaging techniques.(26) AuNPs are generally more stable than other NP core materials, being inert with a large electron density. Low background concentrations in natural aqueous environment and AuNPs' optical properties make them easy to quantify, locate and image in biological systems. Furthermore,

AuNP synthesis is now routine and well established within the literature.(27) There is a range of synthesis techniques, enabling precise customisation of size (less than 5% standard deviation of diameter), shape and surface functionalisation that dictates its biological properties *in vivo*.(24,28) The advantageous physicochemical aspects of AuNPs for PDT are further discussed below.

1.4.1 PHYSICAL ASPECTS OF AuNPS CONTRIBUTING TO PDT

Localised surface plasmon resonance (LSPR) is a fundamental optical feature that provides a better understanding of physical interactions on the nanoscale. When light's frequency is equivalent to the NP's inherent oscillation frequency, a uniform oscillation of free electrons across the NPs is seen.(29) This oscillation gives a specific absorption band, as predicted by Mie theory and is represented in figure 1.3.(30) It is also dependent on other factors, including shape (rod vs. spherical), temperature and interactions with its surrounding dielectric environment.(31) Through LSPR, AuNPs possess two effects:

1. Enhancement effect of the local electromagnetic field
2. Enhanced optical extinction coefficient
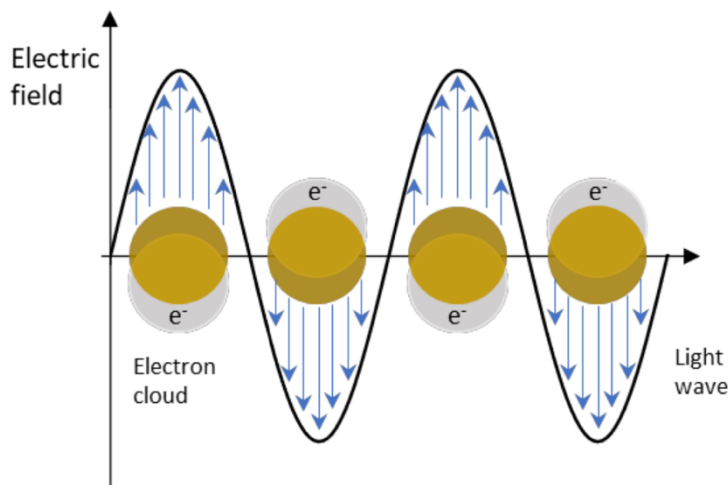
Figure 1.3: LSPR in AuNPs excited by light waves. Source: broadbent(24)

The first effect refers to AuNP's enhancement of the light electric field at the NP surface, its maximum represented by figure 1.3's peaks along the curvature. This may enhance spectral signals of substances near their surface and is referred to as surface enhancement. The

enhancement effect can be witnessed in diagnostic imaging techniques such as surface-enhanced Raman spectroscopy and fluorescence resonance energy transfer.(19)

Optical extinction coefficients for AuNPs can be maximised to be more than 10,000 times stronger than organic molecules when excited by light,(19) as seen with 15nm AuNPs, having an extinction coefficient of 3.6×10^8 $M^{-1}cm^{-1}$.(24,32) This characteristic that can be exploited in PDT and photothermal therapy.(19) Whilst citrate coated AuNPs have been shown to generate singlet oxygen when excited by light overlapping their LSPR band, this is an exceptionally small yield compared to other conventional PSAs (10^{-7} vs 0.89 for photofrin PSA).(24) However, AuNPs can promote the photosensitisation of any conjugated organic PSAs by transferring light energy to enhance singlet oxygen/ ROS production (whilst also directly producing singlet oxygen). This makes AuNPs ideal candidates for PSA delivery agents, improving upon PSA's photo-stability and efficiency of light energy conversion.(23)

1.4.2 CHEMICAL ASPECTS OF AuNPs CONTRIBUTING TO PDT

NPs characteristics, such as size, shape, surface functionalisation and charge directly affect their biocompatibility, cellular targeting, and drug delivery. Turkevich et al. introduced a controlled spherical AuNP synthesis technique by utilising a citrate reduction method in 1951. Citrate coated AuNPs of diameters between 5-120 nm are synthesised depending on reactant ratios and reaction times.(33) This prevents aggregation through the citrate ions' negatively charged coated layer for each AuNP and permits numerous conjugation strategies for ligands.(34) Unlike other NPs, AuNPs can form stable bonds with sulphur and nitrogen-containing groups, allowing for easy coupling with a wide range of biological ligands.(19) Given that the NPs' specific surface area is inversely proportional to their mass, NPs have a large customisable surface area, permitting different ligands to be attached, adding a further level of customisation.(35) The attachment of polyethylene glycol (PEG) may increase circulation half-life, HER2 & CCR5 ligands allow for active targeting of breast tumours and glycol-chitosan enhances uptake by immune cells to allow for detection of lymph node metastasis. In PDT, AuNPs may disperse hydrophobic PSAs in aqueous solutions and target cells through the attachment of other biological ligands onto its surface.(19)

When in contact with cell media and serum, NPs' chemical properties determine their adherence to proteins and lipids, forming a 'corona' structure. This dynamic structure is constantly in flux, with changes in composition until an equilibrium is reached (Vroman effect).(36) A NP-PSA complex may improve the PSA's circulation time, bioavailability, and uptake through its interactions with the protein corona.(19)

1.4.3 GOLD NANOPARTICLE CELL ENTRY MECHANISMS

Cell entry for NPs can be broadly divided into direct and pinocytosis-based uptake. Direct translocation avoids endosomal entrapment, whereby small sized NPs may directly diffuse through plasma membranes, observed for 2-4nm AuNPs in HeLa cells.(37) Pinocytosis is the commonest method for NP uptake in most cells, referring to ingestion of extra-cellular material via invagination of the membrane to form vacuoles, so not entering the cytosol freely.(38) Five mechanisms come into play, as seen in figure 1.4 and include:

- Clathrin-mediated endocytosis (10-150nm particles): a major pathway for NP entry, triggering entry on attachment to cell membrane receptors, in term triggering the GTPase enzyme dynamin to form vesicles with associated clathrin heavy chains

- Caveolae-mediated endocytosis (50-250nm particles): receptor-independent method of cell entry. Assembly of the hairpin-like caveolin coats on the cytosolic side of the plasma membrane, forming a flask-shaped caveolae-encased vacuole

- Clathrin & Caveolae independent endocytosis (60-100nm particles): involves use of lipid rafts and actin cytoskeleton to ensure cell entry

- Macropinocytosis: non-specific entry that occurs with large NP (200nm and above), initiated by actin signalling, leading to actin-stabilised cytoplasmic extensions engulfing the NP

- Phagocytosis: a separate uptake pathway to the above pinocytotic processes, occurring in select cells (e.g., B lymphocytes).
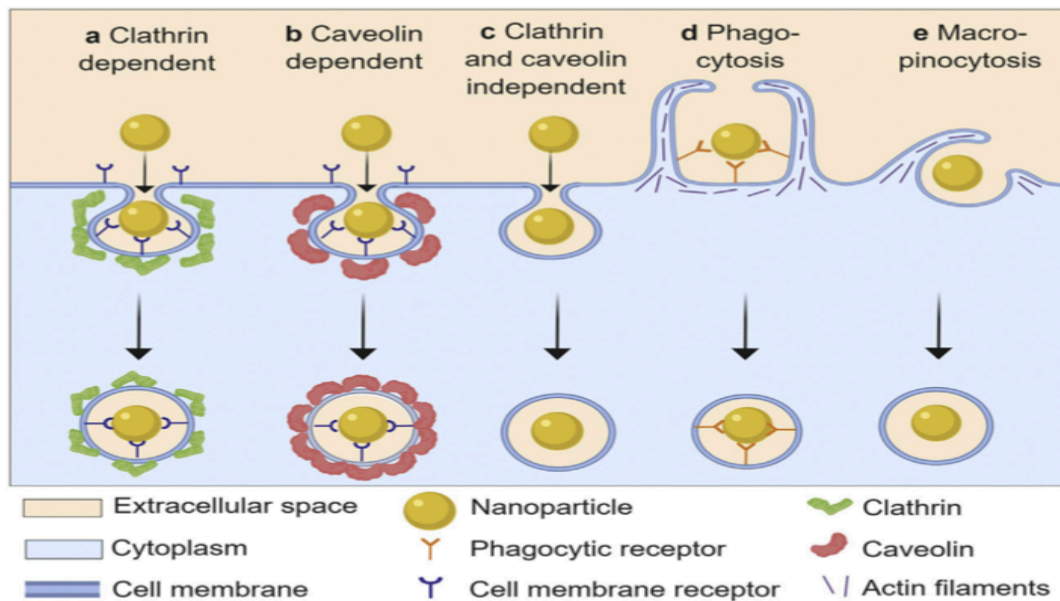
Figure 1.4: Nanoparticle Cell Entry Pathways, *source: Donahue et al.(34)*

The explanation demonstrates how the NP size may influence the preferred endocytic route. However, there is a significant variation reported amongst studies, due to varying NP structures and molecular profiles investigated.(39)(40) Other NP factors also determine the rate of entry, including its surface coating moieties & charge.(38,40) AuNP endocytosis will be discussed further in Chapter 2's literature review.

1.4.4 TOXICITY OF GOLD NANOPARTICLES

There is conflicting evidence within the literature regarding AuNP toxicity. This is invariably due to different physicochemical properties of NPs studied, as well as variable experimental conditions (incubation periods, cell lines and variation in incubation media). Some have expressed concern whereby AuNPs with a core diameter of 2nm or less are cytotoxic due to their enhanced permeability effects.(37,39,41) *In vitro* experiments performed by Albenese et al. did not demonstrate a significant HeLa, A549 or MDA-MB-436 cell toxicity with increased transferrin-coated 26nm AuNP aggregation and uptake.(42) Henson et al. demonstrated a concentration and size dependency on PEGylated AuNP toxicity in cardiomyocytes.(26) Dr. Broadbent's quantitative analysis of HeLa cell viability confirmed a slightly reduced cell growth

after 3 hours incubation with 13.5nm citrated coated AuNP, hypothesised to be due to apoptosis.(24)

In vivo experiment performed by Bahamonde et al. demonstrated uptake and toxicity differences between rats and mice when administering 15nm AuNPs. Sudden deaths were seen in a small percentage of the rat cohort due to brain ischaemia, attributed to vascular AuNP aggregation.(43) Undoubtably, systemic absorption of AuNP will have some degree of adverse effects, although topical and intra-tumoral applications may avoid these consequences. This is being explored in the dermatology division of medicine. Mouse skin models were injected with methotrexate coated AuNPs, which improved psoriasis, with a decrease in the scaling and erythema score.(44) This thesis permits the unique opportunity of topically applying NP solutions directly into the tumour sites through a trans-oral approach for OPSCC

1.4.5 INHERITED GOLD NANOPARTICLE- ROSE BENGAL STRUCTURE

Rose Bengal (RB) was considered as a PSA for the purposes of this project.
This is an anionic water-soluble xanthene dye and described as a type II PSA, inferring that once activated it transfers its energy to surrounding oxygen, forming singlet oxygen as described above. This is considered to have a superior cell-killing effect compared to type I PSAs, the latter reacting with biomolecules or cell membranes to allow hydrogen atom transfer and formation of free radicals.(45) RB is a familiar compound to the medical field, used for photochemical tissue bonding, ocular staining for examination and in liver function assays. This is poised for cancer treatment and is being used in Phase II clinical trials as a PSA for melanoma therapy (NCT02557321, NCT02288897). However, RB's anionic charge debilitates its capabilities of traversing cell membranes and entering cancer cells easily.(46)

This led to the development of an AuNP carrier for RB by our group.

This consisted of a citrate stabilised AuNP core, with a 13-15nm diameter, coated with a positively charged polyallylamine (PAH) and Rose Bengal (RB) layer (PAH-RB), followed by a negatively charged stabilising layer of sodium polystyrene sulfonate (PSS). Its synthesis was based on the layer-by-layer assembly technique described by Serrano et al.(47) Broadbent has confirmed its photodynamic killing efficacy in HeLa and UM-SCC cell lines.(24)
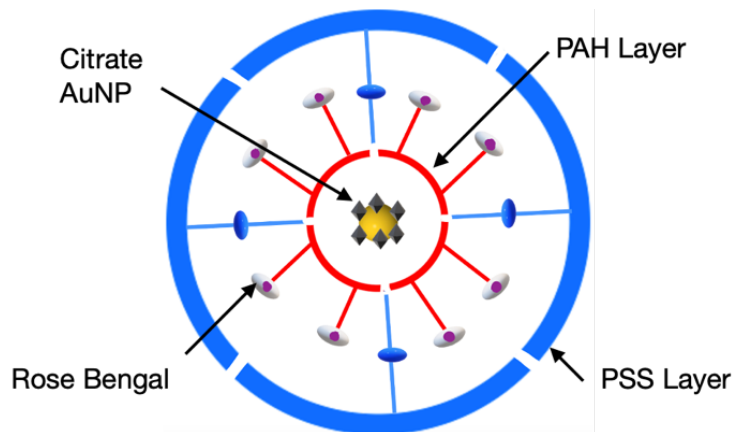
Figure 1.5: Inherited Bilayer Gold Nanoparticle

This NP-PSA complex provides a steppingstone to achieve a cancer targeting PDT centred therapy. OPSCC provides a unique opportunity for the topical application of AuNP associated PDT trans-orally, without the need for surgery to attain tumour access. Creating a selective NP-PSA complex with the inclusion of a targeting ligand is the next step in achieving a viable therapeutic prototype.

1.5 AIMS & OBJECTIVES OF THIS THESIS

This study's primary aim was to improve NP uptake specificity directed at cancer cells whilst avoiding uptake in normal 'physiological' cells. This would set PDT up as a more OPSCC-selective therapy in the clinical setting. The objectives covering this thesis included:

1. Develop a glycosylation technique for the NP-RB complex to improve selectivity for cancer cells

2. Develop an accurate quantification method for cellular internalisation (distinguishing from cell membrane absorption)

To increase the NP-PSA complex's selectivity, a rigorous literature analysis of the most recent AuNP glycosylation techniques with the aim of providing cancer cell targeting was performed, which is covered in Chapter 2. The studies are further critiqued on the quantification of NP

cellular internalisation, rather than solely NP uptake, which includes cellular adsorption and internalisation.

The project's glycosylated AuNP synthesis protocol is described in Chapter 3, adopting a PEGylation approach rather than the previously established bilayer approach. The resulting AuNPs were characterised accordingly with a combination of ultraviolet spectroscopy, differential centrifugal sedimentation (DCS), and zeta potential measurements, providing evidence for successful glycosylation.

Chapter 4 optimises a reported methodology that quantifies AuNP internalisation, building upon our team's inductively coupled plasma optical emission spectroscopy (ICP-OES) quantification technique. This utilises an I_2/KI etching system, investigating its gold etching potential and cell toxicity in HeLa, 74A and UM-SCC6 cell lines.

Initial cell uptake and internalisation experiments are reported in chapter 5 for both HeLa and 74A cell lines incubated with citrate coated, PEGylated and glycosylated AuNP solutions.

CHAPTER 2: NANOPARTICLE SELECTIVITY THROUGH GLYCOSYLATION

2.1 ENHANCING TUMOUR SELECTIVITY THROUGH GLYCOSYLATION

The project's main aim is to functionalise the NP-RB complex and increase tumour selectivity. A carbohydrate-based moiety was reviewed as a means of enhancing cancer selectivity in our targeting strategy.

The concept of tumour-enhanced glucose uptake was first described in 1927, by Otto Warburg. Coined the 'Warburg effect', increased rates of cell division in malignancies require enhanced aerobic glycolytic pathways and therefore lead to a raised glucose requirement.(48) The Warburg phenomenon exposed new fields in cancer research, including targeting cancer cells' glycolytic pathway to selectively stunt their growth,(48,49) and improving tumour localisation by contrast enhancement in radiological investigations.(50)(51) 18-fluro-2-deoxyglucose is utilised in the clinical setting with positron emission tomography radiological imaging as a means of accentuating malignant cells and associated metastatic lesions within the body.(50)

Glucose transporters (GLUTs) permit the facilitated diffusion of glucose molecules into cells and are over-expressed in several cancer types, HNSCC being no exception.(48,52) Li et al. demonstrated increased GLUT expression in recurrent and poorly- differentiated head and neck cancers.(53) Reisser et al. investigated the timeline of increased GLUT expression during cells' cancerous mutations. This entailed examining different tissue biopsies taken *in vivo* (5/13 being OPSCC) at various stages of their malignant transformation, together with normal marginal biopsies. The study showed a rise in GLUT1 expression in dysplastic lesions, implying early GLUT1 expression during HNSCC development.(54) In oral SCC lines, Azad et al. found a positive association between GLUT1 expression and tobacco addiction, indicating that patient-dependent variables can also influence GLUT expression.(55) Increased availability of GLUT in OPSCC may provide a viable option for improving our NP-PSA complex's tumour selectivity in OPSCC. This prompted a review of GLUT's structure to understand the attachment sites of glucose and uptake, aiding in the designs a glucose moiety to fit the transporter.

2.2 GLUT1 Transporter: Structure & Configuration

GLUT belongs to the 2A solute carrier gene family (SLC2A), which forms part of the major facilitator superfamily (MFS) proteins. This family shares a signature motif, believed to be a key element in transport kinetics.(56) There are 14 isoform representations of GLUT and three different classes. Class I GLUTs consist of sub-types 1,2,3 and 4: all highly selective for glucose and sharing a 14-63% and 30-79% protein sequence identity and homology, with similar transmembrane anatomies. Other GLUT classes differ in substrate selectivity, tissue expression and cellular localisation.(57) GLUT1 is over-expressed by several cancer cells and has been targeted extensively with numerous natural and synthetic molecules to produce anti-cancer effects alone or in combination with other medical agents.(57,58)

GLUT1 is encoded by the SLCA1 gene and serves as the prototype of this family. It remains the only glucose transporter to be purified.(59) Deng et al. reported GLUT1's crystallography structure with 3.2Å resolution, introducing two mutations in a full-length GLUT1 sequence.(60) Custodio et al. re-affirmed this by producing GLUT1 crystals in the presence of glucose and detergent Nonyl-B-D Glucoside.(56)

GLUT1 consists of 493 amino acids and 12 transmembrane (TM) alpha-helical domains that are linked by extra- and intracellular loops, with both N- and C-termini facing the cytosol. Modular representations of GLUT suggest that segments 1,2,5,7,8,10 and 11 form an inner helical bundle and central binding site with a water-accessible cavity within the membrane, shown in Figure 2.1. Outer TM helices 3,6,9 and 12 encircle and stabilise the inner bundle.(61,62) Intracellular components of helices 1,2,3, 4 and 14 interact with cytosolic parts of the transmembrane domain, mediating inter-domain interactions.(61,62) GLUT transporters alternate their molecular shape to either accommodate or transfer substrate. Four separate conformations alternate between inward and outward facing GLUT1 structure, depending on the orientation of the core binding site.(56,61) When the central binding site is facing outward (C^{out}), an extracellular carbohydrate can bind to its substrate-binding site (C^{outS}; Figure 2.1, BP2). Facilitated diffusion occurs as dictated by the surrounding concentration gradient, with a change in its conformation (C^{inS}; Figure 2.1, BP3) to inward-facing leading to substrate dissociating from the transporter into the cytosol (C^{in}).(62)

Four binding pockets that interact with glucose during various conformational changes of GLUT1 were discovered by Fu et al. through molecular docking studies.(62) The function of each binding site in transporting glucose into the cell is described below. Figure 2.1 summarises the location of GLUT1's binding pockets (BP), as well as their interactions with a glucose molecule as it traverses GLUT1's channel.

The first BP, referred to as the ligand recognition pocket (Figure 2.1, BP1), is found in the protein's outer vestibular area and is exposed to extra-cellular glucose when in the C^{out} state. This is 9Å from the surface of the channel and approximately 6Å away from the central cavity.(62) When glucose attaches to the first BP, the C^{outS} conformation results in a 1.4Å downshift of the glucose molecule towards the cytoplasm. The glucose molecule interacts with TM5's N-terminal and TM 7,8 and 11's C-termini to reach the second binding pocket (Figure 2.1, BP2), within the central part of GLUT1's cavity. This is found 15-20Å from the transporter's external surface and consists of N-domain of TM5 and C-domains of TM7,8 and 10.(56,59,61,62) At this point, the glucose molecule is initially hydrogen bonded to polar residues of the C-domains. This triggers a change in GLUT1's configuration to the C^{inS} state, with a shift in bonding with the N-domains of the involved TM helices.(56,59,61,62) This enables glucose to further rotate and reach the third binding pocket that is closer to the cytosol, hydrogen bonding with TM 2, 7, 8 & 11 (Figure 2.1, BP3).(62) The glucose molecule then moves into the fourth endoplasmic facing pocket (Figure 2.1, BP4), before finally entering the cell's cytoplasm.(62)
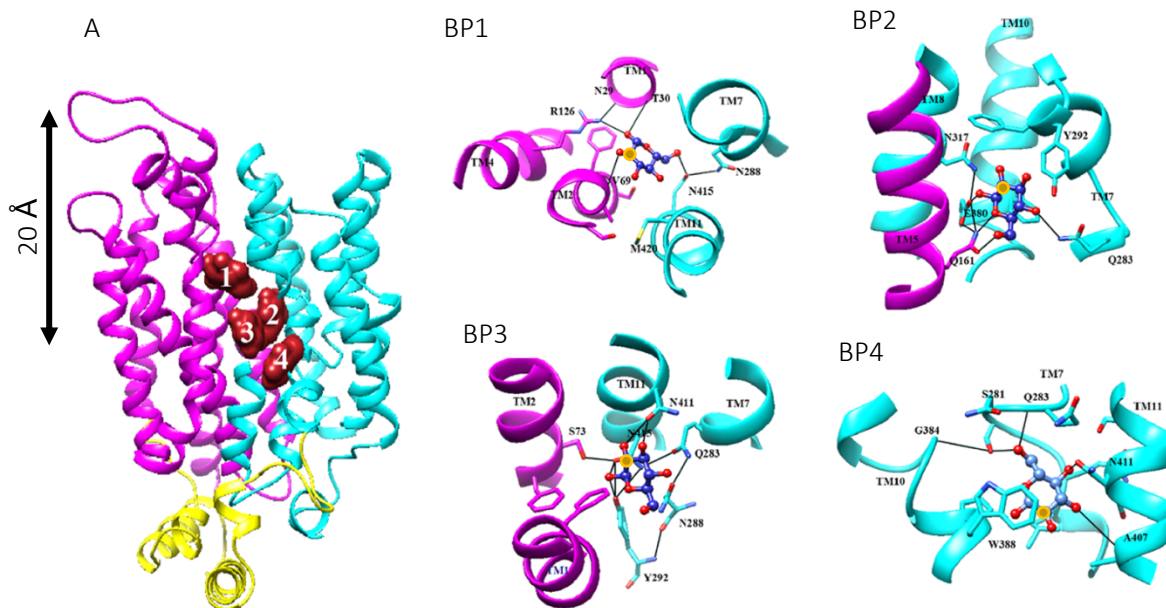
Figure 2.1: GLUT1 Configuration & Glucose Interactions. (A) represents the overall glut1 structure and its four binding sites. BP1-4 represent the binding Pockets' interactions with glucose, depicted as a ball and stick chain. the red atoms represent, oxygen, blue represent carbon and the Yellow atoms represent carbon 2.Modified from Fu et al.(62)

2.2.1 GLUT1 FEATURES TO CONSIDER WHEN GLYCOSYLATING NANOPARTICLES

The analysis of GLUT1 and its binding pockets has drawn two important considerations when glycosylating our NP-PSA complex.

Firstly, the central BPs 2 & 3 establish hydrogen bonding via TM 7 (Glutamine 292 N domain) and TM10 (Glutamic acid 380 C-domain) with the glucose's oxygens found on carbon 6, 4, 1 and its ethereal oxygen. In contrast, the oxygen on carbon 2 (represented as the yellow atom in Figure 2.1) only establishes interactions with TM11 (N-domain) in BP1, however not in the central binding site.(62) From the simulations performed by Fu et al. (Figure 2.1), carbon 2 & 3 are potential candidates for attachment with our NP-PSA complexes.

Secondly, the GLUT1's offered route for cell entry raises questions regarding NP-PSA complex's internalisation via the transporter. Whilst GLUT1 permits facilitated diffusion of glucose molecules that are approximately 1nm in size, our current NP-PSA complex ranges from 15-20nm in diameter. This infers that facilitated diffusion is not a viable route, leaving

endocytic mechanisms as an option for cellular uptake (chapter 1, figure 1.4). We have theorised that attachment of a glycosylated NP-PSA complex to the central BPs would change configuration from C^{out} to a C^{in} configuration. This would potentially trigger endocytic mechanisms for GLUT internalisation, permitting the NP-PSA complex's cell entry. The distance glucose to reach the central BPs from the outer surface is approximately 15-20Å. This implies that glycosylation of our NP-PSA complex cannot occur flush with its surface, leading to the requirement of a long enough linker moiety attaching glucose to the AuNP. However, our groups' previous data raises concerns if this is a viable hypothesis. Dr. Chadwick's thesis demonstrated that surface modified NPs with CALNN protein attached to the cell surface without triggering uptake. (41) NP-PSA complex internalisation is essential to maximise its cell killing capacity, as singlet oxygens' lifespan is microseconds and would be unlikely to instigate cell death if such reactions are occurring extracellularly.

Although GLUT1's structure has been extensively discussed in the literature, evidence on its internalisation is not as substantiated. Eyster et al. identified a clathrin independent endocytic mechanism for GLUT1 internalisation through antibody driven investigations.(63) Further investigative progress has been achieved with its relative, GLUT 4, in the setting of insulin stimulation. Yuan et al. reviewed the GLUT4 regulation in insulin-stimulated adipocytes. In scenarios where glucose uptake is downregulated (decrease in insulin), caveolae & Clathrin-mediated endocytosis decreased GLUT4 membrane expression. (64) This was supported by separate studies reviewing varying insulin levels in muscle and adipose tissue. (65,66) However, these endocytic mechanisms were all instigated by cytoplasmic messengers within cells rather than extracellular stimulators.

2.3 LITERATURE REVIEW: UPTAKE PATHWAYS OF GLYCOSYLATED NANOPARTICLES

2.3.1 AIMS & METHODOLOGY

The initial background reading on GLUT endocytosis did not reveal any definitive results confirming external stimulation of GLUT1 endocytosis (as opposed to cytoplasmic signalling for transporter down-regulation). This led to a more extensive literature review. The main aims for this review consisted of:

1. Glucose moiety used and structural configuration of its attachment to the NP

2. Investigations into cellular absorption and internalisation of glycosylated NPs (Glc-NPs)

3. GLUT interactions with Glc-NP

The review was initially discussed with the University of Liverpool Library services to ascertain the appropriate keywords, inclusion, and exclusion criteria. I took on the sole responsibility of reviewing all published articles against the inclusion and exclusion criteria stated. It was conducted using MEDLINE (Pubmed) and SCOPUS databases on the 20th of October 2021. Material published between the years 1990 to 2021 where reviewed, containing any of the following keywords (searched in all fields):

(((carbohydrate nanoparticle) OR (glucose nanoparticle) OR (glyconanoparticle)) AND ((tumour) OR (cancer) OR (neoplasm)) AND ((cellular uptake) OR (GLUT) OR (glucose transport) OR (endocytosis))).

Inclusion criteria consisted of:

1. Studies directly or indirectly investigating NP cell absorption and/ or uptake (organic and metallic NPs included) with the addition of a glucose/ glucose-derived ligand
2. Manuscripts written in or translated to English
3. Materials and methodology were adequately reported (with any supplementary material referenced in the text available).

Exclusion criteria included:

1. Studies whereby no glucose/ glucose-derivatives were attached to NP investigated
   Where only other monosaccharide attachments were investigated (e.g. galactose or mannose), these where not considered due to their lack of interaction with GLUT1.
2. Letters to the editors, abstracts and articles not published in the English language.

Each study included was described in a chronological manner using a descriptive analytical approach. Distinction between NP internalisation (through endosomes/ lysosomes) and cellular surface adsorption was considered, where possible, throughout the review.

2.3.2 RESULTS & ANALYSIS

2837 papers were retrieved from the literature search, after excluding duplicates. After going through the titles and abstracts, 46 publications were initially selected for further reading. 25 studies met the inclusion criteria included in the final literature review (Figure 2.2). Each study's method of investigating cell absorbance/uptake, strengths and limitations summarised in Appendix 1.
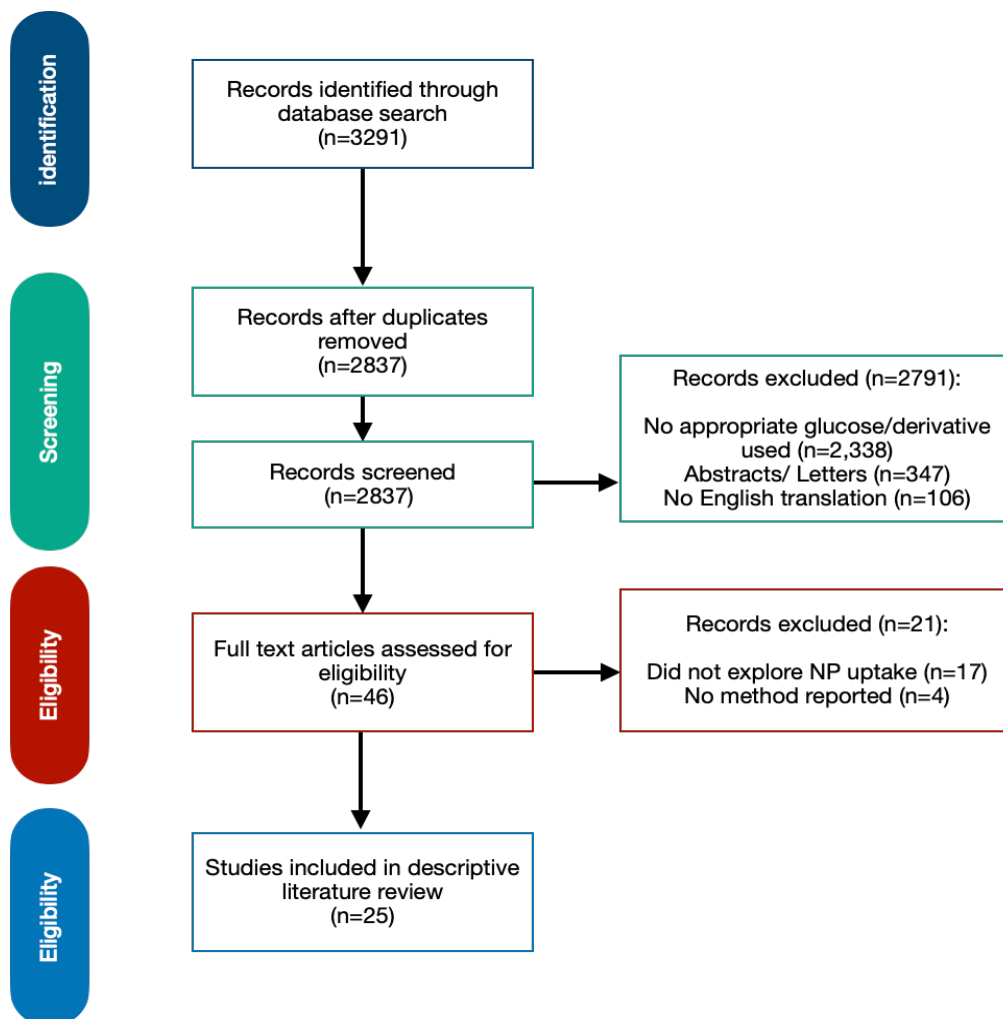
Figure 2.2: PRISMA Flow Diagram for Literature Review

Kong's research group published three papers in 2008 and 2011, detailing the use of AuNPs in different cancer cell lines.(67–69) The first, by Zhang et al, utilised a 1-thiol-beta-glucose

directly attached to AuNPs in a prostate cancer cell line to enhance radiotherapy sensitivity.(67) Transmission electron microscopy (TEM) qualitatively identified the cellular location of AuNPs. The images displayed were not convincing, with several NPs around the cell periphery and only a small number of NPs within the cytosol. This was a recurring theme for many of the studies reviewed. Inductively coupled plasma mass spectroscopy (ICP-MS) was used as a means of confirming quantitative NP uptake. This involved lysing a pre-determined number of cells and submitting the sample for estimation of gold (Au) concentration, enabling the number of AuNPs-per-cell to be calculated. Whilst this did not distinguish between NP adsorption and internalisation, it demonstrated a threefold increase in Glc-NP uptake (6.73×10^4 Glc-NP vs. 2.06×10^4 non-glycoslyated NPs). Radiation results further demonstrated that glycosylation of AuNPs (as opposed to simple citrate AuNPs) increased radiosensitivity by 50% at 24 hours and 39% after 48 hours of treatment with 2 Gray. (67) These suggest that glycosylation increased AuNP uptake when compared to citrate coated AuNPs and improved radiosensitivity. Other studies produced by the same research group utilised similar investigative patterns on enhancing radiotherapeutic effects on breast and ovarian cancer cell lines with modified AuNPs, achieving homogenous conclusions.(68,69) An interesting comparison was made between AuNPs with different surface properties; glycosylation using 1-thio-beta-glucose or the addition of cysteamine. The latter increased cell absorption, given its enhanced positive zeta potential profile compared to the glucose analogue. However, there was a significant decrease in cell viability when coupling Glc-NPs with X-ray and y-ray irradiation over cysteamine-coated AuNPs. It was hypothesised that cysteamine-NPs were mostly adsorbed to the cell membrane, whilst Glc-NPs were internalised to a greater extent, enhancing radiotherapy-induced apoptotic pathways.(67) The validity of these remarks and conclusions are questionable, given that they did not include comparative studies on GLUT-rich and GLUT-poor/ deficient cells. Glucose-deficient media was used with Glc-NPs and whilst stated in the methodology that GLUT1 inhibitor cytochalasin B would be used, no results were taking to this were documented. Given that in each study, glucose ligands were directly attached to the NP surface, GLUT1's central binding pockets were not accessible by these ligands. These limitations raise doubt whether increased uptake was associated with GLUT1 interaction or other uptake mechanisms.

Sur et al.'s study compared glucose and lactose moieties through their attachment with silver NPs. Lactose coated NPs showed improved cellular absorption that tailed off with the addition

of an oligonucleotide to the ligand structure, due to an enhanced positive zeta potential. Cell uptake was estimated indirectly from remaining NP present in the solution with an absorption spectrophotometer. (70) This raises questions regarding potential errors and inaccuracies in results reported. However, the impact of NP's zeta potential on cellular uptake was worth noting.

In 2011, Xiong et al. glycosylated their ferric oxide NPs (10nm diameter) with 2-deoxy-glucose, directly onto the NP surface via an esterification reaction. The study investigated NPs' potential in improving magnetic resonance imaging, using HeLa cells. The study attempted to demonstrate increased uptake of Glc-NP in comparison with non-glycosylated NPs through Prussian blue staining with light microscopy imaging. It was documented that NP aggregates formed when NPs were dispersed in water, with a resultant 156.2nm particulate size for Glc-NPs. (71) This distorts the validity of results, with different pinocytic pathways responsible for aggregates of such a large diameter.(56) Xiong et al. also do not provide suitable GLUT1-deficient cell line results or other suitable controls, making it difficult to draw any definitive conclusions of GLUT1 involvement.

In every study examined thus far, a glucose ligand was directly linked to the NP's surface. Wang et al. adopted a different synthesis approach in 2012. They coated their multi-drug-containing polymeric micelle NPs with 4-deoxy-glucose attached to a polyethylene glycol (PEG) group. Confocal laser microscopy with fluorescence attempted to identify increased Glc-NP uptake compared to 'control' NPs, although images were once again unconvincing. Through MTT assays, Glc-NPs showed enhanced cell killing efficacy in Hep2 cells when compared to non-glycosylated NPs and free/non-NP conjugated drugs. This suggested increased NP internalisation on glycosylation, due to the attached drugs' cell entry requirement to initiate its cytotoxic effects. However, such conclusions were strongly limited due to micelle aggregation reaching 500nm in size and again a lack of suitable GLUT1-deficient cell line controls. (72)

In 2014, Jiang et al. also used a PEG linker to attach 2-deoxy-glucose to a 71nm polytrimethylene carbonate NP (with paclitaxel chemotherapeutic agent) to treat brain glioma tumours. Confocal imaging with fluorescent dyes (LysoTracker Green and Hoechst) were unimpressive in both cell lines and spheroid models.(73) However, a more convincing investigative technique differentiated cell absorbance from internalisation, through the use of

endocytosis pathway inhibitors. Cytochalasin B (inhibits GLUT internalisation through its endofacial glucose binding site) demonstrated a 75% decrease (p <0.01) in cellular uptake, using flow cytometry for quantitative measurement. A significant decrease (p<0.05) was also seen with CPZ (clathrin inhibitor), filipin and genistein (caveolae-mediated endocytic inhibition). Interestingly, DMA (microtubule disrupting agent) did not decrease uptake, indicating that macro-pinocytosis did not play a significant role. *In vivo* experiments using BALB/c mice models demonstrated an increased (by 1.94) fluorescence intensity in the tumour site, with decreased non-specific accumulation in the reticulo-endothelial systems when compared to non-Glc NPs.(73) The study demonstrated GLUT1 involvement in Glc-NP endocytosis through its use of cytochalasin B, although no comparative studies with GLUT1 deficient cell lines were performed.

Eight separate studies in 2015-2017 period investigating selective Glc-NP cell uptake did not report any other noteworthy conclusions and can be found summarised in Appendix 1.(74–80) These include the stud by Barbaro et al, whereby glucose moieties were attached directly onto their NPs, inferring that it would be improbable for their glucose moieties to interact with GLUT1's central binding pockets. Furthermore, their particle sizes are significantly small (2.7nm and 2nm respectively), increasing the use of passive diffusion in cancer cells rather than endocytic pathways.(81)

Publications by Dreifuss and Motei et al. in 2016 and 2018 are landmark papers for the purpose of this review: addressing glucose attachment to NP via PEG linkers, as well as exploring GLUT internalisation pathways.(82,83) The first paper by Motei et al. in 2016 reviewed the optimal carbon for attachment of glucose analogues to AuNPs via a PEG7 linker. This was done with the intention of developing a tumour-selective NP to distinguish between cancerous and inflammatory tissue with positron emission tomography imaging. *In vitro* testing on head and neck cancer cell line (A431) demonstrated increased cell absorption when using glucose's second carbon (2-C) for attachment: a three-fold increased absorption seen compared to using 3-C and 6-C glucose attachment, whilst having a five-fold increase compared to 1-C glucose attachment. This was further echoed in their *in vivo* mouse model investigations, with an approximate three-fold difference between 2-C and 1,3 & 6-C attachment of glucose.(82) As visualised in Figure 2.1, Fu et al.'s study suggested that 1-C and 6-C are H-bonded to GLUT1 when glucose is in the central BPs.(62) However, their model suggested that glucose's 3-C did not interfere with H-bonding. This conflicts with Motei et al.'s

resulting, hinting towards potential steric interactions that prevent glucose from binding when attached via its 3-C.

The Dreifuss et al. study continued to further examine the potential uptake mechanisms of AuNP coated in 2-deoxy-glucose attached via a PEG7 linker. *In vitro* studies explored Glc-NP internalisation pathways through cell lines where GLUT1 percentage expression was confirmed with flow cytometry. These included: HNSCC (A431, high GLUT1 expression), lung carcinoma (A549, high GLUT1 expression), prostate carcinoma (LNCaP, low GLUT1 expression) and fibroblast cells (3T3, low GLUT1 expression). Flame atomic absorption spectroscopy (FAAS) was used to measure the gold concentration from lysed cells and subsequently estimate the AuNP concentration. Initial results demonstrated that Glc-NPs attached to PEG via 2-C showed increased uptake in cell lines with high GLUT1 expression. Various endocytic inhibitors were then used, each inhibiting a specific pathway, and included chlorpromazine (clathrin-mediated endocytosis), nystatin (calveolae-mediated) and amiloride (other pinocytic pathways). Clathrin inhibition (chlorpromazine) profoundly affected Glc-NP absorption in A431 (35% decrease) and A549 (75% decrease), whilst caveolae inhibition (nystatin) had a modest decrease (A431 25% & A549 10%). These inhibitors did not significantly affect cell lines with a lack of GLUT1 expression (LNCaP and 3T3).(83) As per Jiang et al.'s conclusions,(73) these studies provided clarity GLUT1 is directly involved in NP internalisation, through the interaction of glucose with the central binding pockets (attached by a PEG7 linker approximately 25Å long). Dreifuss & Motei et al. also provided substantial evidence on glucose's carbon attachment to the NP-PSA complex.

The study by Pia et al. is the next published article in this review to evaluate the influence of glucose's carbon positioning on cellular uptake in HeLa cell cultures. Single-chain glycopolymer NPs were assimilated using glucose's carbon-1 and carbon-6 as conjugation positions with NPs. Results indicated increased adsorption when glucose's C1 position was not modified, albeit the methodology used to analyse 'uptake' and results were minimalistic and incomplete in some parts. No comparisons with glucose attachment via its other carbons were reviewed and there were no suitable controls to confirm GLUT1 involvement in increased NP uptake.(84)

Four separate studies published in 2018 and 2019 were included in this review.(85–88) Similarly to other studies discussed beforehand, such as Barbaro et al., (81) Sun et al. do not use a

linker between their glucose ligand and NP, limiting the relevance of any conclusions attained. (87) Li et al. utilised a Glc-NP complex to target breast carcinoma cell lines, using 3-amino-1-diethylene glycol-α- D-glucopyranoside as a linker and binding glucose via its carbon-1. There was a 46-fold and 1.43-fold higher uptake of this Glc-NP when compared to non-Glc NPs and glucosamine coated NPs. The higher uptake of Glc-NP compared to glucosamine coated NPs re-affirms the importance of using of a linker, permitting interaction with GLUT1. It should be noted that the polymeric NPs utilised may have had glucosamine bound at the end of polymer chains, this itself acting a sufficient 'linker' to permit GLUT1 interaction. GLUT1 involvement was further evidenced through use of a competitive GLUT1 inhibitor, reducing cellular uptake of Glc-NP & glucosamine coated NPs. Despite using multiple fluorescent dyes to better depict cellular structures, most of the NPs were seen to be around the cell's periphery. The study does report successful *in vivo efficacy* in mice, although does not provide any substantial control to indicate that enhanced uptake is mediate by glucose ligands' interaction with GLUT. (89) This could be due to different capping layer's properties, especially given that glucose is bound via its 1-C.

In 2020, Wang et al. investigated glioma cell lines' GLUT4 trancytosis process, using glycosylated heptapeptide nanodiscs (50nm diameter). The most significant reduction in Glc-NP cellular uptake was observed when clathrin-mediated endocytosis was inhibited. Similar inhibitory approaches were used to rule out caveolae-mediated endocytosis of Glc-NP/GLUT1; they were in accordance with earlier reports. Four different fluorescence dyes (DAPI, DiO & DiD) were also used in Förster resonance energy transfer (FRET) imaging techniques, localising endosomal cell entry as well as exocytic pathways. One limitation of the study was the lack of physiological cell line as a comparison of rate of cell absorption and inhibitor effects.(90) Whilst it has shown that there is NP internalisation through Clathrin-mediated endocytosis, this was not specific to GLUT transporters and not conclusive of Glc-NPs interactions with GLUT.

Aslan et al. further re-affirmed enhanced absorption effects of their Glc-NP, using Horse spleen ferritin as a linker (between 2-deoxy-glucose and AuNPs) to enhance their complex's physiochemical stability and bioavailability. They investigated selective uptake in breast cancer cell lines MCF-10A and MCF-7 as a means of using the complex as an imaging probe for computed tomography scans. Both fluorescence microscopy and ICP-MS showed an increased uptake of Glc-NP when compared to 'naked' NPs, this being more prevalent in the GLUT1-rich MCF7 cell line.(91)

Relevant Results Considered for the Thesis

An analysis of GLUT1's structure and a literature review on NP glycosylation has provided further insights that need to be considered when modifying the NP-PSA complex:

- GLUT1's central binding site is approximately 20Å from its external surface.
- Glucose carbons 1,4,5 and 6 were involved in most interactions with GLUT1 transporter's central binding site.
- Literature review provides strong conclusions that attachment of glucose via 2-C to a PEG linker/ NP provides greatest uptake rate as this permits glucose to interact successfully with GLUT sites.
- Clathrin-endocytic routes are strongly linked with GLUT internalisation, as evidence by decreased uptake of Glc-NPs when endocytic inhibitors where present.

These suggestions were taken into consideration when developing a synthesis technique for Glc-NP. The glycosylation technique for this thesis will be elaborated on in chapter 3, whilst initial uptake experiments are described in chapter 5.

CHAPTER 3: SYNTHESIS OF GLYCOSYLATED NANOPARTICLES

3.1 FUNDAMENTAL DESIGN CONSIDERATIONS

3.1.1 POLYETHYLENE GLYCOL REAGENTS AS A SPACER

The literature study in Chapter 2 emphasised the requirement for a "spacer," a linear structure positioned 20 between the glucose ligand and AuNP to prevent glycosylation from occurring flush with the surface of the AuNP. This may permit adequate binding of a glycosylated molecule to a GLUT1's central binding pockets. Polyethylene glycol (PEG) compounds fulfilled this role in most of the studies discussed in Chapter 2, including landmark papers by Dreifuss et al. & Motiei et al.(82,83) A PEG linker of a minimum of 5.7 repeats is equivalent to the distance of the GLUT1's central binding site at 20Å (a single ethylene glycol monomer is approximately 3.5Å in length). PEG reagents have been used in NP research, with its features and benefits outlined below.

3.1.2 POLYETHYLENE GLYCOL REAGENTS IN THE NANOTECHNOLOGICAL FIELD

In 1977, Davis and Abuchowski covalently attached PEG to bovine serum albumin and liver catalase protein, increasing systemic circulation and reducing immunological inhibition.(92) PEG reagents have since gained popularity in medical research, with the FDA approving PEGylated products to treat varying diseases such as rheumatoid arthritis and severe combined immunodeficiency disease.(93) In nanomedicine, PEG molecules are favoured as capping agents, delaying uptake through the reticular-endothelial system as well as impeding opsonisation and phagocytosis through complement proteins and phagocytes.(94) This is achieved by surrounding NPs with a hydrophilic capping layer, protecting its surface from surrounding environment. PEG chains' flexibility hinders serum corona formation, increasing blood circulation half-life and reducing liver uptake, whilst also reducing NP aggregation (although this also largely depends on their terminal chains, as discussed later).(95-97) The likelihood of tumour cell uptake increases with increased NP circulation. Tumor cells have more

porous lymphatic channels and vasculature than typical physiological cells, which results in increased permeability and retention.(98) This is exploited by NP-product Doxil®, whereby PEGylated liposomes increased doxorubin's bioavailability (as opposed to an unaltered tablet version), improving its circulation half-life and anti-tumour effects.(93)(93)

Several PEG-related factors further influence NP circulation time, including grafting density and conformation, molecular weight, and terminal functionalisation.(99) A PEG capping layer must be sufficiently thick to sterically shield NP surfaces and prevent aggregation as well as adsorption to serum proteins. Lipka et al. demonstrated that PEG chains of 10kDa in weight improves blood circulation time (15% vs. 0.1%) after 24 hours in the bloodstream of mice test subjects, confirmed through repeat blood tests.(100) Interestingly, Yang et al. have also shown a low MW PEG layer (660 Da) grafted at a high surface density may be similarly effective (compared to 2 kDa).(95) Grafting density refers to the number of PEG chains bound to the NP surface and is one of the factors that dictates the PEG chains' configurations (whether this is a mushroom or brush configuration). Three factors determining the confirmation include polymer chain length (n), monomer length (α) and solvent types (v). These determine the minimum distance between PEG chains (referred to as the *Flory Radius, R)* and consequently the conformation. The relation between the three factors & R is described through the equation:

$$R = \alpha n^v$$

If the grafting density records a lower spacing than *R,* a brush conformation is assumed, improving NP stealth in the bloodstream. Cruje et al. used spherical AuNPs (50nm) coated with two PEGs (varying molecular weight), varying the grafting densities to investigate non-specific protein adsorption and cancer cell uptake.(95) Higher density grafting of shorter PEG chain lengths with a brush configuration exhibited a longer circulation time by reducing activation of the body's complement system (seen at 2kDA with a $1PEG/nm^2$ density compared to 5kDa at $1PEG/2nm^2$).(101)

PEG terminal functionalisation not only contributes to its 'stealth' properties but also allows for improved cellular selectivity. Heterobifunctional PEGs covalently couple with NPs whilst providing a means of enhancing cellular uptake through ligand conjugation. Although heterobifunctional chains had an increased opsonisation risk, Harrison et al found that they were less prone to serum adsorption than a mixed monolayer PEG capping alternative

(performing dynamic light scattering post incubation with cell culture media).(96) A suggestion for getting over this limitation is to make sure that the PEG chain lengths are longer than the molecules that are conjugated to it, maximising its circulation time.(97) A separate 'PEG dilemma' regarding functionalisation was addressed by Liu and Thiery, whereby higher molecular weight PEGs prevent NP aggregation but only offer a few terminal conjugation options. Their study investigated the use of mixed PEG reagents and develop a biofunctionalization protocol applicable to AuNPs.(102) Thiolated PEGs with a carboxylic-functionalised terminal of two different molecular weights were used (approximately 460 and 5000). These were used to cap AuNPs of varying sizes (18, 60 and 175nm diameter) at varying ratios. Smaller diameter AuNPs were stabilised by short PEG chains, whilst larger diameter AuNPs continued to aggregate (as demonstrated by UV-vis and dynamic light scattering), requiring a mixture of a 1:1 ratio of long-to short chains to prevent aggregation. When conjugating lysosome protein to carboxylic acid terminated PEG layers, all AuNPs coated in short PEG chains aggregated. With respect to small AuNPs, a minimum ratio of 4:1 (Long: Short) was required to provide stability when biomacromolecules were conjugated. Whilst short PEG chains improved carboxyl group reactivity through inherently smaller steric exclusion volumes, longer PEG chains were required to prevent aggregation. (102)

3.1.3 Chosen Glucose Ligand & PEG Conjugation

Chapter 2's literature review identified glucose's carbon-2 as being an ideal conjugation point. When comparing glucose conjugations at various carbons, Motei et al. further re-affirmed the advantage of glucose's conjugation at 2-C. This enables glycosylated NPs to bind to the GLUT1 when it is in the C_{out} conformation, with increased tumour uptake established in this study. Taking the above requirements into consideration, glucosamine was identified as an ideal glycosylation ligand for this project. Figure 3.1 demonstrates the chemical structures of
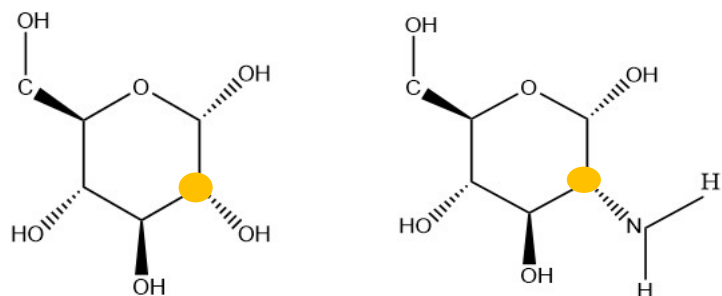
Figure 3.1: Chemical Structures of Glucose (left) & Glucosamine (Right). Yellow atom represents carbon 2

glucosamine (and glucose as a comparison), with a reactive amine group on glucosamine's second carbon. This permits conjugation to a PEG chain through a carbodiimide-mediated crosslinking reaction.

The carbodiimide-mediated crosslinking reaction is a common and recognised biofunctionalization route. Whilst this will be described in more detail below, in essence it crosslinks an amine and carboxylic acid group, thereby allowing us to crosslink the glucosamine's amine group with a PEG chain having a carboxylic acid terminal.(103,104) This reaction has been previously used by our group in the NP-PS complex's synthesis for attachment of RB to the PAH layer. A homobifunctional PEG crosslinker with end-carboxyl groups, poly(ethylene glycol) bis(carboxymethyl) ether (average MW 650, procured from Merk UK, referred to as COOH-PEG$_{11}$COOH) was considered as the spacer (figure 3.2). This has carboxyl terminals that allow cross-linking with glucosamine from one end and the AuNP from the other, whilst satisfying the 20Å spacer length requirement. An analysis of the optimal cross-linking reaction conditions is covered in the following section, playing a crucial role in our proposed glycosylation technique.
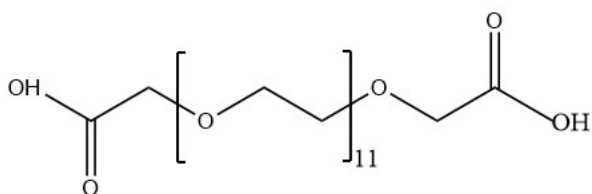
Figure 3.2: Poly(ethyelene Glycol) Bis (Carboxylmethyl) Ether

3.1.4 CARBODIIMIDE CROSSLINKER REACTION

This well-established method achieves a covalent bond between two specific functional groups; carboxyl and amine groups, using crosslinker 1-ethyl-3(3-dimethylaminopropyl) carbodiimide (EDC).(103) This water-soluble compound activates carboxyl groups for direct reaction via amide bond formation. As no portion of the EDC chemical forms part of the final structure between the two conjugated compounds, EDC and carbodiimides are considered 'zero-length' carboxyl-to-amine crosslinkers.(105)

The various potential EDC reactions are summarised in figure 3.3, depending on which other reagents are utilised. EDC initially forms a relatively unstable O-acylisourea intermediate with carboxylic acid groups, that may go on to either form an amide bond with a primary amine or

hydrolyse back to its original products. The presence of N-hydroxysulfosuccinimide (s-NHS) improves the stability of the intermediate, forming an amine-reactive NHS ester and increasing the efficiency of the final desired amide bond to be established.(103) pH is an important factor affecting the reaction's efficiency. The initial EDC/NHS activation reaction with the carboxyl group is most efficient at pH 4.5-7.2. 2-[morpholino]ethanesulfonic acid (MES) buffer is used to achieve the desired pH. The second stage of the reaction with NHS-activated molecules is most efficient at pH 7-8, were phosphate-buffered saline is more favoured.(103,104)
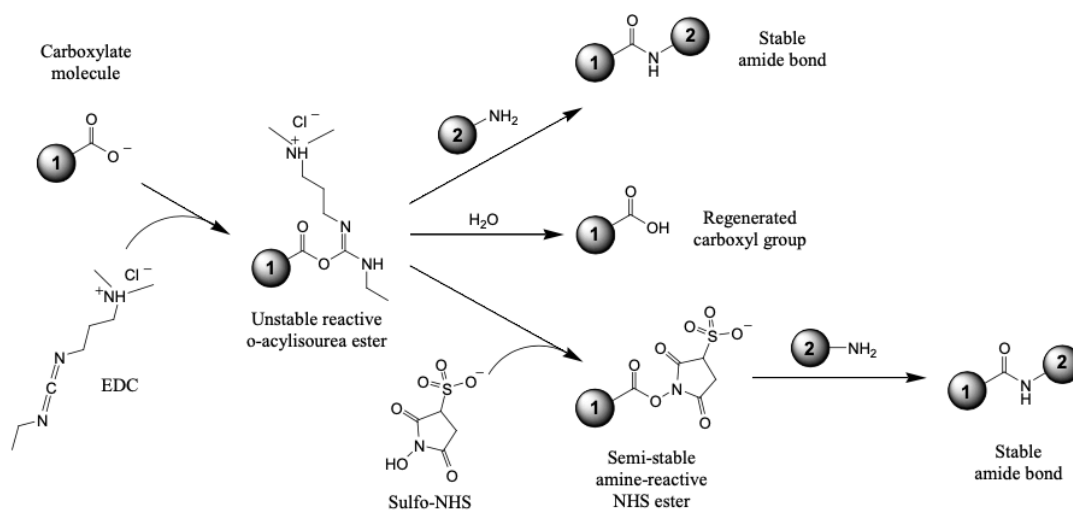
Figure 3.3: EDC/ NHS Reaction. Source: Thermo Scientific (103)

3.1.5 GLYCOSYLATION PROPOSAL FOR NP-PSA COMPLEX

Two consecutive EDC reactions were proposed to glycosylate the NP-PSA complex. The importance of the reactants' ratios cannot be understated, being responsible for the percentage quantity of each reaction's products, summarised in figure 3.4.

The first reaction attaches glucosamine to one of the carboxyl ends of the COOH-PEG$_{11}$-COOH spacer, by reacting glucosamine, EDC and COOH-PEG$_{11}$-COOH. A reactant ratio of 1:1:1 is required to attain COOH-PEG$_{11}$-Glc as the desired main product (approximately 50% at the specified reactant ratio), retaining a free carboxyl group. Side products include glucosamine at both terminal ends of the PEG linker (Glc-PEG$_{11}$-Glc) and unreacted PEG reagent (COOH-PEG$_{11}$-COOH).

Subsequently, the above mixture would undergo a further crosslinking reaction through the addition of EDC (COOH-PEG$_{11}$-Glc: EDC ratio of 1:0.01). This would crosslink the free carboxyl terminal on the COOH-PEG$_{11}$-Glc chain with an amine group present in the PAH layer of the current NP- PSA complex. After two successive EDC reactions at the specified reactant ratios, 0.5% of the end products would be the the desired EDC-PEG$_{11}$-Glc required for glycosylation. To balance creating the desired EDC-PEG$_{11}$-Glc and avoiding unwanted biproducts that could prevent crosslinking, the EDC concentration was lowered for the second crosslinking reaction. Approximately 0.0025% of PEGylated biproducts, EDC-PEG$_{11}$-EDC, predisposes to Glc-NP crosslinking and aggregation through amine group coupling (by-products summarised in Figure 3.4). Most of the other biproducts would be either incapable of binding to the NP-PSA complex or create NP dispersion (EDC-PEG$_{11}$-COOH). Centrifugation steps were devised in the synthesis technique to remove the unwanted biproducts that do not react with AuNPs.
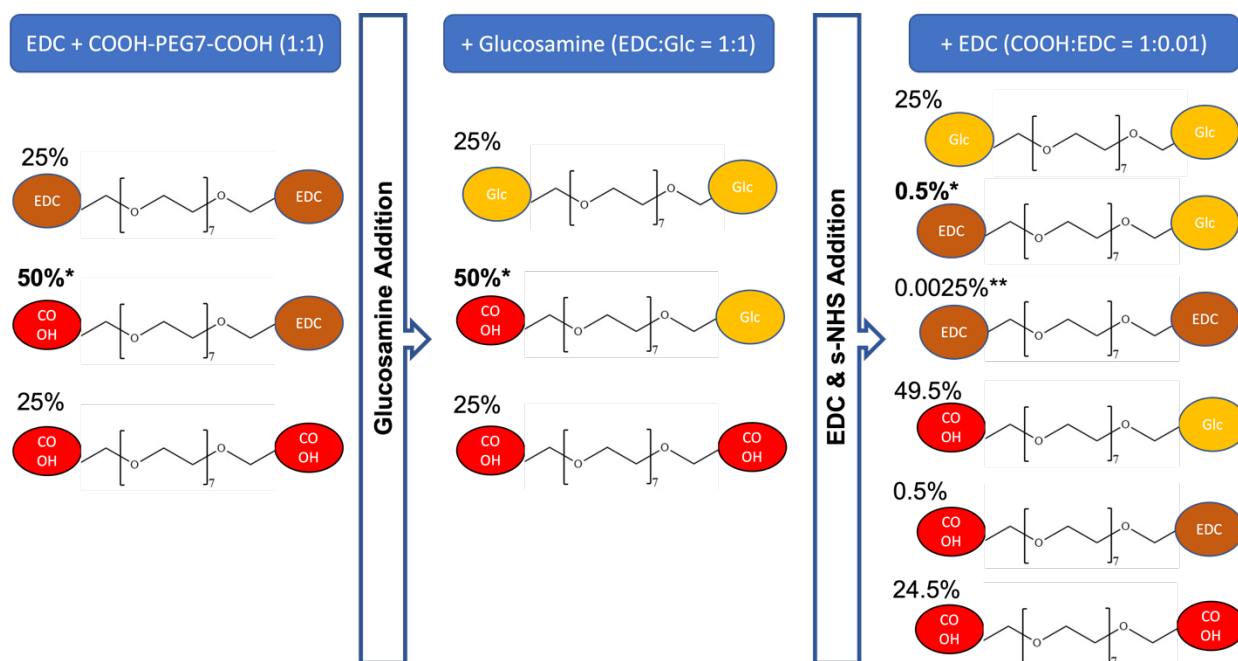
Figure 3.4: Products from Dual EDC/s-NHS Reactions for Glycosylation. Percentages are dependent on the ratio of reactants displayed. *; desired products required for glycosylation, **; undesired biproduct that promotes NP aggregation.

The original synthesis design would then follow to add the activated mixture containing EDC-PEG$_{11}$-Glc to the Dr. Broadbent's AuNP with an overlying PAH/RB layer. The addition of EDC-PEG$_{11}$-Glc to the amine groups of the PAH layer and a subsequent coating with a PSS layer would then follow, stabilising the NP-PSA complex (figure 3.5). Although theoretically feasible, the following disadvantages were considered and a different strategy was chosen. The glucosamine would need to be attached to a PAH layer. Whilst ideally glucosamine should be on the NP-PSA complex's outer surface, the PAH layer would be unstable as an outer layer, requiring an additional PSS layer to stabilise it, regardless of the number of additional bilayers already present. This infers the glycosylated PEG linker not being on the outer shell, potentially creating hindrance and issues with GLUT1 accessibility for binding. Furthermore, photosensitivity of RB may not be as effective when found between the PAH and PSS layers, rather than on the exterior surface of the complex. This led to the proposition of an alternative NP-PSA complex, based on a combination of different PEG linkers.
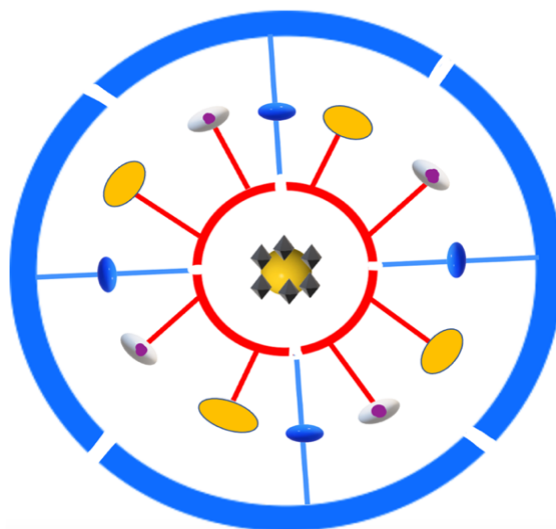
Figure 3.5: Initial Proposition for Glycosylated Gold Nanoparticle Central molecule represents a citrate-coated AuNP. Yellow molecules represent glucosamine, the grey/purple molecules Rose Bengal, both attached to PAH layer (red). PSS layer (blue) forms the outermost layer.

3.1.6 THESIS' AuNP GLYCOSYLATION PROPOSAL USING THIOL-PEGS

A separate strategy considered a functionalised PEG capping layer using thiolated PEG reagents that would house both the PSA Rose Bengal (RB) and glycosylated ligand. Heterobifunctional PEG reagents with thiol-end groups are widely used to create strong covalent bonds with gold and form a stable capping layer. This permits the remaining free ends of the PEG reagents to either provide NP stability and prevent aggregation or serve to functionalise the NP through glycosylation. Theoretically, both RB and glycosylated ligands could be attached to the PEG's capping layer, attaining both PDT functionality and tumour-

selectivity. However, for the purpose of this thesis, functionality through glycosylation was prioritised, ensuring that the synthesised particle is stable.

The synthesis technique describes of a stepwise capping approach evaluated in this project. The initial step included attaching a combination of two heterobifunctional thiolated PEGs onto citrated coated AuNPs (figure 3.6). Whilst a heterobifunctional thiolated PEG is required with an amine end to enable EDC reactions and the addition of glucose and RB; encasing AuNPs solely with an amine-terminal PEG linker would result in cross-linking between the NPs and aggregation. This has led to the addition of a further heterobifunctional thiolated PEG with a hydroxyl group, creating a negative surface charge and enforce NP dispersion. The thiolated PEG reagents were purchased from Prochimia Ltd. (figure 3.6);

1. HS-$(CH_2)_{11}$-EG**6**-NH2: 424 Molecular Weight (MW), referred to as PEG$_6$-NH2
2. HS-$(CH_2)_{11}$-EG**5**-OH: 503 MW, referred to as PEG$_5$-OH
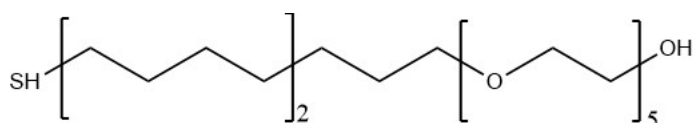
(A)

Figure 3.6: PEG Reagents for Initial Capping Layer
(A) thiol PEG with hydroxyl terminal
(B) thiol PEG with amine terminal

(B)
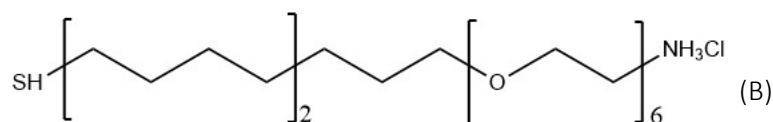
The surface chemistry for the expected AuNPs with a PEGylated capping layer (PEG-NP) is demonstrated in figure 3.7 (a). Subsequently, the two consecutive EDC reactions described in figure 3.2 would be undertaken to attach the glycosylated PEG reagent (EDC-PEG$_{11}$-Glc) to the amine terminals of the PEGylated capping layer over the AuNPs. The expected final Glc-NP is demonstrated in figure 3.7 (b), with approximately half of the PEG-NH$_2$'s amine terminals conjugated with EDC-PEG$_{11}$-Glc and the remaining amine terminals with EDC-PEG$_{11}$-COOH.
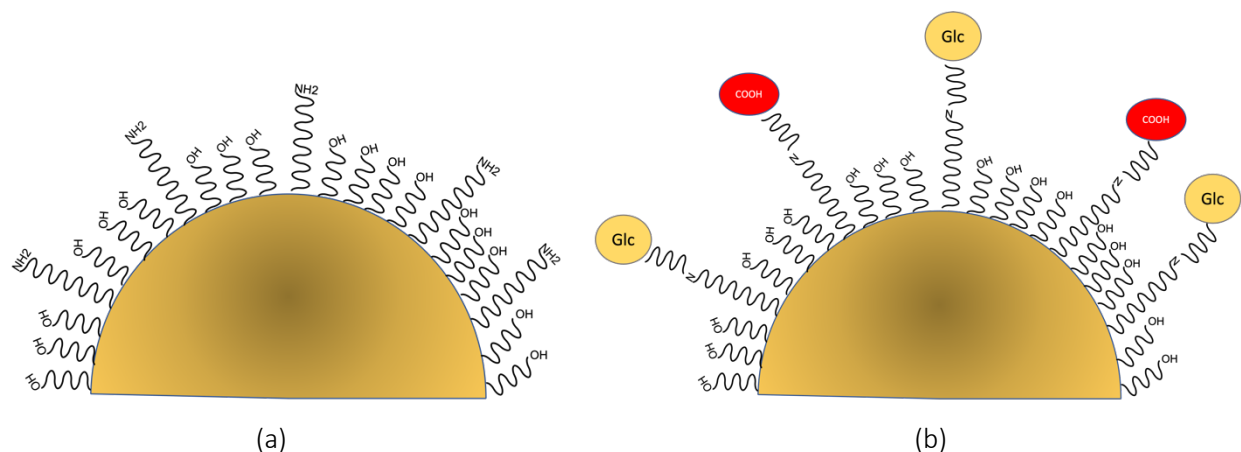
Figure 3.7: (a) PEG-NP Surface Chemistry (b) Glc-NP Surface Chemistry

3.2 METHODOLOGY

Section 3.2.1 describes the synthesis protocol for Glc-NP (summarised in figure 3.8). After the preliminary outcomes described in section 3.3.1, a change to the basic methodology that involved adding Tween-20 to the NP solution during centrifugations was taken into consideration.

3.2.1 GLYCOSYLATED AuNP COMPLEX SYNTHESIS STEPS

AuNP Synthesis: The Turkevich-Frens method was utilised to synthesise 13-15nm citrate-coated AuNPs.(33,106)

- 150ml Aqua Regia was prepared (HCl: HNO_3 in a ratio of 3:1)
- A double-necked round bottomed flask was washed with Aqua Regia and thoroughly rinsed with water
- Tetrachloroauric(III) acid trihydrate ($HAuCl_4.3H_2O$) was dissolved in MQ-H_2O to form a 0.2845M stock solution
- 169.6ul of this solution was pipetted into the round bottomed flask, followed by 150ml MQ-H_2O

- 34mM trisodium citrate dihydrate (HOC(COONa)(CH$_2$COONa)$_2$.2H$_2$O) aqueous solution was prepared in MQ-H$_2$O
- The diluted HAuCl$_4$.3H$_2$0 solution was heated under reflux, using a condenser whilst being magnetically stirred, until boiling. HOC(COONa)(CH$_2$COONa)$_2$.2H$_2$O solution was heated separately
- 4.5ml of HOC(COONa)(CH$_2$COONa)$_2$.2H$_2$O was added to HAuCl$_4$.3H$_2$0 in the round bottomed flask and heated for 25 minutes under reflux
- The solution was allowed to cool and kept magnetically stirred for 24 hours
- A ruby red solution forms and is filtered through fluted filter paper into falcon tubes
- This was stored at 5°C

Addition of PEG Capping Layer:

- PEG$_6$-NH$_2$ & PEG$_5$-OH stock solutions were created by dissolving each in MQ-H$_2$O & methanol, respectively
- Pre-determined volumes of PEG$_5$-OH & PEG$_6$-NH$_2$ were used to prepare a single combined solution in MQ-H$_2$O (in varying ratios, including PEG$_5$-OH:PEG$_6$-NH$_2$ 99:1 & 98:2) with a final total PEG concentration of 2mM & stirred for 30 minutes
- A pre-determined concentration of AuNP solution was added dropwise & stirred overnight
- The solution was centrifuged at 10900xg for 30 minutes at 8°C three times using Heraeus Megafuge 8R Centrifuge in aliquots of 1.5ml as a means of removing excess ligands (cleansing step). After the first two centrifugations, supernatant was removed and replaced with 1.5ml 0.01% v/v Tween-20 dissolved in Phosphate buffer saline (PBS). After the final centrifugation, supernatant was pipetted and replaced with 0.8ml 0.01% v/v Tween-20

Glycosylation of AuNP (Glc-NP): EDC reactions were undertaken to glycosylate the PEG capped AuNP (PEG-NP). The ratio of reagents was discussed in section 3.1.5 (figure 3.4 summarises the products attained from the EDC reactions).

- Poly(ethylene glycol) bis(carboxymethyl) ether (COOH-PEG$_{11}$-COOH, density 1.191g/ml at 25°C) was dissolved in MQ-H$_2$O to achieve a stock solution
- 2.5mM EDC & 6.25mM s-NHS (concentration ratio of EDC:s-NHS - 1:2.5) were reacted with 2.5mM COOH-PEG$_7$-COOH in 0.1M MES (pH 6), forming a total volume of 1ml, whilst being continuously stirred for 30 minutes

- Glucosamine (equivalent number of micromoles as COOH-PEG$_7$-COOH, i.e., 2.5µmol) was subsequently added to the solution and stirred for 3 hours
- Further 25nmol EDC and 6.25umol s-NHS were added to the solution & allowed to stir for 30 minutes
- PEGylated NP solution was added and stirred for 2 hours
- The solution was centrifuged at 10900xg for 30 minutes at 8°C two times using Heraeus Megafuge 8R Centrifuge in aliquots of 1.5ml as a means of removing excess ligands (cleansing step). After the first centrifugation, supernatant was removed and replaced with 1.5ml 0.01% v/v Tween-20 dissolved in PBS. After the second centrifugation, supernatant was pipetted and replaced with 0.8ml 0.01% v/v Tween-20.

3.2.2 CHARACTERISING NANOPARTICLES

Three techniques were used to characterise nanoparticles:

(1) Ultraviolet-visible (UV-vis) Spectroscopy: This displays the AuNPs' surface plasmon resonance (SPR). As a general reference, the absorption maxima for citrate stabilised AuNPs were at a wavelength of 518nm. Indicators of aggregation include broadening of the absorption peak and a strong absorbance at higher wavelengths. UV spectra were recorded using the Cary 8454 UV-Vis (Agilent Technologies):

- Quartz 2ml cuvettes with a path length of 1cm were utilised
- At the start of each session, a 'blank' sample reading was taken (cuvette with MQ-H$_2$O)
- A reference sample consisting of non-centrifuged citrate AuNP solution utilised in the synthesis and subsequent separate samples were taken

(2) Differential Centrifugal Sedimentation (DCS): Particle size and weight distribution of AuNP particles was measured using the DCS disc centrifuge DC24000 (CPS Instruments Inc.), detecting variations at a resolution of 0.1nm. Particle size results are illustrated in the sections below.

- Fresh sucrose in MQ-H$_2$O gradient solutions from 8wt% to 24wt% were injected into the disc rotating at 24,000 rpm in 9 successive additions and left for a minimum of 45 minutes
- Before each sample measurement, 0.1 ml of diluted poly(vinyl chloride) solution (analytic Ltd, diluted 1:20 with MQ-H$_2$O) was used as a calibration standard.
- Each sample was analysed three times, with a 0.1nm variability accepted

The DCS software assumes a homogeneous density of the NP's capping layer complex for the analysis, using the value of Au. However, the capping layer has a lower density, thus distorting the analysis and therefore not providing the true particle diameter (d_{core}). The 'apparent' diameter which the software reports (d_{dcs}) represents the diameter of an NP that sediments and reaches the detector in a specified time interval 't'. The d_{core} is subsequently calculated using the approach described by Krpetic et al.,(107) based on the known thickness of the citrate layer. Subsequently, the thickness of newly added layers onto AuNPs is calculated, assuming a value of 1.5 for the capping layer density.

(3) Zeta Potential

Zeta potential allows for estimation of surface charge of NPs, which also influences its biological activity.(108)

- Folded capillary cells with Au-plated electrodes were rinsed with MQ-H$_2$O and ethanol
- 1ml of sample was inserted, ensuring no air bubbles present and the cell was capped.
- This was placed into the Zetasizer Nano (Malvern Panalytical).
- Three runs per sample was performed to confirm satisfactory measurement repeatability.
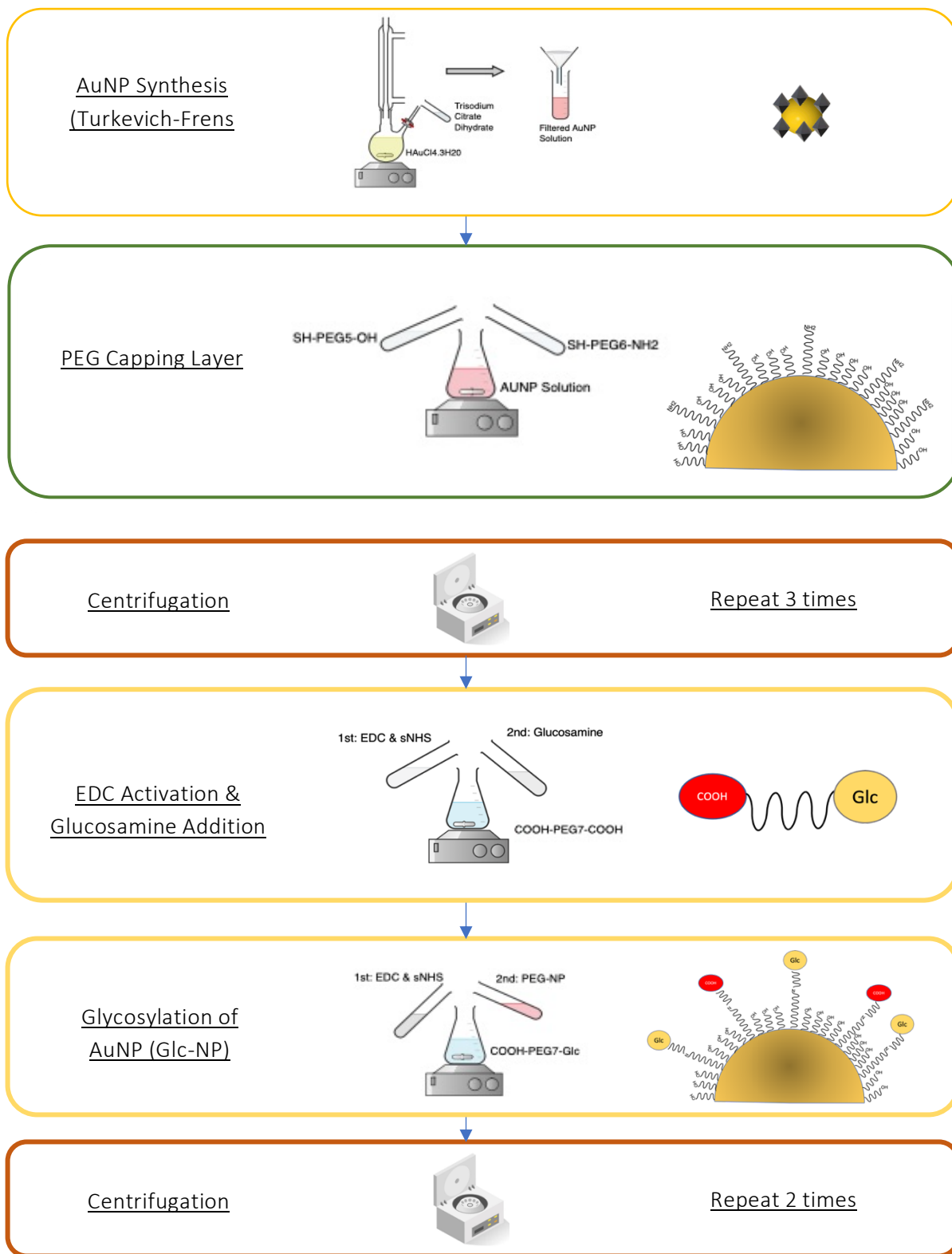
Figure 3.8: GLC-NP Synthesis Technique; Changes to Nanoparticle structure demonstrated on far right

3.3 Results & Protocol Development

3.3.1 Initial Attempt & Issues Observed

3.3.1.1 Initial Citrate Coated AuNP & PEG-NP Characterisation

AuNPs were synthesised repeatedly using the Turkevich method with no aggregation seen on both UV-vis and DCS results, giving the expected macroscopic dark red appearance.

Figure 3.9 shows the distribution of the apparent particle diameter with respect to particle number (three repeat DCS readings per sample).
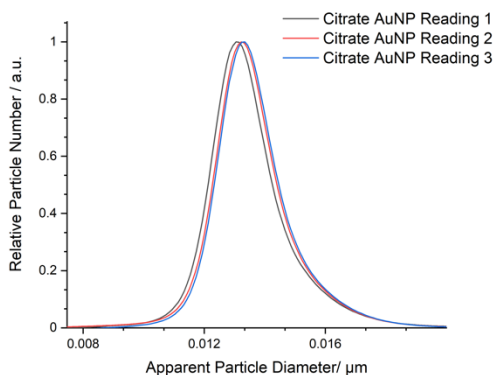
Figure 3.9: DCS Results for Citrate AuNPs (3 readings),
displaying relative particle number
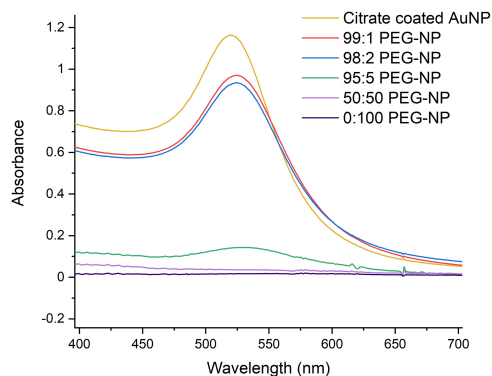
Figure 3.10: UV-vis Spectrum for various PEG-NP ratios & Citrate AuNP (ratios expressed as PEG$_5$-OH: PEG$_6$-NH$_2$)

The average apparent diameter was calculated to be 13.32nm. This translates into an actual particle diameter of 14.02nm. Given the maximal absorbance from UV-vis (Figure 3.10), an AuNP concentration of 4.47nM was confirmed. The extinction coefficient utilised for concentration estimation was 2.4×10^8 M^{-1}cm^{-1}.(109)
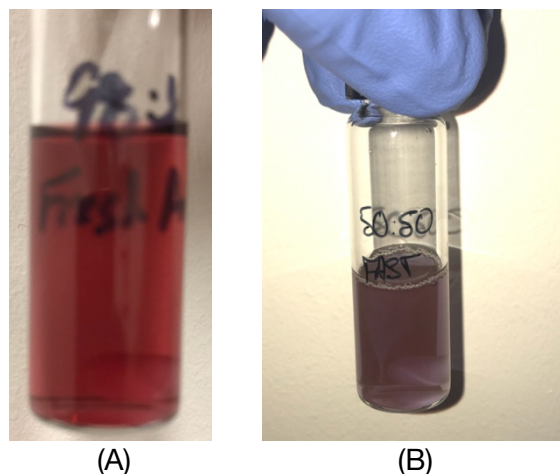
FIGURE 3.11: Macroscopic Colour Changes for PEG-NPs.
(A) Dark Red Colour (sign of np dispersion maintained) seen with a PEG5-OH:PEG6-NH2 ratio of 98:2

(B) purple colour (aggregation) seen with a PEG5-OH:PEG6-NH2 ratio of 50:50

(A)   (B)

Synthesis of PEGylated AuNPs was then attempted using PEG_5-OH:PEG_6-NH_2 at varying ratios (combined molar ratio being 2mM). The UV-vis spectrum from figure 3.10 confirms AuNPs with PEG_5-OH:PEG_6-NH_2 ratios 0:100, 50:50, and 95:5 aggregating, showing a loss in their absorbance peak and macroscopically changing colour from a dark red to purple on mixing (figure 3.11 b). Figure 3.12 demonstrates DCS results for aggregated PEG_5-OH:PEG_6-NH_2 95:5 NPs (3 readings repeated). AuNPs with PEG_5-OH:PEG_6-NH_2 ratio 97:3 did not immediately show a colour change on mixing although demonstrated this after 2 hours of mixing. NPs with PEG_5-OH:PEG_6-NH_2 ratios 99:1 & 98:2 showed a persistent absorption band with a dark red colour maintained (figure 3.11 a). This infers that if a capping layer contains more than 2% PEG_6-NH_2, the end-hydroxyl negative charges will most likely be overcome and result in amine-induced crosslinking and NP aggregation.
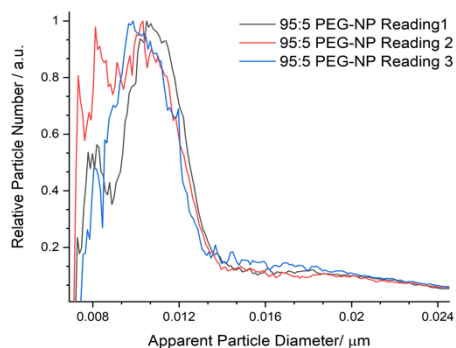
Figure 3.12: PEG_5-OH: PEG_6-NH_2 95:5 PEG-NP DCS Result for Relative Particle Number (3 Readings)

3.3.1.2 Centrifugation Limitations in the Absence of Tween-20

The initial centrifugation process was performed without using Tween-20 in the redispersing solution. Centrifugations were performed after the addition of the PEG_5-OH:PEG_6-NH_2 mixture and after the addition of glycosylated PEG reagents. This was performed three times to sediment the PEG-NPs, removing any excess re-agents within the supernatant. This avoids leaving unwanted ligands and other chemicals in solution that may instigate aggregation. However, when the PEG-NPs were centrifugated at 10900xg 8°C for 30 minutes, NPs were seen to adhere to the centrifuge tube's side walls, losing NPs and thus attaining a lower concentration. UV-spectra readings were taken after each centrifugation, as depicted in figures 3.13 & 3.14.

PEG-NPs with PEG_5-OH:PEG_6-NH_2 99:1 & 98:2 ratios showed an increasing loss of absorbance following each centrifugation. When factoring in the decline in absorbance with the decrease in volume in the final centrifugation step (1.5ml to 0.8ml), the total NP loss was estimated to be 83% and 95% for PEG-NPS with PEG_5-OH:PEG_6-NH_2 99:1 & 98:2 ratios respectively.
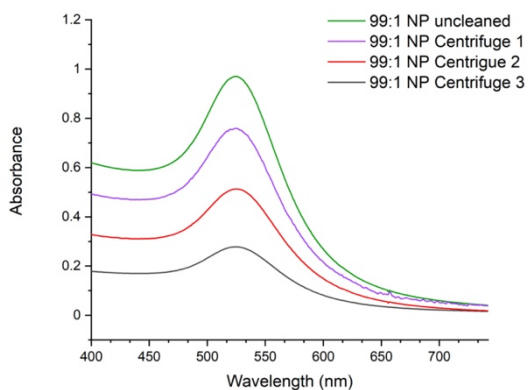
Figure 3.13: UV-vis Spectra of PEG_5-OH: PEG_6-NH_2 99:1 PEG-NP Centrifugation Steps (NOT in Tween-20)
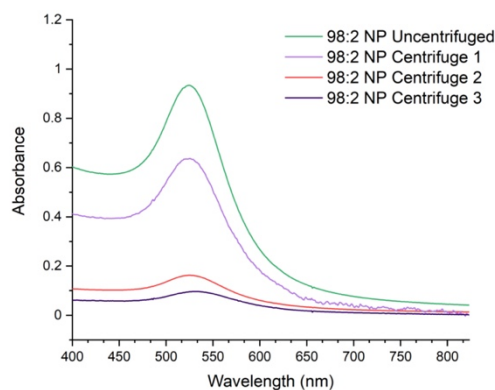
Figure 3.14: UV-vis Spectra of PEG_5-OH: PEG_6-NH_2 98:1 PEG-NP Centrifugation Steps (NOT in Tween-20)

Different settings were attempted, including using longer timings (45 & 60 minutes instead of 30), as well as higher centrifugation forces (12000 & 16000xg). However, PEG-NPs were still macroscopically seen to adhere to the walls of centrifugation tubes. 99:1 PEG-NPs were

further characterised using DCS, attaining a diameter distribution as per particle number in figure 3.15. Shell thickness was estimated to be 2.32nm for the 99:1 PEG-NPs. Despite the significant loss of PEG-NPs during the centrifugation process, the glycosylation of PEG-NPs was still attempted. The initial two EDC reactions were performed, with the final reaction mixture being mixed with 99:1 PEG-NPs in a glass container. This was left overnight and when reviewed the following day, a reddish-pink film had adhered to the glass container, with a completely colourless solution attained. UV-vis further confirmed the absence of any absorption bands.
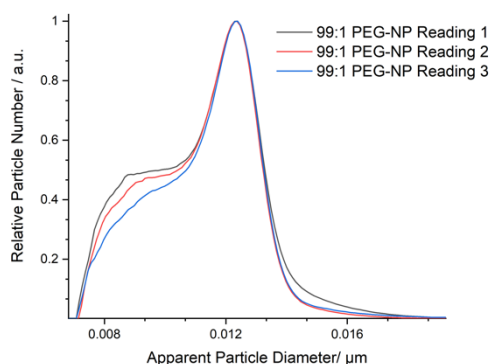
Figure 3.15: PEG_5-OH: PEG_6-NH_2 99:1 PEG-NP (NOT in Tween-20) DCS Result for Relative Particle Number (3 Readings)

3.3.2 FINAL RESULTS

An informal literature search was performed to identify similar issues encountered by other research groups. Given the successes reported when using *Tween* as an additive, *Tween-20* was introduced as during centrifugation steps for both PEG-NPs and Glc-NPs. 2 different batches of AuNPs with varying diameters were used. AuNPs with core diameters of 13.3nm and 14.0nm were used for PEG-NP and Glc-NP synthesis, respectively. PEG-NPs with a PEG_5-OH:PEG_6-NH_2 ratio of 99:1 and 98:2 were used in the final glycosylation experiments. However, lower PEG stock solution concentrations were used (1nM vs. 2nM in initial experiments).

PEG-NP's solubility improved on centrifugation, with no macroscopic PEG-NP visualised high up within the centrifuge tubes. UV-vis demonstrated a 36.4% & 36.7% decrease in NPs over 3 centrifugation cycles for PEG-NPs with PEG_5-OH:PEG_6-NH_2 99:1 & 98:2 ratios respectively (figures 3.16 & 3.17). No absorbance band was seen for Tween-20 when tested in the UV-vis spectrometer.
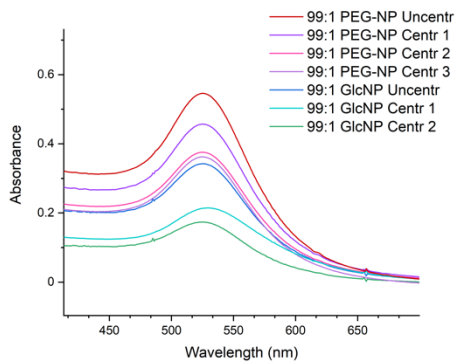
Figure 3.16: UV-vis Spectra for PEG$_5$-OH: PEG$_6$-NH$_2$ 98:2 PEG-NP & resulting Glc-NP Centrifugations (In Tween-20)
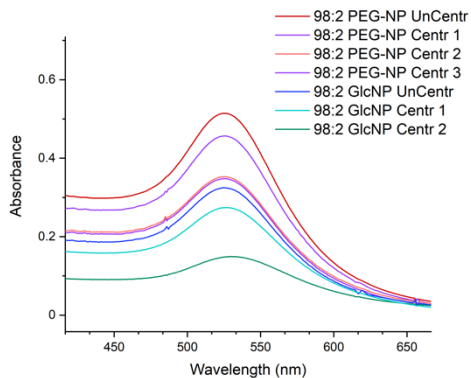
Figure 3.17: UV-vis Spectra for PEG$_5$-OH: PEG$_6$-NH$_2$ 99:1 PEG-NP & resulting Glc-NP Centrifugations (In Tween-20)
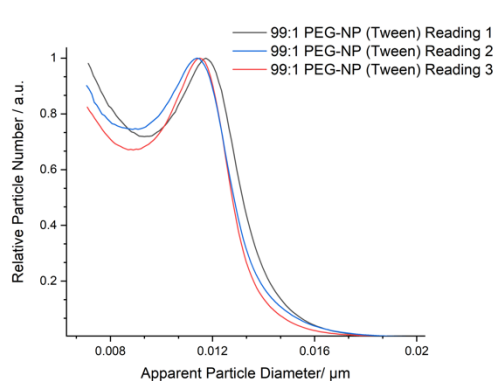
Figure 3.18: PEG$_5$-OH:PEG$_6$-NH$_2$ 99:1 PEG-NP (in Tween-20) DCS Results for Relative Particle Number
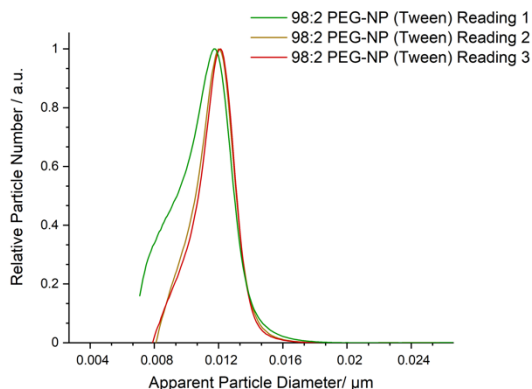
Figure 3.19: PEG$_5$-OH:PEG$_6$-NH$_2$ 98:2 PEG-NP (in Tween-20) DCS Results for Relative Particle Number
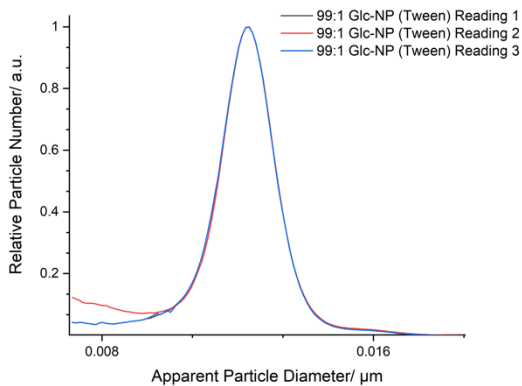
Figure 3.20: 99:1 Glc-NP (in Tween-20) DCS Results for Relative Particle Number
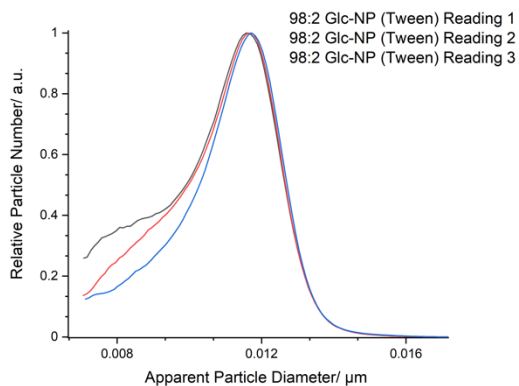
Figure 3.21: 98:2 Glc-NP (in Tween-20) DCS Results for Relative Particle Number

Characterisation with DCS was undertaken for both PEG_5-OH:PEG_6-NH2 98:2 and 99:1 PEG-NPs, as seen in figures 3.18 & 3.19, displaying the relative particle diameter distributions based on particle number. The shell thickness was estimated to be 2.0nm for 99:1 PEG_5-OH:PEG_6-NH_2 NPs and 1.8nm for 98:2 PEG_5-OH:PEG_6-NH_2 NPs, again agreeing with prior results of Krpetic et al.(107)

Glycosylation of the PEG-NPs was attempted in the presence of Tween-20 according to the protocol described above. However, only two centrifugation rounds were undertaken to cleanse the Glc-NPs, with 0.8mL added after the second cleansing step. UV-vis readings for each cleansing step of the cleansing process shown in figures 3.16 (PEG_5-OH:PEG_6-NH_2 98:2) & 3.17 (PEG_5-OH:PEG_6-NH_2 99:1). This does not show any evidence of NP aggregation, with no peaks at higher absorbance values. DCS characterisation was also performed, as shown in figures 3.20 and 3.21. The shell thickness for NPs in tween was estimated to be 2.2nm for 99:1 Glc-NP and 3.1nm for 98:2 Glc-NP. The shell thicknesses for PEG-NPs & Glc-NPs (*in Tween-20*) is summarised in table 3.1. The shell thickness and actual AuNP diameters were calculated as stated in subsection 3.2.2, considering the peak apparent diameters seen in DCS figures demonstrated in this results section. Two different AuNP solutions (with variation in NP diameter per solution) was utilised, hence the difference in diameters seen in table 3.1.

	Actual Diameter/ Shell Thickness
AuNP Diameter	13.31
99:1 PEG-NP (in Tween-20) – S.T	2.0 +/- 0.25
98:2 PEG-NP (in Tween-20) – S.T	1.8 +/- 0.25
AuNP Diameter	14.02
99:1 PEG-Glc (in Tween-20) – S.T	2.2 +/- 0.2
98:2 PEG-Glc (in Tween-20) – S.T	3.1 +/- 0.3

Table 3.1: Change in Shell Thickness Through the Addition of PEG & Glc. S.T; shell thickness

Zeta potential readings were also taken at each modification step. All NPs tested, except for citrate AuNPs, were dissolved in Tween-20 0.01% v/v :

- Citrate AuNPs: Zeta potential of -36.5mV (Standard deviation of 16mV)
- 99:1 PEG-NPs: Zeta potential of -0.85mV (Standard deviation of 4.97mV)
- 98:2 PEG-NPs: Zeta potential of -13.8mV (Standard deviation of 9.25mV)
- 99:1 Glc-NPs: Zeta potential of -21.1mV (Standard deviation of 8.1mV)
- 98:2 Glc-NPs: Zeta potential of -25.7mV (Standard deviation of 7.5mV)

3.4 DISCUSSION

The characterisation results attained are encouraging and give a strong indication that synthesis was successful to some extent, albeit they did not definitively confirm the Glc-NP structure. Section 3.4.1 & 3.4.2 discusses the initial obstacles encountered during the synthesis of a glycosylated AuNP: achieving a viable PEG reagent ratio and NP loss through centrifugation and adherence to its container's walls. Section 3.4.3 reviews the significance of characterisation results.

3.4.1 FINDING BALANCE IN THE PEG REAGENT RATIO

Our group has experience of synthesising PEG-NPs, as witnessed in the Krpetic et al paper.(107) In Krepetic et al's study, AuNPs were coated with thiolated PEG chains of different lengths and shell thickness ascertained using DCS characterisation. The outward terminals consisted solely of hydroxyl groups, serving to repel AuNPs and prevent aggregation.

The initial PEG-coating layer in this thesis presented with a challenge of balancing amine and hydroxyl terminal groups. Amine groups harbour the potential for cross-linking between AuNPs and aggregates, due to their high affinity to Au. This was clearly shown when utilising PEG_5-OH:PEG_6-NH_2 ratios 0:100, 50:50 & 95:5 as the initial PEG layer, resulting in a purplish solution confirming aggregation. However, both PEG_5-OH:PEG_6-NH_2 ratios 99:1 and 98:2 PEG-NPs did not show aggregation, whereby a lower amount of amine-terminated PEG reagents limits the

amount of glucose molecules attached. When considering the PEG_5-OH:PEG_6-NH_2 ratios 99:1 and 98:2, approximately 36 and 72 amine groups would be available in the outer layer, respectively. This estimate considers that the average surface area of a 13.32nm diameter AuNP is 556nm^2, capable of housing 3622 ligands (6.5 PEG ligands per nm^2).(94,110) In this chapter we solely explored the attachment of glucose to the amine groups, although RB may be further attached in a similar fashion to the NP as glucose, functionalising AuNPs for PDT. If hypothetically one would consider an equal ratio in glucose and RB attachment, the PEG_5-OH:PEG_6-NH_2 98:2 ratioed PEG layer would attain a similar number of glucose and RB molecules when compared to our previous theoretical bilayer (PAH/PSS) AuNP structure (Figure 3.5).

Interestingly, PEG-NPs with a PEG_5-OH:PEG_6-NH_2 ratio of 95:5 and 97:3 did not immediately exhibit macroscopic signs of aggregation and may merit further investigations. Tween-20 merits consideration in this regard, as it has demonstrated 'anti-aggregative' properties in other steps leading up to a Glc-NP (section 3.4.2). An alternative approach to increase the PEG_6-NH_2 ratio would be to attempt a *'PEG substitution'* approach. This consists of initially capping citrate AuNPs with solely PEG_5-OH and then, under the right conditions, incubate in a PEG_6-NH_2 solution. This is done with the intention of ligand exchange between unbound PEG_6-NH_2 and bound PEG_5-OH, without expecting significant crosslinking, given the lack of free surface area available on the PEGylated NPs. However, quantifying the extent of ligand exchange may be quite challenging. Utilizing PEGs with a molecular weight of 2000 as an initial capping layer is another strategy worth thinking about because the literature shows that using larger PEG chains reduces NP aggregation.(102)

3.4.2 TWEEN-20: THE MISSING PIECE

Polysorbate 20, commonly referred to as Tween-20, is a non-ionic surfactant that has been promoted in several studies attempting surface modifications to AuNPs.(28,111–114) Zhao et al. confirmed that Tween-80 prevented PEG-modified AuNP aggregation (whilst Tween-80's absence increased aggregation following centrifugation).(112) A red-shift in absorbance peaks seen after exposing AuNP solutions to polysorbate referenced Tween's surfactant adsorption onto the AuNPs, with similar results seen in this study. Interestingly, Zhao et al. confirmed that Tween-80 (compared to other polysorbates with shorter alkyl chains) showed the best

dispersity performance when performing centrifugation and resuspension. They concluded that longer alkyl chains allow for a thicker adsorbed polysorbate layer on AuNPs, presenting the PEGylated capping layer with more stability.(112) Farfan-Castro et al. functionalised their AuNPs with HS-PEG-NH$_2$, to synthesise a nano-vaccine for coronavirus 2019. The authors remarked on Tween-20's essential role in preventing particulate loss through adherence to their containers, as well as prolonging their AuNPs stability for months.(115) These two papers propelled the inclusion of Tween into this study, with three significant improvements.(112,115)

Firstly, its inclusion reduced PEG-NP loss from repeat centrifugations. The overall PEG-NP loss was reduced by an average of 0.55 (from 83% down to 36.4%) and 0.61 (from 95% down to 36.7%) in 99:1 and 98:2 PEG-NPs respectively (figures 3.12 & 3.13). The importance of the surfactant is further underlined when considering that a change in centrifuge setting did not affect NP losses. However, this facet of the synthesis technique requires further investigation and confirmation through reproducibility since UV-vis spectra after each centrifugation were taken only once.

Secondly, the surface adsorption of Tween-20 onto Glc-NPs prevented adherence to the container's wall, allowing for completion of Glc-NP synthesis. However, on reviewing the UV-vis spectra from figures 3.16 & 3.17, a significant loss of NP still occurred following centrifugations. 59% of PEG$_5$-OH:PEG$_6$-NH$_2$ 99:1 ratioed Glc-NPs and 75% of PEG$_5$-OH:PEG$_6$-NH$_2$ 98:2 ratioed Glc-NPs were lost following two consecutive centrifugation rounds, despite the addition of Tween-20. Zhao et al. provided a potential solution towards this, as explained above. Tween-80 showed an improvement in AuNP stability, due to an increased number of hydrophobic methylene chains having a carbon-carbon double bond present in its alkyl chain. This may provide an outlook to improving upon Glc-NP retention following centrifugation.(112) Furthermore, the Tween-20 concentration used may be further increased, with the 0.01% concentration used based on studies that used NPs with different capping layers. A higher concentration (0.1%) used by our group in subsequent experiments has given an indication that this may further decrease NP loss, although requires more in-depth investigations.

Finally, the use of Tween-20 also inadvertently improved the accuracy of DCS readings. This was seen when comparing size distributions for PEG$_5$-OH:PEG$_6$-NH2 99:1 ratioed PEG-NPs in the presence and absence of Tween-20. The former's size distributions are narrower and reproducible. The reasoning behind this was accidentally observed when neat Tween-20

readings were taken on the DCS centrifuge immediately following readings for PEG$_5$-OH:PEG$_6$-NH$_2$ 99:1 ratioed PEG-NPs (not in Tween-20). As seen in figure 3.22, the initial 'readings' for neat Tween-20 demonstrate remnant PEG-NPs from prior experiments, affirmed from a diminishing DCS signal at the exact same size of the previously measured PEG-NPs. The last repeat Tween-20 reading (reading 3) does not show any absorbance. This infers that PEG-NPs were partly sticking to the glass wall of the centrifuge after

Figure 3.22: Tween-20 DCS Results for Relative Particle Number

injection, moving down at a slower rate until reaching the sucrose solution.

3.4.3 CHARACTERISATION & SHELL THICKNESS SIGNIFICANCE

The PEG-NP shell thickness values are within reasonable agreement with previous measurements published in the Krpteic et al. paper, with their PEG$_5$ shell thickness quoted at 2.1nm.(107) Both PEG$_5$-OH:PEG$_6$-NH$_2$ 98:2 & 99:1 ratioed PEG-NP shell thickness (1.8nm & 2nm respectively) are similar.

The shell thickness increases for the Glc-NPs, potentially indicating the conjugation of a glycosylated PEG reagent to the PEG-NP's capping layer. This provides the strongest evidence from characterisation investigations that the glycosylation protocol has been successful. However, other side-products are produced from consecutive EDC reactions (section 3.1.5), including EDC-PEG$_{11}$-COOH chains. These would not house glucose at their end-terminals and when considering the ratio of different products described in Figure 3.4, it is likely that approximately 50% of bound ligands have a glucose moiety. This is made on the presumption that different EDC intermediates have the same reactivity towards PEG$_6$-NH$_2$ ligands on PEG-NPs. Given that all EDC intermediates have the same EDC-PEG$_7$ structure, their differing end terminal is far away from the reactive EDC terminal and therefore unlikely to influence the reaction. EDC intermediates favouring NP crosslinking and aggregation did not show any observable concerns from UV-vis and DCS results, with no indication of Glc-NP aggregation.

Zeta potential results provide more information on the surface charge of AuNPs at differing stages of the synthesis. As a reference, nanoparticles with a zeta potential between −10 and +10 mV are considered approximately neutral, while nanoparticles with zeta potentials of greater than +30 mV or less than −30 mV are considered strongly cationic and strongly anionic, respectively.(108) Opinions are divided in the literature whether zeta potential plays an influential role in uptake, with cationic NPs experiencing more favourable uptake by negatively charged cell membranes. However, Voigt et al. and other studies argued that other NP characteristics, including use of surfactants, increase NP permeability across the blood brain barrier and cell membranes.(116) Citrate AuNPs in this experiment displayed a similar zeta potential as prior experiments performed by Dr. Broadbent.(24) Given the standard deviations, there were no significant differences in PEG_5-OH:PEG_6-NH_2 ratioed 99:1 & 98:2 PEG-NPs. Glc-NPs demonstrate a more negative charge compared to the PEG-NPs. This gives a weak indication that glycosylation has taken place. During our EDC/ glycosylation reactions, PEG_7-COOH (section 3.1.5) is an incidental side product that may attach to the PEG-NPs' outer layer (figure 4.6 (b)). At neutral pH the end carboxyl terminals are deprotonated and may be contributing to the perceived Glc-NPs' negative charge.

3.5 CONCLUSIONS

This chapter details a newly established synthesis strategy for the glycosylation of citrate coated AuNPs using thiolated PEG reagents. The protocol was developed and issues with regards to appropriate PEG_5-OH:PEG_6-NH2 ratios and NP loss through centrifugations were addressed and optimised. Tween-20 surfactant played a major role in ensuring dispersion throughout the various synthesis steps and reduced NP loss through centrifugation.

The finalised synthesis protocol achieved our objective of a non-aggregated Glc-NP solution, with subsequent photophysical metrics supporting the proposed nanostructure. This included a persistent absorption band on UV-vis spectra and increasing shell thickness calculated via DCS readings, hinting towards the glycosylation of the AuNP's capping layer. Whilst these investigations do not provide definitive proof, they provide a strong basis to move forward onto *in vitro* cellular uptake experiments, as described in chapter 5.

CHAPTER 4: QUANTIFYING NANOPARTICLES' CELLULAR INTERNALISATION

4.1 ETCHING GOLD NANOPARTICLES

4.1.1 INTRODUCING GOLD ETCHING

Inductively coupled plasma optical emission spectroscopy (ICP-OES) is a conventional investigative tool used to quantitatively analyse the amount of NP uptake.(37,117) Dr. Chadwick has previously identified the uptake rates of NPs in HeLa cell lines utilising varying NP concentrations over different incubation times with this apparatus.(41) This method entails incubating cell plates in AuNP solution for a specified time. A haemocytometer is used to count the cells after they have been tryptanised off the well plate's surface. Centrifugation is used to separate the cell pellets from its solution before they are dissolved in Aqua regia, along with any AuNPs attached to or inside the cells. The final solution is submitted for Au concentration measurement through use of ICP-OES. The final Au concentration and total cell count permits the estimation of the number of AuNPs per cell (specific for AuNP concentration and incubation time).

However, this does not distinguish cell surface adsorption from actual cellular internalisation of AuNPs. NPs bound to PSAs need to be internalised so that singlet oxygen produced during PDT can cause the most cytotoxic damage in its brief lifetime (singlet oxygen required to inflict cytotoxic injury lasts microseconds, discussed in Chapter 1). Glc-NPs are being hypothesised to be taken up via GLUT1-mediated endocytosis, although section 2.2 discusses limited current evidence of GLUT1 endocytosis. Dreifuss & Motiei et al. have provided evidence suggesting that this is a viable route.(82,83) This chapter review of potential 'gold-etching' solutions that would seek to differentiate Glc-NP cellular entry from cell surface adsorption. An etching solution would dissolve AuNPs adhered to the cell surface and therefore remove the AuNPs from the cell surface on washing cell dishes. This step would be performed before trypanising cells from the well's surface and attaining a cell count.

Au etching is a well-established method in the field of microfabrication of electromechanical systems, including nanodevices.(117,118) Reviewing wet etching methods for Au, there are two key considerations:

1. **‘Complexing’ Ligand**: such as cyanide, chloride, iodide and thiourea; preventing Au atoms from binding to each other, forming stable Au(x) complexes
2. **Oxidant**: provides a stage for the ligand to dissolve AuNPs

This is an electrochemical reaction; whereby Au atoms are oxidised to Au^+ and form a complex with the ligand. The electrons generated by this anodic reaction are consumed by the oxidant in a cathodic process.(117)

4.1.2 THE IODINE SYSTEM AS A GOLD NANOPARTICLE ETCHANT

The iodide system is one of the commonest etching techniques, where a combination of potassium iodide (KI) salt and iodine (I_2) is used. The tri-iodide ion (I_3^-) is synthesised through reaction 1. Reactions 2 & 3 represent the anodic (complexing ligand binds) and cathodic (oxidant is reduced) reactions, respectively:

$$\text{Reaction 1: } I_2 + I^- \rightarrow I_3^-$$
$$\text{Reaction 2: } Au + 2I^- \rightarrow AuI_2^- + e^-$$
$$\text{Reaction 3: } I_3^- + 2e^- \rightarrow 3I^-$$
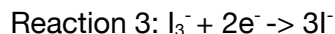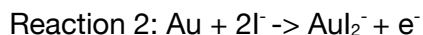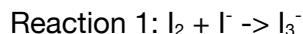
The overall reaction for etching of Au can be condensed as follows:

$$2Au + I_2 + 2I^- \rightarrow 2\ AuI_2^- \text{ (119)}$$
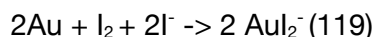
Equation 4.1: Condensed Iodine Etching Reaction of Gold

The condensed reaction indicates that one I_2 molecule is required to etch away two Au atoms. This reactive system operates in a near-neutral pH range, with low toxicity. In a mixing ratio of I_2:KI of 1:6, the etch rate is quoted at 2.8nm/s at room temperature. This can be improved by raising the temperature, where a $10^{\circ}C$ rise would virtually double the etch rate.(120) Compared to other etching reagents such as cyanide and bromide, I_2 is less toxic and hazardous and Au etching occurs more rapidly with I_2.(117)

The I$_2$ etching system has been applied to the field of NPs and nanomedicine. Various publications outline the use of NPs or nanorods as sensors, whereby I$_2$ etching decreases the Au's absorption wavelength depending on the 'sensed' molecule's concentration (such as glucose, or I$^-$ itself).(121)

Cho et al. presented a methodology for distinguishing internalised NPs from NPs adsorbed onto the cell surface (figure 4.1), through I$_2$ etching. Experiments were performed on human breast cell line (SK-BR-3).(122) . Their cell cultures were first incubated in AuNP solution (17.7nm diameter) and washed with phosphate buffered saline (PBS) to wash away non-bound and non-internalised NPs. Cell plates were exposed for 5 minutes to a I$_2$/KI solution (ratio 1:6) with 0.34mM concentration of I$_2$ before being washed in PBS. This etched away AuNPs adhered to the cell's surface membrane, allowing for intra-cellular AuNPs to be quantified using Inductively Coupled Plasma Mass Spectrometry (ICP-MS). Citrate coated AuNP solution did not demonstrate any significant difference in their ICP results whether the I$_2$/KI solution was introduced or not, indicating that these NPs were taken up by cells. However, when poly-allylamine coated AuNPs were used with and without I$_2$/KI solution incubation, there was a substantial difference in ICP results. This strongly suggests that a significant fraction was bound to the cell surface, with the iodine etchant reducing the ICP measured Au content.(122)
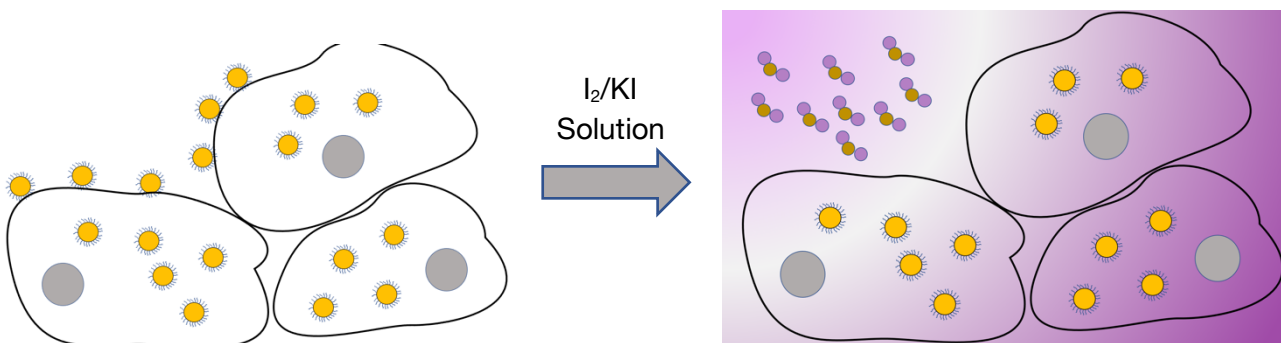
FIGURE 4.1: Iodine Etching of Extracellular AuNPs. Yellow spheres represent AuNPs, purple spheres represent Iodine Atoms and gold spheres represent Gold Atoms.

4.1.3 CONCERNS OVER REPORTED OUTCOMES & IODINE'S CYTOTOXICITY

Cho et al.'s novel approach was taken into consideration for differentiating between NP cell surface adsorption and internalisation. However, two primary concerns required further investigation. Firstly, I$_2$'s stated etching capability at 0.34mM to etch a given number of AuNPs

per cell has not been backed up by experimental validity or references. Cho et al. stated that when 1ml of 0.34mM I_2/KI solution was used, 10,000 AuNPs per cell were dissolved; with no investigations or specific results to back this up. Secondly, iodine toxicity was quantified with 3-(4,5-dimethylthiazol-2-yl)-2,5-diphenyltetrazolium bromide (MTT) assays, with no comment on reproducibility. Whilst MTT assays confirm the cells' physiologically activity, cell membrane permeability is not investigated. Two potential errors need to be considered from this method:

1. <u>false negatives</u>: quiescent cells that have an intact membrane may not demonstrate physiological activity and produce negative test results
2. <u>false positives:</u> Physiologically active cells with excessively porous membranes may have more AuNP "leakage", which could cause these to be etched away by extracellular iodine and provide an underestimated final Au concentration

Cho et al. used a low I_2/KI concentration of 0.34mM to improve cytotoxicity results in their MTT cell viability assays. For this reason, the I_2 system was favoured over thiourea, whereby diluting the latter's concentration did not allow them to attain a similar etching capacity. However, I_2's cytotoxicity remained time critical, with cell viability decreasing from over 90% with a 5-minute incubation interval to approximately 30% if left for 30 minutes.(122) I_2's cytotoxicity is well documented in the medical field, being commonly used in different facets of practise as povidine-iodine, for its cytotoxic effect. It is used in surgery as a washing agent after excising a tumour in the attempt to kill off any seeded or fragmented cancer and as an antiseptic for wound care.(118) Cell line experiments speculate I_2 having anti-proliferative effects through DNA and mitochondrial inhibition, as seen in breast cancer lines.(123) Delivery of complexed I_2 can result in cell membrane disruption,(118) a further antiseptic pathway that was acknowledged whilst developing this protocol.

4.1.4 AIMS & OBJECTIVES FOR DEVELOPING A RELIABLE AuNP ETCHING PROTOCOL
The aim and objectives of this chapter were to incorporate iodine etching into the current AuNP uptake quantification protocol for ICP-OES. This chapter is sub-divided into three sections, investigating both I_2's etching capacity at millimolar concentrations and its toxicity profile (on both cellular cytotoxicity and membrane integrity) to formulate a reliable I_2 etching protocol for

AuNPs. Section 4.2 investigates and validates the etching efficacy of the I_2 system at low concentrations, utilising UV-vis spectroscopy whilst reacting citrate coated AuNP with I_2/KI solution. Section 4.3 seeks to confirm Cho et al.'s I_2 cytotoxicity results through repeat MTT assays, whilst Section 4.4 investigates cellular membrane integrity through trypan blue experiments.

4.2 VALIDATING THE ETCHING PERFORMANCE OF THE IODINE SYSTEM

4.2.1 AUNP & I_2/KI UV-VIS SPECTRA TO CONSIDER

The performance of relatively low I_2/KI concentrations as a Au etchant was investigated in this subsection. To capture UV-vis spectra of etching events in "real time," etching operations were conducted inside a quartz cuvette. Before every experimental session, the baseline absorbance spectra for I_2/KI and AuNP solutions were taken.

The following absorption band values for the iodine system were considered when performing UV-vis spectroscopy. Absorption spectra for the iodide ion (I^-) centres around a wavelength of 226nm (approximately 20nm wide), whilst molecular iodine has a broad absorption band at 203nm (40nm wide). The tri-iodide (I_3^-) complex demonstrates an absorption spectrum shift from a decrease in the 203nm wavelength absorption to two new bands on wavelengths of 288nm and 352nm. This confirms that I_2 molecules are converted into I_3^-.(124) The different absorption bands relating to the iodine system do not interfere with AuNPs' plasmon band (centring around a wavelength of 520nm). Therefore, UV-vis spectroscopy will seek to review a decrease in AuNPs' absorption bands (without I_2 spectra masking this band), ergo confirming the minimum concentration and time required for an I_2/KI solution to etch away AuNPs effectively.

4.2.2 UV-VIS & ETCHING METHODOLOGY

- Both iodine (I_2) and potassium iodide (KI) were added to MQ-H_2O in a pre-determined molar ratio (either 1:6 or 1:10) and placed in a sonicator for a minimum of one hour, to ensure dissolution of solute particles. When citing the I_2/KI solution's concentration in subsection 4.2.3, this refers to the I_2 concentration (rather than combined I_2 & KI concentrations)

- UV-vis instrument Cary 8454 UV-Vis (Agilent Technologies) was set up and a 'blank' sample consisting of MQ-H_2O was used to record the background, using Quartz 2ml cuvettes with a path length of 1cm
- A pre-determined concentration (usually 1nM) of citrate AuNP solution was added in a chosen solvent (either MQ-H_2O, Dulbecco's Modified Eagle Medium (DMEM) or phosphate buffer saline (PBS))
- A UV-vis absorbance reading was taken at this point (prior to the addition of I_2/KI solution)
- Varying concentrations of I_2/KI solution were added attaining a total volume of 2ml in the cuvette
- UV-vis absorbance readings were taken every 30 to 60 seconds (time denoted as '0 seconds' referred to the moment I_2/KI solution was added into the cuvette)

4.2.3 PERCENTAGE OF AuNP ETCHED: CALCULATIONS

I_2's baseline absorbance at 520nm cannot be simply deducted from reaction's absorbance at 520nm (AuNP's plasmon band) to determine the percentage AuNP etched. During the etching procedure, I_3^- & I_2 are consumed to form AuI_2^-, resulting in a shift in iodine's baseline absorbance throughout the reaction. A more accurate approach is considered in equation 4.2. If the average of the absorbance values at 500nm and 554nm is equal to the absorbance at 520nm when the reaction's absorbance is measured after 5 minutes, there is no discernible persisting NP absorbance. This would confirm that Au has been etch away completely. To confirm the equation's validity, this was applied to the baseline absorbance spectrum of I_2/KI solution, attaining a 100% value each time.

$$\% \, AuNP \, Etched = \left\{ \frac{((Abs5min_{500} + Abs5min_{554})/2)}{Abs5min_{520}} \right\} X \, 100\%$$

Equation 4.2: Percentage of AuNP Etched

4.2.4 UV-VIS SPECTRA RESULTS

Initial reactions were tested at room temperature in MQ-H_2O solution. When a '0 second' reading was taken, this represented a UV-vis measurement performed on mixing the I_2/KI solution with the AuNP solution.

Figure 4.2 demonstrates spectra for 2ml containing 0.34mM I_2/KI and approximately 1nM citrate-coated AuNP solution. One can appreciate 2 absorbance bands at lower wavelengths (approx. 298 and 348nm) for I_2/KI solution and an absorbance peak at 518nm for the AuNP solution. Figure 4.3 shows an immediate decline in the AuNP absorbance band in the presence of 0.34mM I_2/KI solution (1:6 molar ratio). This was trialled with citrate AuNPs in PBS and DMEM. The former presented an identical absorption band decline as figure 4.3. The addition of DMEM generated an immediate absorption band at 560nm that persisted over the 5-minute period, although the AuNPs' 518nm absorption band was no longer detected (figure 4.4).
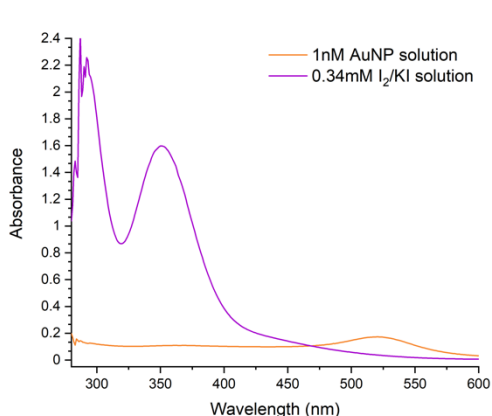
Figure 4.2: 0.34mM I_2/KI (1:6 molar ratio) & 1nM AuNP Absorption Bands
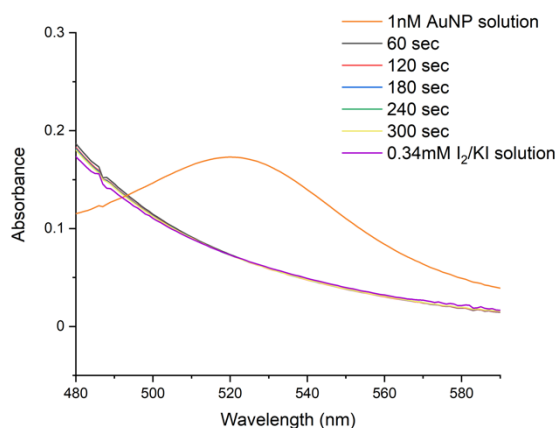
Figure 4.3: 1nM AuNP Etching (in MQ-H_2O) with 0.34mM 1:6 I_2/KI solution
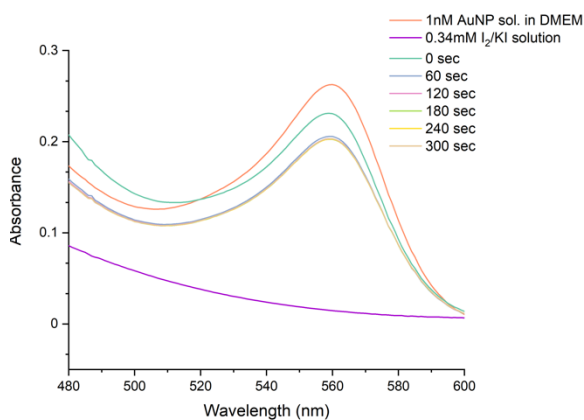
Figure 4.4: Citrate AuNP Etching (in DMEM) with 0.34mM I_2/KI solution

Lower I_2/KI concentrations (molar ratio maintained 1:6 I_2/KI) were subsequently tested, using MQ-H_2O as a solvent. I_2/KI concentrations included 0.17mM, 0.1275mM, 0.085mM and 0.0425mM), with experiments performed at room temperature. The 0.17mM and 0.1275mM solutions revealed similar etching efficacies as figure 4.3. 0.085mM I_2/KI concentrations showed a slower etching rate (as depicted in figure 4.5), whilst an AuNP absorbance band persisted when in the presence of 0.0425mM I_2/KI (figure 4.6). Thus, a 0.085mM I_2/KI concentration was identified as the lowest concentration showing a near-complete etching reaction. Furthermore, both 0.085mM and 0.0425mM I_2/KI solutions underwent etching reactions with AuNP solutions at a higher, more physiologically representative temperature of 37^OC, using different I_2:KI molar ratios (1:6 and 1:10) with MQ-H_2O as a solvent. Results are depicted in figures 4.7 to 4.10. Table 4.1 summarises the percentage of AuNP etched in a five-minute period.

AuNP Conc. (nM)	I^2/KI Conc. (mM) (Molar ratio)	Figure ref.	Abs_{520}	Average Abs_{500} & Abs_{554}	% AuNP Etched in 5 mins
1.0	0.34 (1:6)	4.3	0.072	0.145	100
1.0	0.0425 (1:6)	4.5	0.15	0.11	73
0.69	0.0425 (1:6)[1]	4.7	0.1	0.076	76
0.5	0.0425(1:10)[1]	4.7	0.05	0.039	77
1.0	0.085 (1:6)	4.5	0.06	0.055	92
1.0	0.085 (1:6)[1]	4.8	0.023	0.0214	93
1.2	0.085 (1:10)[1]	4.8	0.12	0.095	79

Table 4.1: Summary of Percentage of AuNP Etched in MQ-H2O.
Conc.: concentration, ref.: reference, Abs: Absorbance, 1: reaction performed at 37 deg Celsius
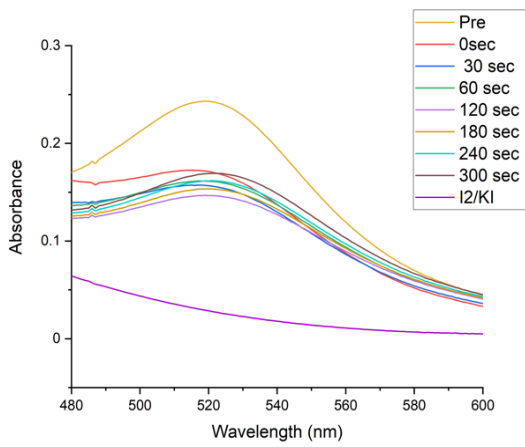
Figure 4.5: 1nM AuNP Etching (in MQ-H_2O) at room temperature with 0.0425mM 1:6 I_2/KI
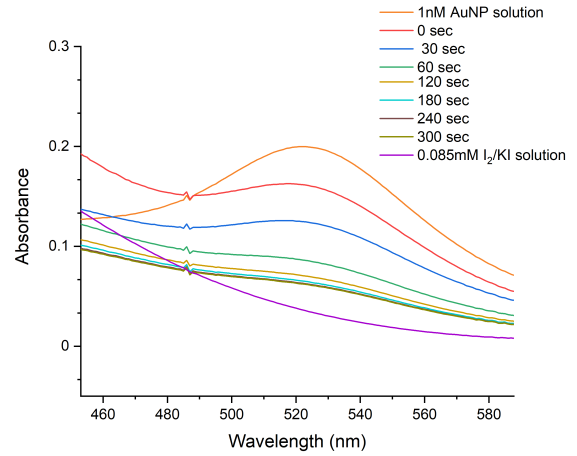
Figure 4.6: 1nM AuNP Etching (in MQ-H_2O) at room temperature with 0.085mM 1:6 I_2/KI
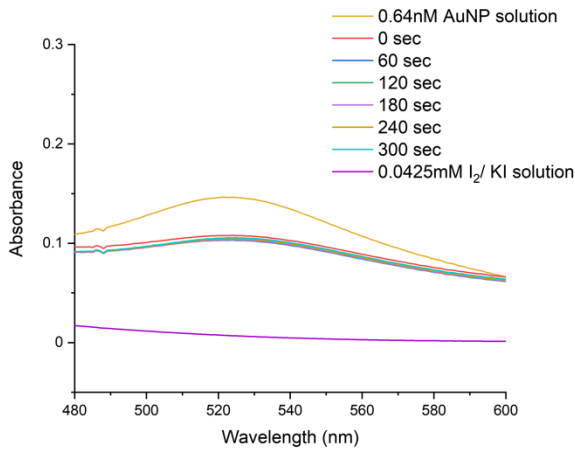
Figure 4.7: 0.64nM AuNP Etching (in MQ-H_2O) at 37°C with 0.0425mM 1:6 I_2/KI
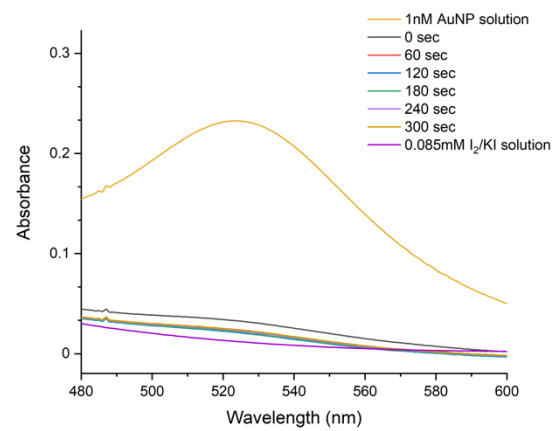
Figure 4.8: 1nM AuNP Etching (in MQ-H_2O) at 37°C with 0.085mM 1:6 I_2/KI
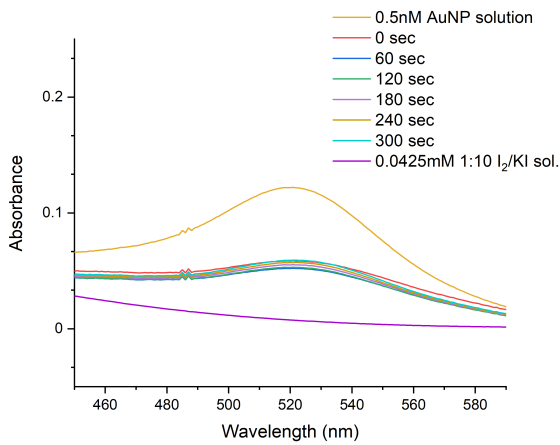
Figure 4.9: 0.5nM AuNP Etching (in MQ-H_2O) at 37°C with 0.0425mM 1:10 I_2/KI
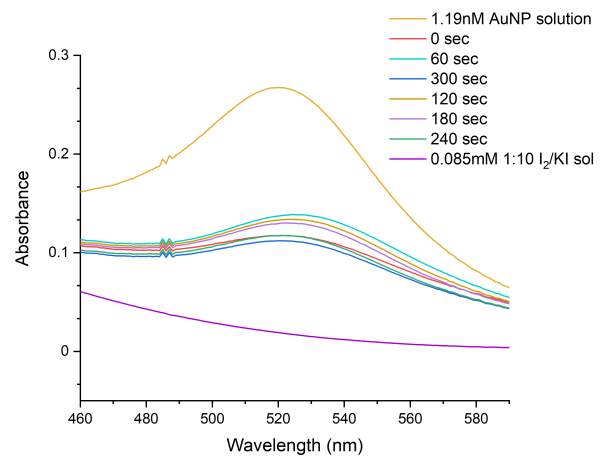
Figure 4.10: 1.2nM AuNP Etching (in MQ-H_2O) at 37°C with 0.085mM 1:10 I_2/KI

4.2.5 REVIEWING THE ETCHING CAPACITY OF LOW I_2 CONCENTRATIONS IN 5 MINUTES

Equation 4.1 clearly demonstrates the need for a minimum of one I_2 molecule to etch two Au atoms, i.e. an I_2:Au of greater than 0.5. Our experimental conditions sought to determine the lowest I_2/KI concentration to etch away AuNPs within a 5-minute period. Cho et al. demonstrated that 0.34mM successfully etched away a citrate coated AuNP solution within a 5-minute interval. Figure 4.3 further corroborates this statement, with 0.34mM I_2/KI solution etching away 1nM AuNP solution on stirring. Lower I_2/KI concentrations were pursued to see if these may etch away AuNP solutions within a similar timeframe, whilst providing the potential for improving its cytotoxic profile. 0.17mM and 0.1275mM I_2/KI concentrations provided similar results, i.e., almost instantaneous etching of 1nM AuNPs. 0.085mM and 0.0425mM I_2/KI concentrations were further tested; etching 73% & 92% of a 1nM AuNP solution respectively. The reaction required between 180-240 seconds to etch 92% of NPs (as opposed to 0.34mM I_2/KI solution's etching profile).

No significant difference in etching rate was seen on utilising a more physiological temperature at low I_2 concentrations. The 0.085mM I_2/ KI concentration did not show an appreciable difference (92% vs 93%), whilst the 0.0425mM I_2/KI concentration did not demonstrate an increase in NPs etched despite using a lower 0.64nM AuNP solution when raising the temperature to 37 deg Celsius (73% vs 76%). When increasing the I_2:KI ratio from 1:6 to 1:10 at 37 deg Celsius, the 0.0425mM I_2/KI solution showed a minimal increase in %NP etched, despite the AuNP solution's concentration again being reduced. The 0.085mM I_2/KI 1:10 solution (37 deg Celsius) showed a decline in %NP etched, likely due to the increase in AuNP solution's concentration to 1.2nM. These results suggest that at low Au & I_2 concentrations, the reactants' concentrations are more likely to drive the equilibria of these reactions than temperature or I_2:KI molar ratio changes.

These etching experiments were considered within a 5-minute timeframe. This is due to Cho et al.'s I_2 toxicity results, with a significant decline in cell viability after 5 minutes of cell incubation with I_2/KI solution (as per their MTT assay results). Liang et al.'s review confirms that etching reactions may persist for hours,(125) and these experiments do not negate the possibility of the AuNP solution being fully etched over longer time intervals. From these results, a 0.085mM I_2/Ki solution was the lowest concentration sufficient to etch away most NPs (93% of a 1nM AuNP solution).

4.3 Iodine's Cytotoxic Effect on Cell Physiology

4.3.1 I_2/KI Solution Toxicity: Testing Cho et al.'s Results

Colorimetric assays using 3-(4,5-dimethylthiazol-2-yl)-2,5-diphenyltetrazolium bromide (MTT) were performed to determine the physiological impact of I_2/KI solutions on HeLa and 74A cancer cell lines. The tetrazolium ion is reduced by physiologically viable cells into a formazan precipitate. Subsequently, Dimethyl Sulfoxide (DMSO) is added to solubilise the precipitate and quantify through an absorbance reading at 570nm.(126) The highest I_2/KI concentration utilised for this experiment was 0.34mM, with results attained by Cho et al. showing higher concentrations, such as 0.5mM gave a 60% cell viability or less.(122)

Two standards were utilised per experiment: a 'PBS' & 'DMEM' standard. The PBS standard consisted of three PBS washes before and after incubating wells in PBS (replicates the iodine incubation process, without iodine present). This served as the control through which the 'relative' cell viability could be calculated (equation 4.3, see below), thereby assessing the effect of iodine on cell viability. The 'DMEM' standard (no washes during experiment, well incubated in DMEM) served as a further comparison with the PBS standard to review whether washes and/or PBS solution use during incubation were affecting cell viability.

4.3.2 MTT Assay Methodology

- I_2/KI solution was initially prepared as per section 4.2.2., attaining an I2:KI ratio of 1:6. Varying concentrations of I_2 (referenced in results as 'I_2/KI concentration') used in these experiments were prepared by diluting the stock solution in phosphate buffered solution (PBS - pH of 7.1-7.5 and osmolality of 275-304 mOs/kg)
- HeLa & 74A cells cultures were grown in T74 flasks, reaching a 70-80% confluency
- These were washed once with 10ml PBS and passaged, seeding an appropriate number of cells in either a 96-well or 6-well flat-bottomed plate
- The cell plates were incubated in Dulbecco's Modified Eagle Medium (DMEM) in a 5% carbon dioxide incubator at $37^{O}C$ for 24 hours, monitoring until 80% confluence was reached
- A predetermined number of wells were designated for I_2/KI solution exposure, whilst the remaining well plates were classified as 'DMEM' or 'PBS' standards

- Wells subjected to iodine cytotoxicity testing were initially washed three times with PBS
- These were subsequently incubated in I_2/KI solutions, with varying I_2 concentrations for a specified time-period (3 to 5 minutes), washed a further three times in PBS and submitted to 3-(4,5-dimethylthiazol-2-yl)-2,5-diphenyltetrazolium bromide (MTT), as below
- 'DMEM' standard wells were washed with PBS once and subsequently subjected to MTT (see below)
- 'PBS' standard wells were washed three times with PBS, incubated in PBS solution for the 5 minutes as well plates incubated in I_2/KI solutions and washed a further three times in PBS before subjected to MTT solution (see below)
- 5mg/ml MTT solution, together with DMEM, was applied to each well plate and incubated at 37 ^{O}C in the dark for 3 hours
- MTT solution was then removed, paying careful attention to not disturb the formed crystals, equivalent amounts of Dimethyl Sulfoxide (DMSO) pipetted into each well and allowed to settle for 15 minutes
- A SpectraMax Plus-384 spectrophotometer 96 well plate reader was used to measure the absorbance at 590nm
  When 6-well plates were used, the remaining DMSO solutions from each plate was transferred to 96-well plates to allow for automated absorbance reading

- Mean absorbance value was derived from wells incubated in identical conditions being investigated (Abs$_{Mean Cond}$)
- The 'PBS' standard absorbance values (Abs$_{PBS}$) were taken as the standard to calculate the relative cell viability (RCV) using equation 4.3:

$$Relative\ Cell\ Viability\ (\%) = \frac{Abs_{Mean\ cond}}{Abs_{PBS}}$$

Equation 4.3: Relative Cell Viability calculation for a specified well

4.3.3 MTT ASSAY RESULTS

The first MTT assays were performed in 96-well plates using HeLa cell cultures. Despite several attempts, results attained lacked reproducibility and contained a large standard error range between wells exposed to identical incubation conditions. Comparisons were made between

PBS and DMEM standards using various PBS washing steps, noting that these issues likely stemmed from cell loss during PBS washing steps.

This led to the use of 6-well plates (with HeLa cell lines), with each well having thirty times the surface area when compared to a 96-well plate (9.6cm^2 vs. 0.32cm^2). This allowed for more careful handling and less disruption of the cell layer on removing and adding solutions to the wells, thereby reducing the shear forces caused by the flow of liquid during washing. Each well plate was set up as demonstrated in Figure 4.11, with 'PBS' and 'DMEM' standards set up as described in the methodology section 4.3.2. I$_2$/KI concentrations 0.34mM and 0.17mM (I$_2$:KI ratio of 1:6) were investigated with five-minute incubation periods, using the 'PBS' standard as the control when calculating the RCV. The test was replicated ten times for reproducibility and summarised in Figure 4.12, together with standard error bars.
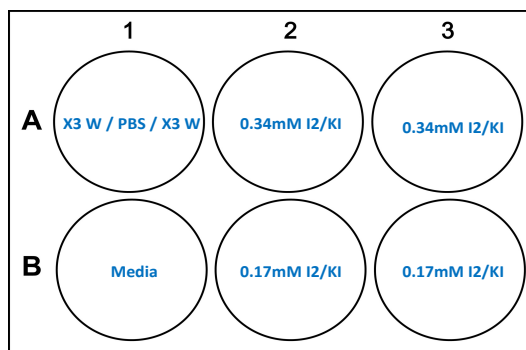
Figure 4.11: 6 well plate setup
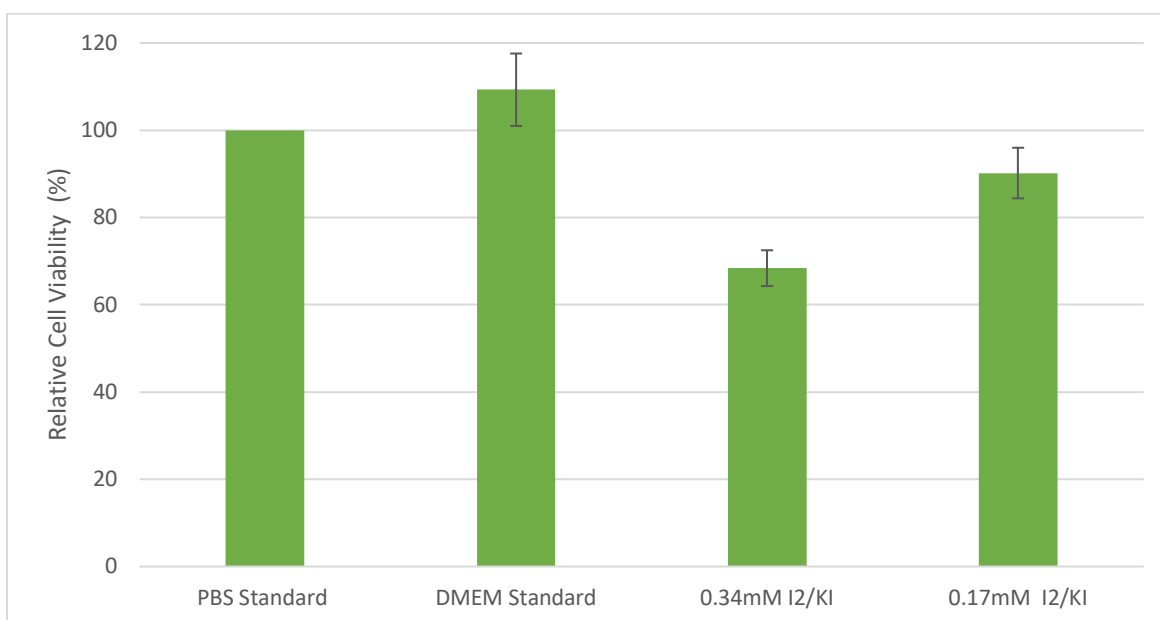
Figure 4.12: HeLa MTT Assay in 6 Well-Plates RCVs in varying PBS, DMEM & I$_2$/KI concentrations (I$_2$:KI molar ratio 1:6) incubated for 5-minutes

The 6-well plate template (Figure 4.11) was replicated in the 74A cell line (repeated in four separate well plates): utilizing varying I$_2$/KI concentrations with an I$_2$:KI molar ratio of 1:6 and five-minute incubation periods (figure 4.13).
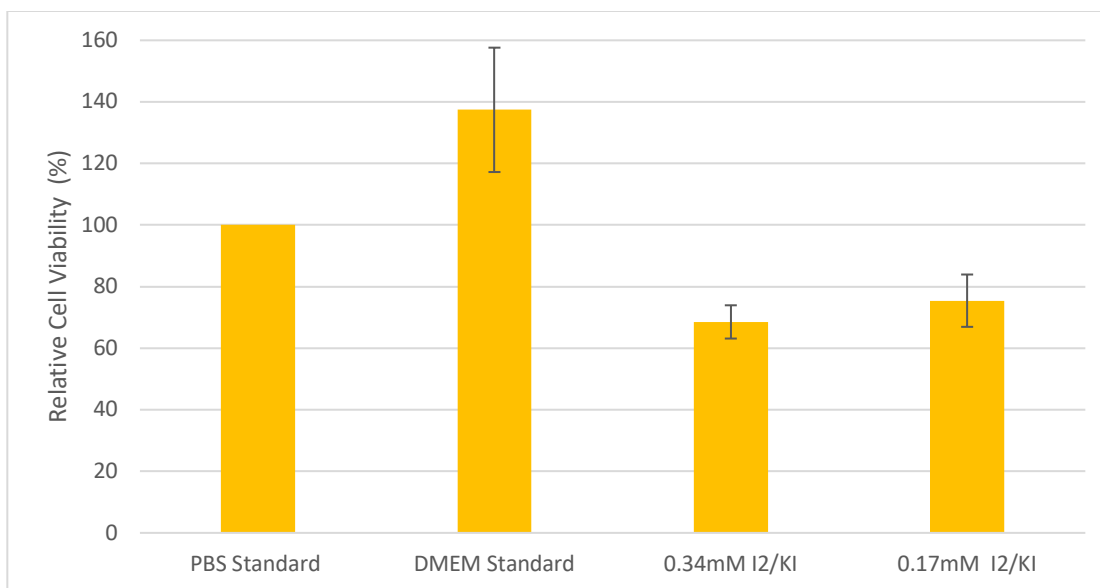
Figure 4.13: 74A MTT Assay in 6 Well-Plates RCVs in varying PBS, DMEM & I_2/KI concentrations (I_2:KI molar ratio 1:6) incubated for 5-minutes

4.3.4 REVIEWING IODINE'S CYTOTOXIC EFFECT THROUGH MTT ASSAYS

Initial MTT assays performed in 96-well plates showed significant variability between plates with the same incubation conditions and I_2/KI concentrations, with a wide standard error range. Given the small area per well, questions were raised regarding washes and transfer of solutions resulting in cell disruption and loss. Further experiments varied the number of washes in PBS & DMEM standards as a means of confirming these concerns. Although a significant variability persisted, the results hinted towards a decline in RCV with increased PBS washes. 6-well plates were then utilised to attempt and reduce well variability with identical experimental conditions, investigating an initial I_2/KI concentration of 0.34mM identified by Cho et al. as well as a lower 0.17mM concentration. 0.34mM & 0.17mM I_2/KI solutions provided an RCV of 68% & 90% in the HeLa cell line (figure 4.12), and an RCV of 68% & 75% in the 74A cell line (figure 4.13).

Our MTT assays (figure 4.12 & 4.13) contradict Cho et al.'s results; whereby 0.34mM I_2/KI solution demonstrated a greater than 80% viability in a human breast cancer cell line. This may be due to the use of a different cell line that is potentially less susceptible to the iodotoxic effects of I_2/KI solutions. Whilst Cho et al. did not report their result reproducibility and standard deviations, they utilised 6-well plates for their experiments, which provided more consistent results in this thesis' assays. From a physiological perspective, I_2/KI concentrations of 0.17mM

or less would be required in HeLa (RCV 90%) and 74A cells (RCV 75%) to maintain a respectable cellular physiological viability.

Tetrazolium-based assays have been used to determine the cytotoxicity of various drugs and their effects on the mitochondrial electron-transport chain,(127,128) although this does not reflect on cell membrane stability (CMS). For the future purpose of incorporating the I_2/KI etchant into an NP cell-internalisation quantification protocol; I_2's toxic influence on CMS would provide further insight into the generation of false positive results and is considerably more important than solely analysing the physiological impact of I_2/KI solutions. This led us to explore I_2/KI solution's cytoskeletal disruption effects through trypan blue staining (section 4.4).

4.4 IODINE'S CYTOTOXIC EFFECT ON CELL MEMBRANE STABILITY

4.4.1 TRYPAN BLUE STAINING: A COMPLEMENTING INVESTIGATION FOR IODINE CYTOTOXICITY

Trypan blue staining was included as a part of iodine's cytotoxicity investigations, allowing a more comprehensive understanding of cancer cells' membrane stability (CMS) in I_2/KI solution. Quantifying cell membrane disruption would provide a better understanding of the quantity of AuNPs that 'leak' out from within cells due to I_2's membrane disruption. Cells with disrupted membranes would still be counted (even though these would not hold any AuNPs), resulting in an underappreciation of the true Au concentration and hence number of AuNPs per cell. Trypan blue staining would permit better assessment of the extent of false positives discussed in subsection 4.1.3, when compared to MTT assay's more limited approach to investigating cells' physiology.

The crux of the trypan blue staining method involves ascertaining the number of cells stained with trypan blue (versus those which are not) after I_2/KI solution incubation. Cell staining with trypan blue indicates increased permeability of the cell membrane due to iodine's cytotoxic profile. Phosphate buffer saline (PBS) and Dulbecco's Modified Eagle Medium (DMEM) standards were also undertaken with each experiment (see methodology below). These acted as controls, establishing a baseline cell membrane permeability for each cell line, allowing a *relative* CMS percentage to be calculated using the PBS standard. This reduced the false positive rate for this investigation, whereby already porous cell membranes pre-iodine

exposure may contribute to the result. The 'DMEM' standard allowed for comparisons as to whether washes and incubation in PBS (rather than DMEM) may be affecting CMS results.

4.4.2 Trypan Blue Staining Methodology & Calculations

- Stock I2/KI solutions were prepared as detailed in subsection 4.2.2, utilising both 1:6 and 1:10 I2/KI molar ratios. Varying I_2 concentrations were achieved using phosphate buffered saline (PBS) and a dilutant
- HeLa, 74A & UM-SCC-6 cell types were incubated in 35mm cell dishes with 2ml of Dulbecco's Modified Eagle Medium (DMEM) for 24 hours at $37^O C$ in a 5% carbon dioxide incubator
- A predetermined number of cell dishes were designated for I_2/KI solution exposure, whilst the remaining dishes were classified as with a 'DMEM' or 'PBS' standard
- Cell dishes designated for iodine solution exposure were initially washed with 1ml PBS, incubated in 2ml of differing I_2/KI solution concentrations and washed a further three times with 1ml PBS washes
- 'DMEM' standard dishes underwent one wash with 1ml phosphate buffered saline (PBS)
- 'PBS' standard dishes underwent three 1 ml PBS washes, were incubated for five minutes in 2ml of PBS solution and then underwent a further three 1ml PBS washes

- All cell dishes were exposed to 250uL trypsin for 5 minutes.
- Microscopy was used to confirm that cells had detached off the cell dish's surface & 750uL of DMEM was added to each cell dish
- 10uL sample was taken from each cell plate and mixed with 10ul of 0.4% trypan blue (Invitrogen, ThermoScientific)
- After 1 minute, 10uL of the trypan blue/ cell solution mixture was taken for cell counting, using both a manual haemocytometer and an automated cell counter, *Countess 3FL (Invitrogen, ThermoScientific)*
- A minimum of two separate samples were used for counting to reduce false positive results
- The number of cells with an intact cell membrane (referred to as *absolute* CMS) was calculated as displayed in equation 4.4. A mean *absolute* CMS was estimated per condition investigated

$$Absolute\ CMS = \frac{Unstained\ cells - cells\ stained\ with\ trypan\ blue}{total\ number\ of\ cells}$$

Equation 4.4: Calculating the Absolute Cell Membrane Stability (% cells with an intact membrane)

- 'PBS' standard was used as the control when expressing the *relative* CMS, calculated as displayed in equation 4.5.

$$Relative\ CMS = \frac{Absolute\ CMS}{Absolute\ CMS\ of\ PBS\ standard}$$

Equation 4.5: Calculating the Relative Cell Membrane Stability

4.4.3 TRYPAN BLUE STAINING RESULTS

The HeLa cell line was initially subjected to trypan blue testing. Varying I_2/KI solution concentrations (referring specifically to I_2 concentrations), incubation intervals and I_2/KI molar ratios were tested, as listed below:

- 0.17mM I_2/KI solution, five-minute incubation interval (Molar I_2/KI ratio 1:6)
- 0.17mM I_2/KI solution, three-minute incubation interval (Molar I_2/KI ratio 1:6)
- 0.085mM I_2/KI solution, five-minute incubation interval (Molar I_2/KI ratio 1:6)
- 0.0425mM I_2/KI solution, five-minute incubation interval (Molar I_2/KI ratio 1:6)
- 0.0425mM I_2/KI solution, five-minute incubation interval (Molar I_2/KI ratio 1:10)

Each experimental condition was trialled on a minimum of three separate cell dishes, with 'PBS' and 'DMEM' standard cell dishes also prepared per experimental condition, as described in the methodology section 4.4.2. Results for the mean *relative* CMS rates are shown in figure 4.16, with standard error presented by the error bars. When comparing the mean *relative* CMS of the DMEM and PBS control, there is a 4% difference, indicating that PBS as a dilutant for I_2/KI etching solution has a minor impact on CMS. A low *relative* CMS was seen when using 0.17mM I_2/KI solutions, with a mean *relative* CMS of 46%. Shortening the incubation period from 5 to 3 minutes did not improve the *relative* CMS (46% vs 44%). However, the *relative* CMS improved on incubation with lower concentrations, whereby 0.085mM I_2/KI concentration showing a mean *relative* CMS of 88%. 0.0425mM I_2/KI concentrations were experimented with

molar ratios 1:6 and 1:10 (I2:KI). The higher molar ratio demonstrated a lower relative CMS (93.2 vs 109.1%).
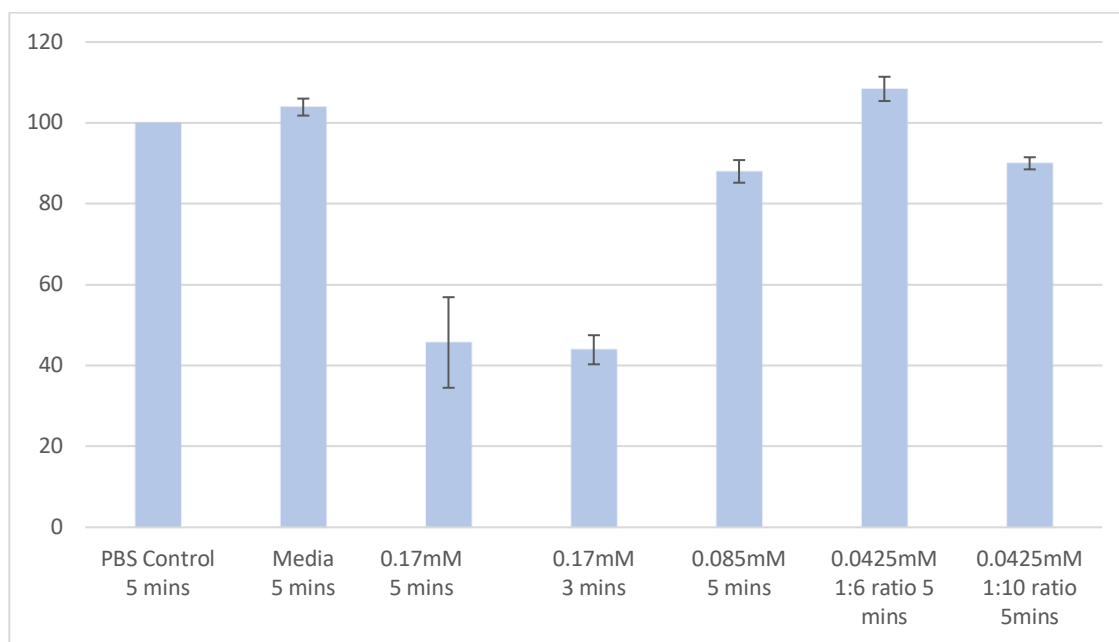
Figure 4.14: HeLa Trypan Blue Assay: Mean Relative CMS for PBS, DMEM controls & varying I_2/KI solutions (I_2:KI molar ratios 1:6 & 1:10) at 3- and 5-minute incubation periods

The trypan blue experiment was further trialled on the 74A and UM-SCC6 cell lines, utilising 0.085mM & 0.0425mM I2/KI solutions, with a five-minute incubation interval (Molar I_2/KI ratio 1:6) as shown in Figure 4.17. 0.085mM I_2/KI etchant was the highest concentration investigated in these cell lines, given HeLa's trypan blue assay results with higher concentrations. Each incubation medium was repeated four times for the 74A cell lines and two times for the UM-SCC6 cell line. Interestingly, in both cell lines the use of PBS did not have any effect on CMS, as seen when comparing PBS and DMEM results. The mean *relative* CMS percentage at 0.085mM I_2/KI concentrations was calculated to be 90% for both 74A and UM-SCC6. Trypan blue staining experiments confirmed a relative CMS of higher than 80% in all three cell lines when using 0.085mM I_2/KI concentration.
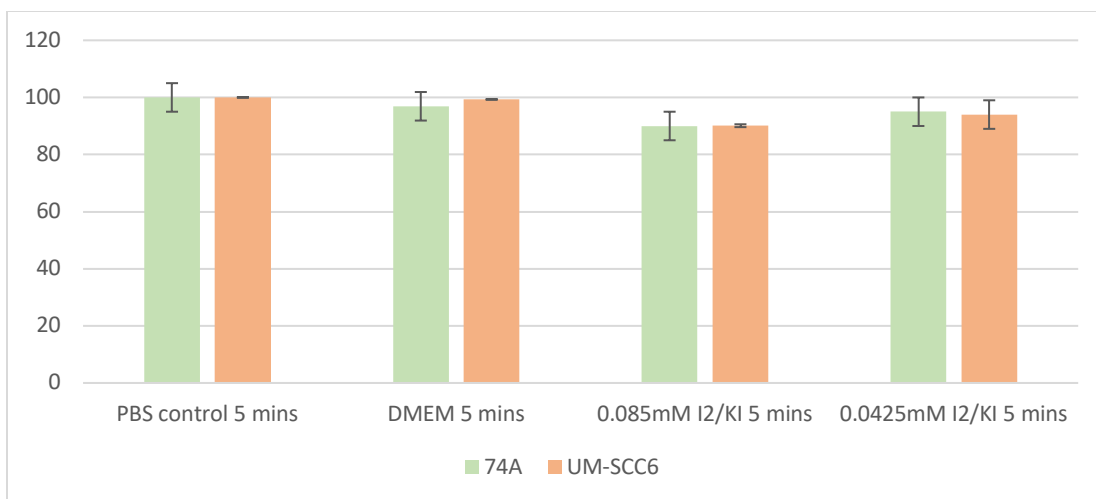
Figure 4.15: 74A & UM-SCC6 Trypan Blue Assay: Mean Relative CMS for PBS, DMEM controls & varying I_2/KI solutions (I_2:KI molar ratios 1:6) at 5-minute incubation periods

4.5 CONCLUSIONS ON IODINE ETCHING & CYTOTOXICITY

Cho et al.'s article provides a unique insight into Au etching on a NP scale. Reviewing its 625 citations, none have attempted to replicate results published in this letter. Some studies citing the paper have instead attempted to implement this etching reaction in nanoparticle biosensors for Au detection.(121) This chapter sought to replicate Cho et al.'s technique, as this would provide substantial evidence regarding NP cell entry (rather than simple cell surface adsorbance). Confirming NPs' cell entry ensures that our NP-PDT therapeutic strategy can progress and may serve to fundamentally progress the other NP-centered research projects (as witnessed by Cho et al's numerous citations). Cho et al's results were investigated in terms of I_2/KI solution's etching efficacy at millimolar concentrations, as well as its cytotoxicity impact on ICP measurements for NP internalisation.

Etching experiments examined by UV-vis spectroscopy confirmed that 0.085mM I_2/KI solution (molar ratio 1:6 I_2:KI) was the lowest concentration that successfully etched away over 90% of a 1nM AuNP solution in a 5-minute period. MTT assays assessing I_2/KI cytotoxicity did not correspond with Cho et al.'s findings. 0.34mM I_2/KI solution demonstrated a lower RSV in both HeLa and 74A cell lines, whilst the 0.17mM I_2/KI solution showed a higher RCV of 90% & 75% respectively. In trypan blue assays, a lower concentration at 0.085mM I_2/KI was required to reach a relative CMS value of 88% in the HeLa cell line, also being well tolerated in 74A and

UM-SCC6 cell lines (both exhibiting a 90% relative CMS). Moving forwards, a 0.085mM I_2/KI solution (molar ratio 1:6 I_2:KI) was considered for quantification of NP internalisation in NP uptake experiments, providing an adequate Au etching (93% 1nM AuNP solution) and CMS profile (88-90% in HeLa, 74A & UM-SCC6 cell lines).

CHAPTER 5: ASSESSING NANOPARTICLE UPTAKE & INTERNALISATION

5.1 INTRODUCTION

A Glc-NP synthesis technique has been discussed in Chapter 3, with promising characterisation results. Cell experiments would provide more conclusive proof of AuNP glycosylation; where comparisons of Glc-NP uptake is increased in GLUT1-rich cells when compared to GLUT1-deprvied cell uptake. A subsequent line of investigation would seek to look at whether Glc-NPs are internalised or simply adhering to the cell surface, using the iodine etching technique described in chapter 4. Our group's previous work utilised Inductively Coupled Plasma Optical Emission Spectroscopy (ICP-OES), with Dr. Broadbent attaining uptake profiles for HeLa and UMSCC cell lines using both citrate AuNPs and the bilayer NP structure with RB (Chapter 1, figure 1.5).(24) ICP-OES analyses elements at a concentration of parts per billion/ million and the technique is used in several research settings. It utilises emission spectra to confirm and quantify elements in the studied sample.(129)

In this study, HeLa and 74A cell lines were reviewed for potential inclusion in AuNP internalisation experiments. HeLa was chosen for continuity, given the available data for this cell line within the Volk team's database, whilst the 74A cell line was representative of OPSCC. In the literature, the HeLa cell line was shown to overexpress the GLUT1 & GLUT2 isoforms through Western Blot analysis.(130) GLUT1 expression in 74A cell line was measured in a separate study, with GLUT1 staining confirming its presence on 74A cells' surface.(131)

5.2 METHODOLOGY

Our groups' ICP technique was utilised for uptake experiments, incorporating an additional iodine etching step to review NP cellular internalisation.

- A pre-determined number of cells were grown in 10cm dishes with DMEM for 24 hours
- 4nM AuNP solution was mixed in a 1:1 ratio with DMEM culture media overnight, attaining a 2nM AuNP concentration
- DMEM was removed from the cell plates and 10ml of the AuNP:DMEM solution applied for 3 hours to each cell plate
- Three 10ml PBS washes were applied to each cell plate to completely remove the AuNP:DMEM solution
- 2ml of trypsin was applied for 5 minutes, then 8ml of DMEM was added (once confirming that cells were detached from the plate surface via microscopy).
- 10uL representative sample was taken for manual cell counting using a haemocytometer
- 9ml of the remaining solution was pipetted into a 15ml falcon tube
- Each falcon tube was centrifuged using the *Heraus Megafuge 8R Centrifuge* at 1000xG $8^{\circ}C$ for 10-minutes
- Media supernatant was removed via pipette and aqua regia solution (375uL hydrochloric acid and 125uL nitric acid) applied to each cell pellet to prepare the samples for ICP-OES. This was allowed to stand for 3 days after vortexing for 1-minute
- 4.5ml of MQ-H_2O was added to each sample prior to submission for ICP-OES analysis of gold (Au) concentration
- For each condition, uptake experiments were repeated a minimum of three times per cell line and an Au salt solution (pre-determined concentration) was sent per submission as a standard.

When assessing solely for NP cellular internalization, the following alteration in methodology was carried out after incubating cells with the AuNP/ DMEM solution:

- AuNP:DMEM solution was removed after its 3 hour incubation period and three 10ml PBS washes applied to each cell plate
- 10ml of 0.085mM I_2/KI solution (molar ratio 1:6 I_2:KI) was applied to the cells for 5 minutes and each cell plate washed three times with 10ml of PBS

Otherwise, the rest of the technique was carried out as described above.

Samples were sent off to the analytical lab for ICP-OES analysis. An estimate of each sample's Au concentration (mg/L) was given, allowing for calibration of instruments with standards within the submitted concentration estimates. Results received confirmed the actual concentration of Au (mg/L) per sample. The NP diameter attained from prior DCS results (emphasising the importance of precise NP sizing), together with Au concentration, was then used to calculate the number of Au atoms per NP. This allowed for an accurate estimate of the number of AuNPs per cell; dividing the quantity of AuNPs in the 5mL sample by the total cell count.

NP Cellular internalisation investigative experiments using I_2/KI solution further utilised the above calculation to confirm the quantity of NPs per cell. From Chapter 4's trypan blue assays, up to 15.5% (± 4%) & 4.6% (± 3%) of HeLa and 74A cells may experience cell membrane instability, resulting in NP leakage from the cell's cytoplasm. This may produce an underestimation of AuNPs per cell and was considered when reviewing results.

5.3 PRELIMINARY RESULTS & DISCUSSION

The results of NP uptake tests using citrate-coated AuNP, PEG-NP, and Glc-NP in both HeLa and 74A cell lines are summarised in Tables 4.1 and 4.2. The final "AuNP number per cell" represents an average of the three biological repeats per NP uptake experiment, together with the corresponding standard deviation to consider result inter-variability.

NP tested	Final Au Conc: mg/L (st dev)	Final cell count (st dev)	No. of AuNP in Final Sample	No. of AuNP per cell (st dev)
Citrate AuNP (25/7/22)	3.09 (0.032)	4.4×10^6 (4.2×10^4)	6.2×10^{11}	158,615 (30,000)
Citrate AuNP I$_2$/KI etched (25/7/22)	3.63 (0.039)	4.4×10^6 (1.2×10^4)	7.2×10^{11}	183,163 (29,000)
99:1 Glc-NP (04/08/22)	0.01 (0.01)	3.5×10^6 (1.5×10^5)	2.7×10^9	771 (500)
98:2 Glc-NP (04/08/22)	0.02 (0.02)	4.3×10^6 (1.5×10^5)	4.0×10^9	930 (655)
98:2 PEG-NP (19/08/22)	0.02 (0.01)	8.3×10^6 (11,000)	4.4×10^9	530 (600)
98:2 Glc-NP (19/08/22)	0.03 (0.05)	5.6×10^6 (5,000)	5.8×10^9	1050 (300)

Table 5.1: HeLa NP Cell Uptake & Internalisation. St dev: Standard deviation

NP tested	Final Au Conc: mg/L (st dev)	Final cell count (st dev)	No. of AuNP in Final Sample	No. of AuNP per cell (st dev)
Citrate AuNP (25/7/22)	0.92 (0.015)	1.7×10^6 (4.4×10^5)	1.85×10^{11}	126,000 (50,000)
Citrate AuNP I^2/KI etched (25/7/22)	0.73 (0.016)	1.6×10^6 (5×10^4)	1.47×10^{11}	101,000 (10,000)
99:1 Glc-NP (04/08/22)	0.07 (0.05)	4.5×10^6 (5.6×10^4)	1.3×10^{10}	3000 (240)
98:2 Glc-NP (04/08/22)	0.023 (0.01)	4×10^6 (1.3×10^5)	4.6×10^9	1200 (400)
98:2 PEG-NP (19/08/22)	0.04 (0.03)	1.2×10^6 (6,000)	5.8×10^9	4800 (570)
98:2 Glc-NP (19/08/22)	0.013 (0.01)	1×10^6 (13,000)	2.5×10^9	2500 (800)

Table 5.2: 74A NP Cell Uptake & Internalisation. St dev: Standard Deviation

The citrate AuNP uptake in HeLa cells was estimated to be 158,000 NPs/cell. This is 3.76 times the results previously achieved by Dr. Broadbent & Dr. Chadwick, where value of 42,000 NPs/cell was recorded under the same incubation conditions (2nM citrate AuNPs incubated at 3 hours).(24,41) Dr. Chadwick further confirmed her results with both ICP-OES and transmission electron microscopy.(41) Due to this discrepancy, the above experiment was repeated a further 11 times, with an average of 120,000 NPs/cell (standard deviation: 50,000 NPs/cell).

After the protocol was scrutinized to rule out errors and disparities, cell size measurements of cell line used for this project were taken and compared to previous HeLa cell sizes recorded by the Volk team. The Invitrogen EVOS M5000 microscope was used to estimate the average cell length (Figure 5.1). This was noted to be 115μm, 3.8 times that of the Dr. Broadbent's previous measurements of a separate HeLa cell line (cell diameter estimated at 30μm).(24) As seen in figure 5.1, the cells utilised in these experiments have a more elongated appearance than those used previously by Dr. Chadwick (Figure 5.2).(41) These results hint towards a linear relationship between the cells' surface area and uptake; an increase in surface area permitting more endocytic-related cellular activities.(132) Although HeLa cell lines originate from the same patient, it is well known that these cell lines have mutated over the years and are not a suitable standard.
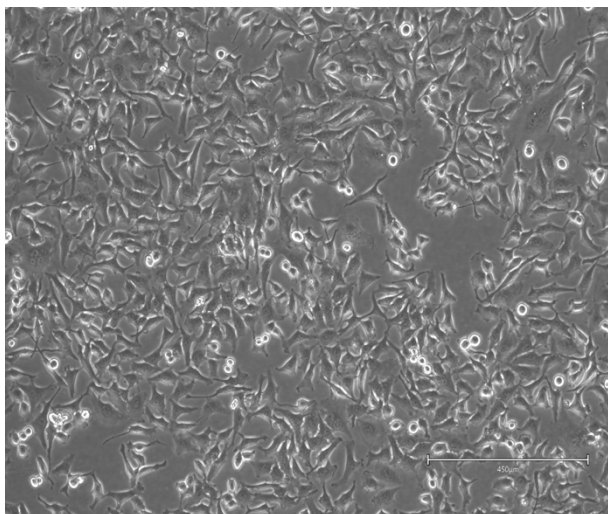
Figure 5.1: Thesis HeLa Cell Culture, scale bar at 450um
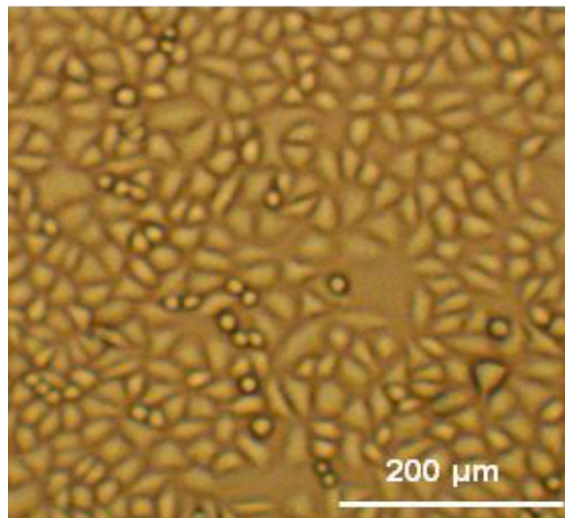
Figure 5.2: Chadwick HeLa Cell Culture(41)

The iodine etching experiments for citrate coated AuNPs in both HeLa and 74A cell lines were successful. The HeLa cell line showed an overall increase in AuNPs per cell (180,000) when compared to the non-iodine uptake technique (150,000), although this difference is not significant when considering experimental uncertainties (quantified by the standard deviation). These results also align with Chadwick et al.'s transmission electron microscopy observations in HeLa cells: the majority of citrated coated AuNPs were identified in the cytosol and less than 10% were adsorbed onto the cell surface.(41) 74A cell lines also demonstrated similar results. Both iodine (101,000) and non-iodine (126,000) uptake experiments for citrate coated AuNPs demonstrated a non-significant difference in AuNP quantity per cell (values overlapping within standard deviations). This provides a satisfactory conclusion for the use of iodine etching as a method of differentiating cellular internalisation from generalized
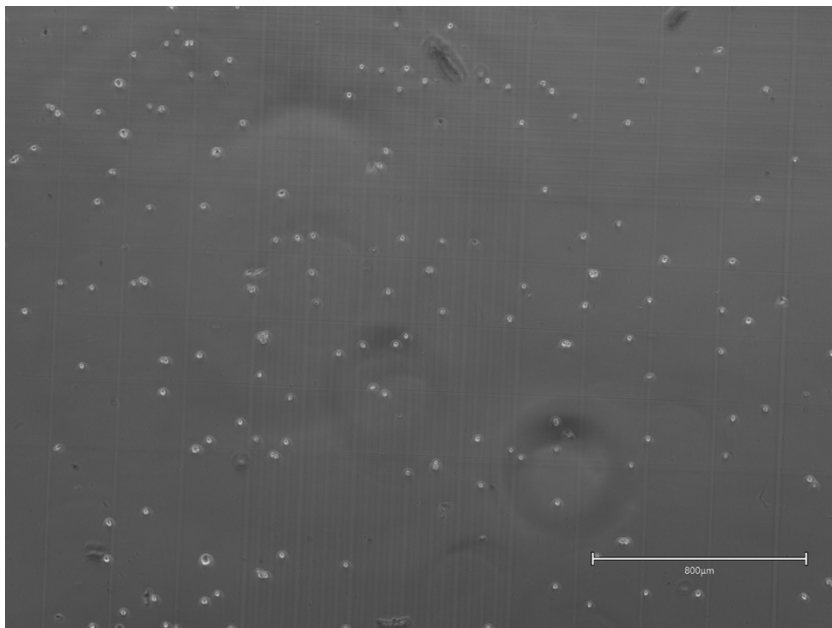
Figure 5.3: Thesis 74A cells, scale bar at 800um

cell uptake in both HeLa and 74A cell lines. There is a discrepancy between HeLa (158,000) and 74A (126,000) NP uptake. This may be attributed to differing cell lines expressing varying cell surface receptors and endocytic pathways. Microscopic evaluation of 74A cells have also revealed its cell diameter to be approximately $8\mu m$ (figure 5.3); with a decrease in surface area (compared to HeLa cells) a further potential explanation for decrease in NP uptake.

Uptake experiments performed on the 04/08/22 and 19/08/22 reviewed PEG-NP and Glc-NP uptakes with 2 differing PEG ratios encapsulating the AuNPs (PEG_5-OH:PEG_6-NH_2 of 99:1 & 98:2). Both PEG-NPs & Glc-NPs did not show any significant cellular uptake. These uptake experiments reported low Au concentrations by ICP-OES. This infers that the reported values are below ICP-OES' detection limit, therefore restricting any confirmation of NP uptake. For

PEG-NPs, this is in keeping with the literature; whereby end-hydroxyl PEGylated capping agents are known to prolong NP circulation (referred to as 'stealth' NPs).(95) Interestingly their uptake remained negligible despite the increase in amine-terminal PEGs as seen with the PEG$_5$-OH:PEG$_6$-NH$_2$ 98:2 ratioed PEG-NP uptake experiments. With respect to Glc-NP uptake results, this was not the desired outcome. This may be due to a potential number of factors related to Glc-NP synthesis. In the reported round of experiments, the concentration of residual/ excess glucosamine was likely at least an order of magnitude higher than NP-bound glucosamine, with competitive binding of free glucosamine preventing NP-GLUT1 binding and therefore limiting Glc-NP uptake. Furthermore EDC/sNHS biproducts that were not removed from the final solution during the cleansing process may cause steric interactions Glc-NP aggregation. The addition of Tween-20 and DMEM solution may promote corona formation, as well as a surfactant layer over the Glc-NPs preventing interactions with GLUT1 receptors. The positive outcome of this experiment was that non-specific NP uptake (as witnessed by citrated coated AuNPs) was not witnessed.

5.3.1 RECOMMENDATIONS TO IMPROVE UPON NP UPTAKE EXPERIMENTS

Future experiments would seek to ascertain GLUT status through Western blot analysis prior to uptake investigations. Improving the Glc-NP synthesis technique (discussed in Chapter 3) by decreasing NP loss during centrifugation and improving PEG-NP and Glc-NP concentrations would be the next reasonable step to attain more accurate and recordable concentrations within the ICP-OES' detection limits. Performing more centrifugation steps for Glc-NP is critical in reducing excess glucosamine that may be competitively inhibiting Glc-NP uptake through GLUT1s. Each centrifugation round reduces glucosamine's concentration by an approximate factor of 20. Therefore, three or more centrifugation steps may be required, together with a thorough analysis on how to reduce glucosamine well below NP concentration.

The use of a GLUT antibody on cell lines prior to cell uptake experiments with Glc-NP may serve as further confirmation of glycosylation success. WZB117 has been identified as an ideal GLUT1 inhibitor candidate, whereby it inhibits glucose in a dose-dependent manner and can be added to glucose deprived media 24-48 hours prior to uptake experiments taking place.(133)

5.4 Conclusions

Initial NP uptake & internalisation experiments were performed with a reproducible technique, as witnessed with citrate coated AuNPs. This was replicated within both HeLa and 74A cell lines, successfully incorporating the iodine etching technique into our group's ICP-OES protocol and re-affirming its validity. PEG-NP and Glc-NP uptake experiments were trialled with negative results attained. This was a positive outcome for PEG-NPs' experiments, with minimal-to-no uptake expected given that its predominantly hydroxyl end-terminal PEGs encasing the NPs. Whilst a primarily negative outcome for Glc-NPs, this confirmed that no non-specific uptake (as seen in citrate coated AuNPs) took place. The lack of Glc-NP uptake might have been secondary to excess glucosamine within the Glc-NP solution and requires further modifications to the Glc-NP synthesis technique.

CHAPTER 6: PROJECT CONCLUSIONS & LOOKING AHEAD

6.1 SUMMARY OF THESIS CHAPTERS & RESULTS

This project has laid the foundations for development of a topically applied targeted vector for OPSCCs. I have developed and began optimising a novel protocol for glycosylated AuNP synthesis through PEGylation that would improve the prospect of tumour-targeted PDT therapy. Maximising PDT efficacy involves NP cellular internalisation rather than simply being adsorbed onto the cell's membrane. As a result, an iodine etching technique in cell cultures was scrutinised and modified to distinguish NP cellular internalisation from cell surface adsorption. This was incorporated into our group's analytical approach for measuring NP cellular uptake.

Chapter 1 summarises the current treatment routes for OPSCC and experimental trials of PDT in head and neck cancer medicine. OPSCC was identified as an ideal cancer model for targeted PDT, with its trans-oral accessibility permitting topical PSA administration. AuNPs demonstrate ideal physicochemical properties for PSA delivery, although lacked tumour-targeting specificity without the appropriate surface modifications.

The systematic literature review in Chapter 2 considers NP glycosylation to enhance tumour selectivity. Examining GLUT1's structure confirmed that its central binding site is approximately 20Å from its external surface. The receptor's interactions with glucose were appreciated, whereby conjugating glucose via its 2-C or 3-C may would not hinder the carbohydrate's attachment to GLUT1. However, the NP's size prohibits its facilitated diffusion across GLUT1's central channel. Motiei and Dreifuss et al. confirmed clathrin-endocytic routes of NP-GLUT1 internalisation using endocytic pathway inhibitors, as well as glucose's preferred attachment through 2-C (when compared to other carbon attachments, including 3-C). Suitable GLUT1-deficient cell line controls re-affirmed Glc-NP's specificity with GLUT1-rich cell lines.(82,83) The literature review provided an opportunity to comprehend the limits of other similar studies reviewed. Common limitations included a lack of biological control groups, limited NP characterisation and analytical investigations failing to confirm NP internalisation. Chapter 2's

conclusions confirmed the potential for NP-GLUT1 cellular internalisation, together with a structural blueprint for glycosylation (glucose attached via its 2-C using a spacer between it and the NP of at least 20Å in length).

Chapter 3 describes the Glc-NP synthesis technique developed during this thesis. A PEGylated NP synthesis technique was favoured over Dr. Broadbent's current bilayer PAH/PSS NP approach.(24) The PEGylated strategy involved encasing AuNPs in a PEGylated capping layer (PEG-NP), with two consecutive EDC reactions attaching a glucose moiety via a further PEG linker (Glc-NP). This had a few advantages over the PAH/PSS NP model, including increased stability whilst allowing glucose attachment to occur on its the outermost surface and permitting future attachment of Rose Bengal (RB) to the outer shell. The PEGylated model may further act as a flexible, streamlined model for the attachment of other tumour-specific ligands identified in future. PEG-NP characterisation with DCS & UV-vis spectroscopy confirmed 13-14nm AuNPs capped with a PEGylated layer of SH-PEG5-OH & SH-PEG6-NH2 in viable ratios of 99:1 and 98:2% (no aggregation identified). Dissolution of PEG- NP in Tween-20 solution allowed for Glc-NP synthesis and cleansing through centrifugation, without adherence to the sidewalls of centrifugation tubes. DCS results confirmed an increase in shell thickness from citrate coated AuNPs to PEG-NPs to Glc-NPs, highly suggestive that the addition of a PEG capping layer and subsequently glycosylation was successful.

An NP cellular internalisation quantification protocol was optimised in Chapter 4, based on Cho et al's methodology. They concluded that I_2/KI solution would successfully etch away AuNPs on cellular surface, minimizing cell toxicity when incubation the cells with a 0.34mM I_2/KI solution for 5 minutes.(122) The chapter reviewed I_2's etching capacity at low millimolar concentrations, establishing through UV-vis that 0.085mM I_2 was the lowest concentration to etch away 1nM AuNP to near completion. MTT and trypan blue assays examined iodine's cytotoxicity, concluding that the relative cell membrane stability for HeLa, 74A and Um-SCC 6 cell lines was above 80% with a 0.085mM I_2/KI solution.

Results from the initial quantification of NP cell uptake are the focus of Chapter 5. Citrate coated AuNP uptake in HeLa was 3.75 times higher than our group's previous results, likely due to a difference in the thesis' larger HeLa cell size (3.8 times larger). The iodine etching protocol yielded successful results in both HeLa and 74A cell lines. No significant differences were noted in the final citrated coated AuNP uptake values of both iodine and non-iodine

uptake protocols (values falling within standard deviation limits). This re-affirms Dr. Chadwick's previous data, whereby electron microscopy confirmed that less than 10% of citrate coated AuNPs were found on the surface of HeLa cells.(41) No appreciable uptake was detected for PEG-NPs and Glc-NPs. This was a positive outcome for PEG-NPs, providing a strong indication that the capping layer prevents uptake as described in the literature (a PEGylation layer increase circulation time rather than enhancing cell uptake).(95) Whilst the lack of Glc-NP uptake was a negative result, this may be due to various factors. Excess free glucosamine and EDC/sNHS biproducts not removed through centrifugation, as well as interactions of Glc-NPs with Tween-20 and DMEM may have prevented Glc-NP's interactions with GLUT1. However, the experiment re-affirms that there is no unspecific uptake witnessed with Glc-NP (unlike citrate coated AuNPs), hinting towards potential glycosylation.

6.2 MOVING FORWARDS: MODIFICATIONS

6.2.1 GLC-NP SYNTHESIS

It is still evident that NP loss is occurring (albeit less with Tween-20) during centrifugation steps. This is evident when centrifugating PEG-NPs & Glc-NPs, as seen on UV-vis spectroscopy. Higher Tween concentrations used by our group in later Glc-NP synthesis attempts have decreased NP loss through centrifugation and may be a solution. Utilising a Tween surfactant with more alkyl chains present (such as Tween-80) may be a further option to prevent NP loss through centrifugation. Dialysis is an alternative purifying process to centrifugation. This would hypothetically separate Glc-NPs unwanted reaction products, including excess non-bound glucosamine that may be negatively affecting uptake experiments. Furthermore, the use of high-performance liquid chromatography may achieve better separation of products attained during the EDC reactions, removing unwanted reactants that may cause cross-linking (such as Glc-PEG$_{11}$-EDC). This would improve the glycosylation rate of PEG-NPs' terminals, by reacting PEG-NPs directly with Glc-PEG$_{11}$-EDC. Using PEG chains with a minimum molecular weight of 2000 would be a different approach to preventing Glc-NP aggregation. When compared to the use of short PEG chains, this has been shown in the literature to reduce NP aggregation (as used in this synthesis technique). (102)

Taking the synthesis technique to the next stage, RB attachment will need to be considered, functionalizing the NP for PDT. Reacting PEG-NPs with 50:50% concentration mix of Glc-PEG$_{11}$-EDC (separated by HPLC) and RB- would be an ideal way of achieving a tumour-selective, PDT-functioning NP.

6.2.2 CELL UPTAKE/ INTERNALISATION EXPERIMENTS

Uptake trials may be improved by addressing the synthesis restrictions noted in subsection 6.2.1, particularly by removing the extra non-bound glucosamine discovered in the final Glc-NP solution. Western blot analysis on cell line pellets taken per session of uptake experiments would allow for characterization and quantification of GLUT present per cell line. This would support the validity of Glc-NP uptake conclusions when comparing uptake in GLUT1-rich and GLUT1- deficient cell lines. An alternative to GLUT1- deficient cell lines would be the consideration of a GLUT1 inhibitor, such as WZB117.

6.2.3 INCORPORATING GLC-NPS WITH PHOTODYNAMIC THERAPY

As a general overview, the inclusion of Glc-NPs in PDT would involve a two-point sequential plan. Firstly, the attachment of RB to Glc-NP would allow for testing of singlet oxygen production with the use of a probe. Dr. Entradas has used 9,10-Anthracenediyl-bis(methylene)dimalonic acid (ABDA) as a singlet oxygen sensor when investigating the 'cell killing efficacy' of the PAH/PSS bilayered AuNP with RB.(32) This experiment may be replicated with modified Glc-NPs, drawing comparisons between the two NPs' efficacies. Thereafter, a 3-dimensional cellular model may be considered for assessing PDT penetration and efficacy at different tumour depths. As discussed in the literature review, tumor penetration is a well-known drawback of PDT as outlined in Chapter 1. Such a model may provide more precise information regarding depth of NP penetration and tumour dimensions that may be considered suitable for PDT.

6.3 FINAL CONCLUSIONS

This thesis recounts a detailed protocol development for two key processes:

1. Optimisation of an iodine etching methodology to accurately quantify NP cellular internalisation
2. Production of PEGylated & glycosylated AuNPs that have the functional translational potential for diagnostic and therapeutic modalities

This work has established a Glc-NP protocol with NP characterization results highly suggestive of successful glycosylation. The incorporation of photosensitiser RB into our Glc-NP would create a selective third generation PSA and a viable topical therapeutic option for OPSCC through PDT. This could potentially alter current OPSCC treatment guidelines and improve patients' quality of life through a reduction in systemic chemoradiotherapy, whilst adopting a more cancer-targeted, NP based PDT approach.

REFERENCES

1. Taib BG, Oakley J, Dailey Y, Hodge I, Wright P, du Plessis R, et al. Socioeconomic deprivation and the burden of head and neck cancer—Regional variations of incidence and mortality in Merseyside and Cheshire, North West, England. Clin Otolaryngol. 2018;43(3):846–53.

2. Huang SH, Hansen A, Rathod S, O'Sullivan B. Primary surgery versus (chemo)radiotherapy in oropharyngeal cancer: The radiation oncologist's and medical oncologist's perspectives. Vol. 23, Curr Opin Otolaryngol Head Neck Surg. 2015; 23(2):139-47.

3. Kelly JR, Park HS, An Y, Contessa JN, Yarbrough WG, Burtness BA, et al. Comparison of survival outcomes among human papillomavirus–negative cT1-2 N1-2b patients with oropharyngeal squamous cell cancer treated with upfront surgery vs definitive chemoradiation therapy: An observational study. JAMA Oncol. 2017;3(8):1107–11.

4. Hamilton D, Khan MK, O'Hara J, Paleri V. The changing landscape of oropharyngeal cancer management. Vol. 131, J Laryngol Otol. 2017; 131(1):3-7.

5. Wilkie MD, Upile NS, Lau AS, Williams SP, Sheard J, Helliwell TR, et al. Transoral laser microsurgery for oropharyngeal squamous cell carcinoma: A paradigm shift in therapeutic approach. Head Neck. 2016;38(8):1263–70.

6. National Cancer Registration and Analysis Service. Head and Neck Cancers: Research Statistics . Cancer Registration Statistics. 2021.

7. Evans M, Beasley M. Target delineation for postoperative treatment of head and neck cancer. Oral Oncol. 2018;86:288–95.

8. Hay A, Nixon IJ. Recent advances in the understanding and management of oropharyngeal cancer. F1000 Res. 2018;7:F1000 Faculty Rev-1362.

9. Department of Veterans Affairs Laryngeal Cancer Study Group; Wolf GT, Fisher SG, Hong WK, Hillman R, Spaulding M, et al. Induction chemotherapy plus radiation compared with surgery plus radiation in patients with advanced laryngeal cancer. N Engl J Med. 1991;324(24):1685-90.

10. Calais G, Alfonsi M, Bardet E, Sire C, Germain T, Bergerot P, et al. Randomized trial of radiation therapy versus concomitant chemotherapy and radiation therapy for advanced-stage oropharynx carcinoma. J Natl Cancer Inst. 1999;91(24):2081-6.

11. Høxbroe Michaelsen S, Grønhøj C, Høxbroe Michaelsen J, Friborg J, von Buchwald C. Quality of life in survivors of oropharyngeal cancer: A systematic review and meta-analysis of 1366 patients. Eur J Cancer. 2017 Jun;78:91-102.

12. Golusiński W, Golusińska-Kardach E. Current role of surgery in the management of oropharyngeal cancer. Front Oncol. 2019 May 24;9:388.

13. Denis F, Garaud P, Bardet E, Alfonsi M, Sire C, et al. Late toxicity results of the GORTEC 94-01 randomized trial comparing radiotherapy with concomitant radiochemotherapy for advanced-stage oropharynx carcinoma: comparison of LENT/SOMA, RTOG/EORTC, and NCI-CTC scoring systems. Int J Radiat Oncol Biol Phys. 2003;55(1):93-8.

14. JM, Rapley R. Medical Biomethods Handbook. Humana Press; 2005

15. Lambert A, Nees L, Nuyts S, Clement P, Meulemans J, Delaere P, et al. Photodynamic Therapy as an Alternative Therapeutic Tool in Functionally Inoperable Oral and Oropharyngeal Carcinoma: A Single Tertiary Center Retrospective Cohort Analysis. Front Oncol. 2021;11.

16. Hou YJ, Yang XX, Liu RQ, Zhao D, Guo CX, Zhu AC, et al. Pathological mechanism of photodynamic therapy and photothermal therapy based on nanoparticles. Int J Nanomedicine. 2020;15:6827–38.

17. Hu JJ, Lei Q, Zhang XZ. Recent advances in photonanomedicines for enhanced cancer photodynamic therapy. Prog Mater Sci. 2020;114:100685

18. Donohoe C, Senge MO, Arnaut LG, Gomes-da-Silva LC. Cell death in photodynamic therapy: From oxidative stress to anti-tumor immunity. Biochim Biophys Acta Rev Cancer. 2019;1872(2):188308 .

19. Bai X, Wang Y, Song Z, Feng Y, Chen Y, Zhang D, et al. The basic properties of gold nanoparticles and their applications in tumor diagnosis and treatment. Int J Mol Sci. 2020;21(7):2480 .

20. Karakullukcu B, Stoker SD, Wildeman APE, Copper MP, Wildeman MA, Tan IB. A matched cohort comparison of mTHPC-mediated photodynamic therapy and trans-oral surgery of early-stage oral cavity squamous cell cancer. Eur Arch Otorhinolaryngol. 2013;270(3):1093-7.

21. Schweitzer VG, Somers ML. PHOTOFRIN-mediated photodynamic therapy for treatment of early stage (Tis-T2N0M0) SqCCa of oral cavity and oropharynx. Lasers Surg Med. 2010;42(1):1–8.

22. Hopper C, Kübler A, Lewis H, Tan IB, Putnam G, Patrice T, et al. mTHPC-mediated photodynamic therapy for early oral squamous cell carcinoma. Int J Cancer. 2004;111(1):138–46.

23. Kwiatkowski S, Knap B, Przystupski D, Saczko J, Kędzierska E, Knap-Czop K, et al. Photodynamic therapy – mechanisms, photosensitizers and combinations. Biomed Pharmacother. 2018;106:1098-1107.

24. Broadbent M. Nanoparticle use in Photodynamic Therapy. University of Liverpool 2022.

25. García Calavia P, Bruce G, Pérez-García L, Russell DA. Photosensitiser-gold nanoparticle conjugates for photodynamic therapy of cancer. Photochem Photobiol Sci. 2018;17(11):1534-1552 .

26. Boisselier E, Astruc D. Gold nanoparticles in nanomedicine: preparations, imaging, diagnostics, therapies and toxicity. Chem Soc Rev. 2009;38(6):1759–82.

27. Alkilany AM, Lohse SE, Murphy CJ. The gold standard: Gold nanoparticle libraries to understand the nano-bio interface. Acc Chem Res. 2013;46(3):650–61.

28. Yeh YC, Creran B, Rotello VM. Gold nanoparticles: Preparation, properties, and applications in bionanotechnology. Nanoscale. 2012;4(6):1871-80.

29. Garcia MA, de La Venta J, Crespo P, Llopis J, Penadés S, Fernández A, et al. Surface plasmon resonance of capped Au nanoparticles. Phys Rev B Condens Matter Mater Phys. 2005;72(24).

30. Wriedt T. Mie theory: a review. The Mie theory: Basics and applications. 2012:53-71.

31. Amendola V, Pilot R, Frasconi M, Maragò OM, Iatì MA. Surface plasmon resonance in gold nanoparticles: A review. Vol. 29, Journal of Physics Condensed Matter. J Phys Condens Matter. 2017;29(20):203002.

32. Entradas T, Waldron S, Volk M. The detection sensitivity of commonly used singlet oxygen probes in aqueous environments. J Photochem Photobiol B. 2020;204.

33. Dong J, Carpinone PL, Pyrgiotakis G, Demokritou P, Moudgil BM. Synthesis of precision gold nanoparticles using Turkevich method. Kona. 2020 Jan 10;37:224-232. .

34. Yeh YC, Creran B, Rotello VM. Gold nanoparticles: Preparation, properties, and applications in bionanotechnology. Nanoscale. 2012 Mar 21;4(6):1871-80.

35. Singh P, Pandit S, Mokkapati VRSS, Garg A, Ravikumar V, et al. Gold nanoparticles in diagnostics and therapeutics for human cancer. Int J Mol Sci. 2018 Jul 6;19(7):1979 .

36. Lima T, Bernfur K, Vilanova M, Cedervall T. Understanding the Lipid and Protein Corona Formation on Different Sized Polymeric Nanoparticles. Sci Rep. 2020 Dec 1;10(1).

37. Donahue ND, Acar H, Wilhelm S. Concepts of nanoparticle cellular uptake, intracellular trafficking, and kinetics in nanomedicine. Sci Rep. 2020 Jan 24;10(1):1129.

38. Rennick JJ, Johnston APR, Parton RG. Key principles and methods for studying the endocytosis of biological and nanoparticle therapeutics. Nat Nanotechnol. 2021 Mar;16(3):266-276.

39. Wang X, Wang X, Bai X, Yan L, Liu T, Wang M, et al. Nanoparticle Ligand Exchange and Its Effects at the Nanoparticle-Cell Membrane Interface. Nano Lett. 2019;19(1):8–18.

40. Zhang S, Gao H, Bao G. Physical Principles of Nanoparticle Cellular Endocytosis. ACS Nano. 2015 Sep 22;9(9):8655-71.

41. Chadwick S. Photodynamic and Photothermal Human Cancer Cell Killing Using Gold Nanoparticles. 2015.

42. Albanese A, Chan WCW. Effect of gold nanoparticle aggregation on cell uptake and toxicity. ACS Nano. 2011 Jul 26;5(7):5478-89.

43. Bahamonde J, Brenseke B, Chan MY, Kent RD, Vikesland PJ, et al. Gold Nanoparticle Toxicity in Mice and Rats: Species Differences. Toxicol Pathol. 2018;46(4):431–43.

44. Fratoddi I, Benassi L, Botti E, Vaschieri C, Venditti I, Bessar H, et al. Effects of topical methotrexate loaded gold nanoparticle in cutaneous inflammatory mouse model. Nanomedicine. 2019;17:276–86.

45. Vanerio N, Stijnen M, de Mol BAJM, Kock LM. Biomedical Applications of Photo- and Sono-Activated Rose Bengal: A Review. Photobiomodul Photomed Laser Surg. 2019;37(7):383–94.

46. Fadel M, Kassab K. Evaluation of the photostability and photodynamic efficacy of Rose Bengal loaded in multivesicular liposomes. Trop. J. Pharm. Res. 2011;10(3):289–97.

47. Serrano MP, Rafti M, Thomas AH, Borsarelli CD. Photosensitizing properties of hollow microcapsules built by multilayer self-assembly of poly(allylamine hydrochloride) modified with rose Bengal. RSC Adv. 2019;9(33):19226–35.

48. Tilekar K, Upadhyay N, Iancu C v., Pokrovsky V, Choe J yong, et al. Power of two: combination of therapeutic approaches involving glucose transporter (GLUT) inhibitors to combat cancer. Biochim Biophys Acta Rev Cancer. 2020;1874(2):188457.

49. Jennings ML. Carriers, exchangers, and cotransporters in the first 100 years of the Journal of General Physiology. J Gen Physiol. 2018;150(8):1063-1080 .

50. Aydogan B, Li J, Rajh T, Chaudhary A, Chmura SJ, Pelizzari C, et al. AuNP-DG: Deoxyglucose-labeled gold nanoparticles as X-ray computed tomography contrast agents for cancer imaging. Mol Imaging Biol. 2010;12(5):463–7.

51.   Yao C, Zhang L, Wang J, He Y, Xin J, Wang S, et al. Gold Nanoparticle Mediated
       Phototherapy for Cancer. J. Nanomater. 2016.

52.   Yang H, Zhong JT, Zhou SH, Han HM. Roles of GLUT-1 and HK-II expression in the biological
       behavior of head and neck cancer. Oncotarget. 2019 Apr 30;10(32):3066-3083

53.   Li S jiao, Guo W, Ren G xin, Huang G, Chen T, et al. Expression of Glut-1 in primary and
       recurrent head and neck squamous cell carcinomas and compared with 2-[18F]fluoro-2-
       deoxy-D-glucose accumulation in positron emission tomography. Br J Oral Maxillofac Surg.
       2008;46(3):180-186.

54.   Reisser C, Eichhorn K, Herold-Mende C, Born AI, Bannasch P. Expression of facilitative
       glucose transport proteins during development of squamous cell carcinomas of the head
       and neck. Int J Cancer. 1999;80(2):194-8 .

55.   Azad N, Kumari Maurya M, Kar M, Goel MM, Singh AK, Sagar M, et al. Expression of GLUT-1
       in oral squamous cell carcinoma in tobacco and non-tobacco users. J Oral Biol Craniofac
       Res. 2016;6(1):25–31.

56.   Custódio TF, Paulsen PA, Frain KM, Pedersen BP. Structural comparison of GLUT1 to GLUT3
       reveal transport regulation mechanism in sugar porter family. Life Sci Alliance.
       2021;4(4):e202000858 .

57.   Drew D, North RA, Nagarathinam K, Tanabe M. Structures and General Transport
       Mechanisms by the Major Facilitator Superfamily (MFS). Chem Rev. 2021;121(9):5289-
       5335.

58.   Wright EM. Glucose transport families SLC5 and SLC50. 2013;34(2-3):183-96.

59.   Kasahara T, Maeda M, Boles E, Kasahara M. Identification of a key residue determining
       substrate affinity in the human glucose transporter GLUT1. Biochim Biophys Acta
       Biomembr. 2009;1788(5):1051–5.

60.   Deng D, Xu C, Sun P, Wu J, Yan C, Hu M, et al. Crystal structure of the human glucose
       transporter GLUT1. Nature. 2014;510(7503):121–5.

61.   Raja M, Kinne RKH. Mechanistic Insights into Protein Stability and Self-aggregation in
       GLUT1 Genetic Variants Causing GLUT1-Deficiency Syndrome. J Membr Biol.
       2020;253(2):87-99 .

62.   Fu X, Zhang G, Liu R, Wei J, Zhang-Negrerie D, Jian X, et al. Mechanistic Study of Human
       Glucose Transport Mediated by GLUT1. J Chem Inf Model. 2016;56(3):517–26.

63.   Eyster CA, Higginson JD, Huebner R, Porat-Shliom N, Weigert R, Wu WW, et al. Discovery of
       new cargo proteins that enter cells through clathrin-independent endocytosis. Traffic.
       2009;10(5):590–9.

64.   Yuan T, Hong S, Yao Y, Liao K. Glut-4 is translocated to both caveolae and non-caveolar lipid rafts, but is partially internalized through caveolae in insulin-stimulated adipocytes. Cell Res. 2007;17(9):772–82.

65.   Foley K, Boguslavsky S, Klip A. Endocytosis, recycling, and regulated exocytosis of glucose transporter 4. Biochemistry. 2011;50(15):3048–61.

66.   Dannhauser PN, Camus SM, Sakamoto K, Sadacca LA, Torres JA, Camus MD, et al. CHC22 and CHC17 clathrins have distinct biochemical properties and display differential regulation and function. J Biol Chem. 2017;292(51):20834-20844.

67.   Kong T, Zeng J, Wang X, Yang X, Yang J, McQuarrie S, et al. Enhancement of radiation cytotoxicity in breast-cancer cells by localized attachment of gold nanoparticles. Small. 2008;4(9):1537–43.

68.   Zhang X, Xing JZ, Chen J, Ko L, Amanie J, Gulavita S, et al. Enhanced radiation sensitivity in prostate cancer by gold-nanoparticles. Clin Invest Med. 2008;31(3):E160-7.

69.   Geng F, Song K, Xing JZ, Yuan C, Yan S, Yang Q, et al. Thio-glucose bound gold nanoparticles enhance radio-cytotoxic targeting of ovarian cancer. Nanotechnology. 2011;22(28).

70.   Sur I, Cam D, Kahraman M, Baysal A, Culha M. Interaction of multi-functional silver nanoparticles with living cells. Nanotechnology. 2010;21(17).

71.   Xiong F, Zhu ZY, Xiong C, Hua XQ, Shan XH, Zhang Y, et al. Preparation, characterization of 2-deoxy-D-glucose functionalized dimercaptosuccinic acid-coated maghemite nanoparticles for targeting tumor cells. Pharm Res. 2012;29(4):1087–97.

72.   Wang J, Yin C, Tang G, Lin X, Wu Q. Glucose-functionalized multidrug-conjugating nanoparticles based on amphiphilic terpolymer with enhanced anti-tumorous cell cytotoxicity. Int J Pharm. 2013;441(1–2):291–8.

73.   Jiang X, Xin H, Gu J, Du F, Feng C, Xie Y, et al. Enhanced antitumor efficacy by d - glucosamine-functionalized and paclitaxel-loaded poly(ethylene glycol)-co- poly(trimethylene carbonate) polymer nanoparticles. J Pharm Sci. 2014;103(5):1487–96.

74.   Hu C, Niestroj M, Yuan D, Chang S, Chen J. Treating cancer stem cells and cancer metastasis using glucose-coated gold nanoparticles. Int J Nanomedicine. 2015;10:2065–77.

75.   Venturelli L, Nappini S, Bulfoni M, Gianfranceschi G, Dal Zilio S, et al. Glucose is a key driver for GLUT1-mediated nanoparticles internalization in breast cancer cells. Sci Rep. 2016;6.

76.   Shan XH, Wang P, Xiong F, Gu N, Hu H, et al. MRI of High-Glucose Metabolism Tumors: a Study in Cells and Mice with 2-DG-Modified Superparamagnetic Iron Oxide Nanoparticles. Mol Imaging Biol. 2016;18(1):24–33.

77.   Panzarini E, Mariano S, Vergallo C, Carata E, Fimia GM, et al. Glucose capped silver nanoparticles induce cell cycle arrest in HeLa cells. Toxicology in Vitro. 2017;41:64–74.

78.   Park JH, Cho HJ, Kim DD. Poly((D,L)lactic-glycolic)acid-star glucose nanoparticles for glucose transporter and hypoglycemia-mediated tumor targeting. Int J Nanomedicine. 2017;12:7453–67.

79.   Aşik E, Aslan TN, Volkan M, Güray NT. 2-Amino-2-deoxy-glucose conjugated cobalt ferrite magnetic nanoparticle (2DG-MNP) as a targeting agent for breast cancer cells. Environ Toxicol Pharmacol. 2016;41:272–8.

80.   Singh S. Glucose decorated gold nanoclusters: A membrane potential independent fluorescence probe for rapid identification of cancer cells expressing Glut receptors. Colloids Surf B Biointerfaces. 2017;155:25–34.

81.   Barbaro D, di Bari L, Gandin V, Evangelisti C, Vitulli G, et al. Glucose-coated superparamagnetic iron oxide nanoparticles prepared by metal vapour synthesis are electively internalized in a pancreatic adenocarcinoma cell line expressing GLUT1 transporter. PLoS One. 2015;10(4).

82.   Motiei M, Dreifuss T, Betzer O, Panet H, Popovtzer A et al. Differentiating between Cancer and Inflammation: A Metabolic-Based Method for Functional Computed Tomography Imaging. ACS Nano. 2016;10(3):3469–77.

83.   Dreifuss T, Ben-Gal TS, Shamalov K, Weiss A, Jacob A et al. Uptake mechanism of metabolic-Targeted gold nanoparticles. Nanomedicine. 2018;13(13):1535–49.

84.   Pia A, Kröger P, Komil MI, Hamelmann NM, Juan A et al. Glucose Single-Chain Polymer Nanoparticles for Cellular Targeting. 2019 Jan 15;8(1):95-101.

85.   Shamsi M, Zolbanin JM, Mahmoudian B, Zolbanin NM, Maleki LA, Jafarabadi MA, et al. A study on drug delivery tracing with radiolabeled mesoporous hydroxyapatite nanoparticles conjugated with 2DG/DOX for breast tumor cells. Nucl Med Rev Cent East Eur. 2018;21(1):32-36.

86.   Cheng TM, Chu HL, Lee YC, Wang DY, Chang CC, et al. Quantitative Analysis of Glucose Metabolic Cleavage in Glucose Transporters Overexpressed Cancer Cells by Target-Specific Fluorescent Gold Nanoclusters. Anal Chem. 2018;90(6):3974–80.

87.   Sun IC, Ahn CH, Kim K, Emelianov S. Photoacoustic imaging of cancer cells with glycol-chitosan-coated gold nanoparticles as contrast agents. J Biomed Opt. 2019;24(12):1.

88.   Yi Y, Kim HJ, Zheng M, Mi P, Naito M et al. Glucose-linked sub-50-nm unimer polyion complex-assembled gold nanoparticles for targeted siRNA delivery to glucose transporter 1-overexpressing breast cancer stem-like cells. J Control Release. 2019;295:268–77.

89.   Li Y, Hong W, Zhang H, Zhang TT, Chen Z et al. Photothermally triggered cytosolic drug delivery of glucose functionalized polydopamine nanoparticles in response to tumor microenvironment for the GLUT1-targeting chemo-phototherapy. J Control Release. 2020;317:232–45.

90.   Wang H, Wang X, Xie C, Zhang M, Ruan H et al. Nanodisk-based glioma-targeted drug delivery enabled by a stable glycopeptide. J Control Release. 2018;284:26–38.

91.   Aslan TN, Aşık E, Güray NT, Volkan M. The potential application of gold-apoferritin nanocages conjugated with 2-amino-2-deoxy-glucose for imaging of breast cancer cells. J Biol Inorg Chem. 2020 Dec 1;25(8):1139–52.

92.   Abuchowski A, McCoy JR, Palczuk NC, van Es T, Davis FF. Effect of covalent attachment of polyethylene glycol on immunogenicity and circulating life of bovine liver catalase. J Biol Inorg Chem. 1977;252(11):3582–6.

93.   Suk JS, Xu Q, Kim N, Hanes J, Ensign LM. PEGylation as a strategy for improving nanoparticle-based drug and gene delivery. Adv Drug Deliv Rev. 2016;99(Pt A):28-51.

94.   Manson J, Kumar D, Meenan BJ, Dixon D. Polyethylene glycol functionalized gold nanoparticles: The influence of capping density on stability in various media. Gold Bull. 2011;44(2):99–105.

95.   Chithrani DB. Polyethylene Glycol Density and Length Affects Nanoparticle Uptake by Cancer Cells. J Nanomed Res. 2014;1(1).

96.   Harrison E, Nicol JR, Macias-Montero M, Burke GA, Coulter JA, et al. A comparison of gold nanoparticle surface co-functionalization approaches using Polyethylene Glycol (PEG) and the effect on stability, non-specific protein adsorption and internalization. Mater Sci Eng C Mater Biol Appl. 2016 May;62:710-8.

97.   Harrison E, Coulter JA, Dixon D. Gold nanoparticle surface functionalization: Mixed monolayer versus hetero bifunctional peg linker. Nanomedicine (Lond). 2016 Apr;11(7):851-65.

98.   Matsumura Y, Maeda2 H. A New Concept for Macromolecular Therapeutics in Cancer Chemotherapy: Mechanism of Tumoritropic Accumulation of Proteins and the Antitumor Agent Smancs1. Cancer Res. 1986 Dec;46(12 Pt 1):6387-92.

99.   Nicoara R, Ilies M, Uifalean A, Iuga CA, Loghin F. Quantification of the PEGylated gold nanoparticles protein corona. Influence on nanoparticle size and surface chemistry. Appl. Sci. 2019;9(22).

100. Lipka J, Semmler-Behnke M, Sperling RA, Wenk A, Takenaka S et al. Biodistribution of PEG-modified gold nanoparticles following intratracheal instillation and intravenous injection. Biomaterials. 2010;31(25):6574–81.

101. Pannuzzo M, Esposito S, Wu LP, Key J, Aryal S et al. Overcoming Nanoparticle-mediated complement activation by surface PEG pairing. Nano Lett. 2020;20(6):4312–21.

102. Liu T, Thierry B. A solution to the PEG dilemma: Efficient bioconjugation of large gold nanoparticles for biodiagnostic applications using mixed layers. Langmuir. 2012;28(44):15634–42.

103. Thermo Scientific Inc. NHS and Sulfo-NHS Instructions [Internet]. Thermo Scientific 2011 [cited 2023]. Available from; https://tools.thermofisher.com/content/sfs/manuals/MAN0011309_NHS_SulfoNHS_UG.pdf.

104. G-Biosciences. Protein Cross-linkers handbook and selection guide [Internet]. Geno-Technology Inc. [cited 2023]. Available from; http://genotech.com/bulletins/xlinker-handbook.pdf

105. Thermo Scientific Inc. Easy Molecular Bonding Crosslinking Technology. Thermo Scientific Handbook technology 2011 [cited 2023]. Available from; https://tools.thermofisher.com/content/sfs/brochures/1602163-Crosslinking-Reagents-Handbook.pdf

106. Fan J, Cheng Y, Sun M. Functionalized Gold Nanoparticles: Synthesis, Properties and Biomedical Applications. Chem Rec. 2020 Dec;20(12):1474-1504.

107. Krpetić Ž, Davidson AM, Volk M, Lévy R, Brust M, Cooper DL. High-resolution sizing of monolayer-protected gold clusters by differential centrifugal sedimentation. ACS Nano. 2013 2;7(10):8881–90.

108. McNeil SE, editor. Characterization of nanoparticles intended for drug delivery. New York, NY: Humana press; 2011.

109. Haiss W, Thanh NTK, Aveyard J, Fernig DG. Determination of size and concentration of gold nanoparticles from UV-Vis spectra. Anal Chem. 2007;79(11):4215–21.

110. Duchesne L, Gentili D, Comes-Franchini M, Fernig DG. Robust ligand shells for biological applications of gold nanoparticles. Langmuir. 2008;24(23):13572–80.

111. Shen CC, Tseng WL, Hsieh MM. Selective extraction of thiol-containing peptides in seawater using Tween 20-capped gold nanoparticles followed by capillary electrophoresis with laser-induced fluorescence. J Chromatogr A. 2012;1220:162–8.

112.   Zhao Y, Wang Z, Zhang W, Jiang X. Adsorbed Tween 80 is unique in its ability to improve the stability of gold nanoparticles in solutions of biomolecules. Nanoscale. 2010;2(10):2114–9.

113.   Lin CY, Yu CJ, Lin YH, Tseng WL. Colorimetric sensing of silver(I) and mercury(II) ions based on an assembly of tween 20-stabilized gold nanoparticles. Anal Chem. 2010;82(16):6830–7.

114.   Helgason T, Awad TS, Kristbergsson K, McClements DJ, Weiss J. Effect of surfactant surface coverage on formation of solid lipid nanoparticles (SLN). J Colloid Interface Sci. 2009;334(1):75–81.

115.   Farfán-Castro S, García-Soto MJ, Comas-García M, Arévalo-Villalobos JI, Palestino G et al. Synthesis and immunogenicity assessment of a gold nanoparticle conjugate for the delivery of a peptide from SARS-CoV-2. Nanomedicine. 2021;34.

116.   Voigt N, Henrich-Noack P, Kockentiedt S, Hintz W, Tomas J et al. Surfactants, not size or zeta-potential influence blood-brain barrier passage of polymeric nanoparticles. Eur J Pharm Biopharm. 2014 May;87(1):19-29.

117.   Green TA. Gold etching for microfabrication. Gold Bulletin. 2014; 47(3):205-16.

118.   Zamora JL, York N. Chemical and Microbiologic Characteristics Povidone-Iodine Solutions. Am J Surg. 1986;151(3):400-6.

119.   Davis A, Tran T, Young DR. Solution chemistry of iodide leaching of gold. Vol. 32, Hydrometallurgy. 1993;32(2):143-59

120.   Stevic P. Gold Etchant Standard Operating Procedure [Internet]. Sigma Aldrich 2018 [cited 2022]. Available from: https://www.sigmaaldrich.com/catalog/product/aldrich/651818?lang=en&region=NL

121.   Zhong Q, Chen Y, Qin X, Wang Y, Yuan C, Xu Y. Colorimetric enzymatic determination of glucose based on etching of gold nanorods by iodine and using carbon quantum dots as peroxidase mimics. Microchimica Acta. 2019;186(3).

122.   Cho EC, Xie J, Wurm PA, Xia Y. Understanding the role of surface charges in cellular adsorption versus internalization by selectively removing gold nanoparticles on the cell surface with a I 2/KI etchant. Nano Lett. 2009;9(3):1080–4.

123.   Rodríguez F, Castillo-Ortega MM, Encinas JC, Sánchez-Corrales VM, Pérez-Tello M, Munive GT. Adsorption of a gold-iodide complex (AuI2-) onto cellulose acetate-polyaniline membranes: Equilibrium experiments. J Appl Polym Sci. 2009;113(4):2670–4.

124.   Kireev S v., Shnyrev SL. Study of molecular iodine, iodate ions, iodide ions, and triiodide ions solutions absorption in the UV and visible light spectral bands. Laser Phys. 2015;25(7).

125.   Liang CJ, Li JY. Recovery of gold in iodine-iodide system–a review. Sep Sci Technol. 2019;54(6):1055-66.

126.   Riss T. Is your MTT assay really the best choice. Promega. 2017.

127.   Stepanenko AA, Dmitrenko V. Pitfalls of the MTT assay: Direct and off-target effects of inhibitors can result in over/underestimation of cell viability. Gene. 2015;574(2):193–203.

128.   van Meerloo J, Kaspers GJL, Cloos J. Cell Sensitivity Assays: The MTT Assay. Cancer cell culture: methods and protocols. 2011:237-45.

129.   Iti S. ICP-OES: An Advance Tool in Biological Research. Open J Environ Biol. 2020 Oct;5(1):027-33.

130.   Rodríguez-Enríquez S, Marín-Hernández A, Gallardo-Pérez JC, Moreno-Sánchez R. Kinetics of transport and phosphorylation of glucose in cancer cells. J Cell Physiol. 2009;221(3):552–9.

131.   Silén J, Högel H, Kivinen K, Silvoniemi A, Forsback S, Löyttyniemi E, et al. Uptake of [18f]Ef5 As a Tracer for Hypoxic And Aggressive Phenotype in Experimental Head and Neck Squamous Cell carcinoma. Transl Oncol. 2014;7(3):323–30.

132.   Khetan J, Shahinuzzaman M, Barua S, Barua D. Quantitative Analysis of the Correlation between Cell Size and Cellular Uptake of Particles. Biophys J. 2019;116(2):347–59.

133.   Pliszka M, Szablewski L. Glucose Transporters as a Target for Anticancer Therapy. Cancers (Basel). 2021 Aug 20;13(16):4184.

A<small>PPENDIX</small> 1

The appendix consists of a summary of each research group's publications included in the literature review (chapter 2). For each study, it details cell lines & carbohydrate analogue used for NP conjugation as well as investigations, measured outcomes, study strength & weakness and conclusions reached from their research.

Kang et al. Research Group [67-69]	2008 - 2011
Cell lines	MCF-7 & MCF-10A Cell line (Breast Carcinoma)
Carbohydrate Analogue used	1-Thio-B-Glucose & Cysteamine Moieties attached to AuNPs (10.8nm diameter)
NP Absorption Investigations	Inductively Coupled Mass Spectroscopy (ICP-MS) following cell lysis (trypsin) Transmission Electron Microscopy (TEM) for qualitative analysis of uptake
Measured Outcomes	
• Cell Absorption	Threefold increase in Cysteamine coated NP absorption compared to Glc-NPs, due to its positively charged surface. TEM displays intracellular Glc-NPs, whilst cysteamine coated NPs are at the periphery of cells.
Study Strengths	Acknowledges that ICP-MS does not distinguish between adsorption vs. internalization. Cell irradiation suggests different cellular localisations of NPs types, with Glc-NPs exhibiting lower cell viability. Comparators utilised including non-cancerous cell line & non-functionalised NPs.
Study Limitations	No further investigations performed to differentiate cell uptake vs. adsorption. Carbon position of glucose attachment site not considered as a limiting factor in the Glc-NPs absorption.
Conclusions	Modified surface properties have produced enhanced adsorption vs. internalization effects
Sur et al. [70]	2010
Cell lines	A549 (non-small cell carcinoma) & L929 (mouse fibroblast cells)
Carbohydrate Analogue used	Glucose or Lactose derivatives with/out a thiolated oligonucleotide on Silver NPs
NP Absorption Investigations	Atomic Absorption Spectrophotometer (indirect quantave cell absorption) and confocal laser microscopy (SPR at 488nm to visualise NPs)
Measured Outcomes	
• Cellular Uptake Profiles with/out oligonucleotide linker	A549 cells demonstrated significantly enhanced selectivity to lactose modified NPs over Glc-NPs (75% vs. 15% NP absorption rate). No difference in uptake was seen the the physiological L929 cell line (compared to control). With the addition of the oligonucleotide group, There was no significant difference in uptake between Glc- (increase of 20%) and lactose-NPs (decrease of 335) at 6 hours (however still significant at 12 and 1- hour
• Confocal Microscopy of cells	Lactose-NPs were seen to enter A549 cells more than any other NP type, localizing in the cytoplasm after 5 hours.

Study Strengths	Several varying structural configurations for NPs were used, whilst also including a physiological cell line and 'naked' NP as controls.
Study Limitations	No distinction between cell uptake and absorption noted, with indirect method of calculating the percentage of NPs absorbed leaving room for error and inaccuracies (considering each wash needed to be completely added to reach this evaluation). Whilst confocal microscopy images were clear, images of single isolated cells with small number of NPs cannot be used to confirm enhanced cell entry via surface changes.
Conclusions	Addition of an oligonucleotide linker has improved NP absorption through a change in zeta potential, with carbohydrates significantly enhancing cellular absorption in the A549 cancer cell line.

Xiong et al. [71]	*2011*
Cell lines	HeLa Cell line (Cervical cancer)
Carbohydrate Analogue used	2-deoxy-D-glucose in Ferric Oxide NPs (10nm)
NP Absorption Investigations	Prussian Blue Staining for localisation & Calorimetric assays for quantification of absorbance Competitive binding methods & GLUT1 inhibition
Measured Outcomes	
• Competitive Binding & GLUT1 inhibition	Significant decrease in Prussian blue staining in/on cells when adding GLUT1 inhibitor
• Glc-NP absorbance using UV calorimetric assays	Increased absorbance of Glc-NPs when compared to controls, when compared at differing concentrations
Study Strengths	Demonstrates increased Glc-NP absorbance at different concentrations compared to control at similar concentrations; with decreased absorbance during GLUT1 inhibition confirming its role in potential absorbance
Study Limitations	Dispersion of NPs in water produced aggregates with average diameters of 156.2nm – inferring that other potential route of entry (macrocytes) may be undertaken. No suitable GLUT1- deficient cell lines as controls.
Conclusions	GLUT1 plays a role in Glc-NP absorbance with increased uptake when compared to non-Glc NPs. Interestingly bending efficacy of glucose conjugation by 40%.

Wang et al. [72]	2012
Cell lines	Hep2 cell line (hepatoma cells)
Carbohydrate Analogue used	4-deoxy-glucose terpolymer attached to chemotherapeutic agents (Ara-C and FUDR)
NP Absorption Investigations	FITC Fluorescence with Confocal Laser scanning microscopy
Measured Outcomes	
• Cell Absorption with FITR	Confirmed cell absorption with imaging of all different glycosylated aggregates utilised in the study
Study Strengths	Use of 'control' non-glycosylated NPs as comparisons; reviewing different drug concentrations
Study Limitations	Micelle aggregation with 500nm particular size & no GLUT1-deficient cell lines as control No attempt to review endocytic pathway that undertakes, with no GLUT-1 inhibition to identify transporter No differentiation between cell adsorption and actual cell uptake
Conclusions	Increased cellular adsorption associated with glucose functionalized chemotherapy
Jiang et al. [73]	2014
Cell lines	bEnd.3 cell (endothelial cell line to act as blood brain barrier), RG2 glioma cell line & Mice Models
Carbohydrate Analogue used	2-deoxy-D-Glucose (attached to PEG group 71nm polytrimethylene carbonate NP with paclitaxel)
NP Absorption Investigations	Quantitative cell absorption with flow cytometry (cell line and spheroid models). Fluorescent Dye (LysoTracker Green and Hoechst) with confocal microscopy, together with endocytosis inhibitor use.
Measured Outcomes	
• Cell Viability/ Toxicity	Increased early and late cell apoptosis when compared to non-Glc NPs (17.12 and 11.21% increase resp.) in cell line assays. Spheroid models decreased by 58.7% 7 days after use of glycosylated NPs (vs. 17.5% with non-Glc NPs).
• Cellular Absorbance (Competition Assay)	Cellular absorbance was reduced when a preceding free glucose solution was added, saturating GLUT carriers
• Endocytic Mechanism	Cytochalasin B (inhibits endocytosis of GLUT) showed statistically significant reduction, together with CPZ (clathrin inhibitor) and filipin/ genistein (caveolae-mediated endocytosis). Interestingly

	DMA (microtubule disrupting agent) did not decrease internalisation; hence macro-pinocytosis did not play a significant role
• In vivo distribution/ efficacy	1.94 fluorescence intensity of Glc NPs in tumour vs. non-Glc NPs, with decreased non-specific accumulation in reticuloendothelial systems, with a significantly stronger tumour inhibition
Study Strengths	Endocytic mechanisms of entry identified using several inhibitors targeting different endocytic pathways Attempted to review depth penetration of NPs Confirmed increase uptake in animal models
Study Limitations	Glc-NP remained at the periphery of spheroids at greater depths No dose variations in investigations (especially when confirming toxicity profile, depth of penetration) Despite use of flow cytometry, distinction between adsorption and uptake not made.
Conclusions	Glc-NP is taken up by cells via Clathrin- & caveolae-mediate endocytic pathways; with improved depth of invasion and can cross the blood brain barrier
Barbaro et al. [81] *2015*	
Cell lines	BxPC3 cells (human pancreatic ductal carcinoma)
Carbohydrate Analogue used	2-deoxy-D-Glucose (functionalized with 2.7nm Iron Oxide NPs)
NP Absorption Investigations	TEM imaging for cellular localization • GLUT-1 inhibition (polyclonal antibodies) Graphite Furnace Atomic Absorption Sepctrometry (quantify NP uptake)
Measured Outcomes	
• Comparisons with non-glucose coated NP	Glc-NP cellular content 1.5 higher than non-glucose coated NP at 6 hours Glc-NP uptake followed time-dependent kinetic saturation (typical of carrier-assisted internalization); whilst non-glucose NPs followed linear dose-dependent absorbtion
• NP uptake with GLUT1 inhibitor	41% reduction of cellular absorbance of glucose coataed NP
Study Strengths	Varying concentrations of NPs tested, commenting on rate of absorbance non-glucose coated NPs act as control
Study Limitations	Diameter of NPs permitted facilitated diffusion across a more porous cancer cell membrane

Conclusions	Glc-NP increases cellular absorbance, with a time-dependent kinetic saturation noted
Hu et al. [74]	*2015*
Cell lines	MCF-7 (breast carcinoma) and THP-1 cell lines (monocytic leukemia)
Carbohydrate Analogue used	1-thio-D-glucose attached to AuNPs (20nm diameter)
NP Absorption Investigations	Scanning Electron Microscopy & Inductively Coupled Plasma Mass Spectrometry (ICP-MS)
Measured Outcomes	
• Pharmacokinetics on different starvation times	MCF-7: Glc-NPs had highest absorption concentration at 1 & 2 hours, that tailed off to coincide with non-Glc-NP concentrations at 3 and 4 hours. Different starvation intervals (1,2 and 3 hours), with higher Glc-NP absorption seen in the 2-hour starvation period. THP-1: Glc-NPs shown a lower concentration compared to non-NPs at 2 hours, however significantly iraise at the 1- and 4-hour mark. In the starvation experiment (same time intervals), higher uptakes were seen after 1 hour of measurement (at 1- and 2- hour starvation intervals).
• Intracellular localisation	SEM image of cell demonstrates intra-cellular NPs
Study Strengths	Utilised a 'control' NP for comparisons as well as detailed time-interval experiments (illustrating changes from 1 to 3 hours into the experiment).
Study Limitations	Glucose moiety was attached flush to the NP, likely to limit the complex's interactions with GLUT transporters. PEG insertions, as commented by the authors, also be responsible for cell absorption, with no further isolated PEG-NP to witness its effects (rather than combined Glc-NP with a further 'PEG variable' as was the case). Both cell lines utilised were cancer cell lines, permitting limited scope of comparisons to be made, given that their uptake mechanisms and transporter expression were not explored.
Conclusions	Limited meaningful conclusions can be drawn given variability in NP complexes and lack of appropriate further standards to compare with (such as a PEG-NP complex)
Venturelli et al. [75]	*2015*
Cell lines	MCF7 and MDA-MB-231 cell line (breast cancer)
Carbohydrate Analogue used	2-deoxy-glucose to Cobalt Ferrate NPs (27nm diameter)

NP Absorption Investigations	Pearl Staining, Conflocal Fluroscence Imaging and Focal Ion Beam- SEM techniques GLUT1 inhibition (siRNA transfection)
Measured Outcomes	
• Intracellular Entry	Increased cell absorbance of GLc-NPs in cancer cells with enhanced GLUT1 expressionc(3.8 times higher at concentrations of 5mM NPs)
• GLUT1 Inhibition	Reduced cell absorbance of Glc-NPs by 78-81% in respective cell lines
Study Strengths	FiB-SEM techniques allows appreciation of depth of NP within the cell (3 dimensional images attached) Differing concentrations utilised when reviewing cell absorbance of Glc-NPs
Study Limitations	Whilst differing cell lines were used to compare GLUT vs. GLUT deficient absorptions; the varying deficiencies in cell mechanisms outlined makes direct comparisons difficult, although GLUT1 inhibition does bring appreciation of its role in cell absorbance. Use of non-Glc-NPs would have allowed for better comparisons. Confocal fluorescence imaging shows a minute number of NPs stained on/ within the cell (not convincing)
Conclusions	Potential for increased cell absorbance of Glc-NPs, although this is not the most convincing article
Shan et al. [76]	*2017*
Cell lines	MDA-MB-231 and MCF-7 breast cancer
Carbohydrate Analogue used	2-deoxyglucose attached to DMSA coated supermagnetic iron oxide (150nm)
NP Absorption Investigations	Prussian blue staining (in vitro) and MRI imaging (in vivo localisation) UV Colorimetric assays (quantification)
Measured Outcomes	
• In vitro localisation	Following 2-hour incubation; higher uptake in GLUT-1 expressing MDA cell line
• In vivo localisation	non-Glc-NP was not detected in cancer on MRI imaging; with contrasting results for the Glc-NP
Study Strengths	Array of in vitro and in vivo testing with different receptors (glucosamine) and control present (non-Glc)
Study Limitations	No differentiation between cell adherence and uptake, with unspecific attempts of uptake quantification

Conclusions	Potential scope for use of such NPs in imaging (however drawback of requiring 2 MRI sequential scans)

Panzarini et al. [77]	*2017*
Cell lines	HeLa cell line (epithelioid cervical cancer)
Carbohydrate Analogue used	3-amino-1-diethylene glycol-α- D-glucopyranoside or Glucosamine (attached to 150nm PDA NPs)
NP Absorption Investigations	Fluoroscopy & Laser scanning Confocal Microscopy (quantum dots), SEM-EDX, ICP-MS (directly by silver concentration absorptied) & GF-AAS (indirectly through silver concentration)
Measured Outcomes	
• Cellular Absorbance and targeting (Competition assay)	Improved fluorescence of Glc-NP (compared to control and glucosamine NPs), with a 46-fold and 1.3-fold higher absorbance rate. GLUT1 inhibition resulted in decrease absorbance.
• NP intracellular localisation	NP localised in endo/lysosomal organelles
Study Strengths	Improved vision of NPs with the use of quantum dot technique. Demonstrated increased tumour selectivity in mouse models
Study Limitations	No distinction between cell absorption vs. cell uptake through their uptake investigations. SEM images attached demonstrated a single cell with NP absorbance does not give definitive conclusions of uptake.
Conclusions	Glc-NP increases cellular absorbance, with a time-dependent kinetic saturation noted

Park et al. [78]	*2017*
Cell lines	Hep-2 cells
Carbohydrate Analogue used	Glycol-chitsan-coated AuNPs
NP Absorption Investigations	Flow cytometry analysis (DiI dye) & confocal laser scanning microscopy
Measured Outcomes	
• Cellular Absorbance	Uptake was tested using media with different glucose concentrations; with a decrease in cell adherence as glucose solute concentrations increased.
• In vivo cell targeting	1.35-fold higher fluorescence intensity when using Glc-NPs

Study Strengths	In vitro and in vivo testing, demonstrating increase tumor selectivity
Study Limitations	No differentiation between absorbance vs uptake, whilst commenting on 'uptake efficiency' using flow cytometry – this distinction was not made or inferred throughout the text. Did not specify glucose moiety structure used. Whilst glucose saturation solutions were experimented with, the lack of non-cancerous cell lines prevents meaningful comparisons of NP absorbance when comparing with non-Glc NPs.
Conclusions	Addition of glucose moiety improves tumor selectivity and targeting with chemotherapy
Asik et al. [79]	*2017*
Cell lines	MDA-MB-231, MCF-7 cancer and MCF-10A normal breast line
Carbohydrate Analogue used	2-amino-2-deoxyglucose with cobalt ferrite magnetic NPs (211nm)
NP Absorption Investigations	Transmission Electron micrographs and ICP-OES (quantification)
Measured Outcomes	
• Selective targeting and accumulation of NPs	TEM with Prussian blue staining showed higher NP uptake, with significant quantitative uptake values noted. Concentration dependent feature of internalizations noted for both Glc and non-Glc-NPs
Study Strengths	Use of controls in terms of both non-Glc NPs and normal breast tissue cell lines for comparisons. Selected TEM imaging in paper more convincing of intracellular uptake than other studies.
Study Limitations	Investigations used do not differentiate between absorbance and actual uptake.
Conclusions	Increased tumour selectivity/ absorption evident with Glc-NPs
Singh et al. [80]	*2017*
Cell lines	Human keratinocyte cell line and A431 cell line (human epithelial carcinoma)
Carbohydrate Analogue used	'Glucose' ($C_6H_{12}O_6$) with AuNPs (2nms)
NP Absorption Investigations	Fluorescence Confocal Microscopy & Flow cytometry (quantification) with GLUT1 inhibitor (gentisein)
Measured Outcomes	

• Cell absorbtion at varying membrane potentials	The uptake of Glu-NPs was significant more in A431 cell line (2.8-fold increase); with 60% increase in GLUT1 expression in this cell line. This is further demonstrated with decreased uptake in genistein inhibition.
Study Strengths	Appreciates differences of cell surface absorption and actual cell uptake: reference made to FSC vs SSC and utilised in dissociating adsorption from uptake. Utilises control non-Glc-NPs for comparisons as well as differing cell lines with varying GLUT1 expression.
Study Limitations	Size of NPs discussed (<2nm) is extremely small; whilst evidence of cell uptake is confirmed, enhanced permeability of cancer cell membranes are likely to contribute to its uptake by passive diffusion. No mention of fluorescence dye use to aid in differentiating location of NP
Conclusions	Cell absorption related to GLUT1 receptors and membrane potential independent when considering Glc-NPs; investigating cell uptake (rather than just adsorption)
Motei et al. [82] **& Dreifuss et al.** [83]	*2016 & 2018*
Cell lines	A431 (H&N cancer), A549 (non-small cell lung cancer), LNCaP (prostate cancer) and 3T3 fibroblast cell lines.
Carbohydrate Analogue used	2 & 1-amino-2-deoxy-glucose attached via PEG group (7) to AuNPs (20nm diameter)
NP Absorption Investigations	Fluorescence Microscopy (Rhodamine B) & Scanning Electron Microscope for qualitative analysis, whilst Atomic Absorption Spectroscopy was used for quantitative analysis. GLUT1 inhibition (cytochalasin) and endocytosis inhibition (chlorpromazine, nystatin and amiloride).
Measured Outcomes	
• Glucose Attachment Optimised	Motei et al. showed *in vitro and in vivo* that 2-Glc-NP had a three-fold increased uptake compared to 3-Glc-NP and 6-Glc-NP whilst a five-fold increase in 1-Glc-NP; also confirmed in vivo mouse models with Atomic Absorption Spectro.
• NP Cell Absorption	16.3% increase in glycosylated NP absorption compared to non-Glc NPs (statistically significant). Lower 1-Glc-NP absorption compared to 2-Glc-NP; with cell lines expressing increased GLUT1 showing a positive correlation with 2-Glc-NP absorption.
• Endocytosis pathway investigations	More than one uptake mechanism partook in NP uptake: depending on cell type. In A549 cells, Clathrin mediated endocytosis inhibition significantly decreased NP internalization for 2-Glc-NP by a relative uptake decrease of 75%. Nystatin inhibiton of calveolae also contributed to decreased NP uptake (25% in A431 cells).

Study Strengths	First study to delineate optimal carbon attachment to glucose moiety to ensure efficient NP internalization. Re-affirmed endocytic pathways undertaken on NP binding to GLUT. Utilises several different cell types to re-affirm 2-Glc-NP association with increased GLUT presence.
Study Limitations	In Motei et al. NP concentration for in vitro incubation was not stated in 'Methods' section, whilst in Dreifuss et al. this was stated as 30mg.ml; a very high concentration leading to questions over aggregation and/or uncertainty in technique. No direct quantitative measurement tools to identify the net NP internalization and percentage of remaining NPs that are adsorbed to the cell surface.
Conclusions	
Shamsi et al. [85] *2018*	
Cell lines	MCF-7, MD-MDA-231 and MC4-L2 cell lines (breast carcinoma, varying estrogen receptor selectivity)
Carbohydrate Analogue used	2-deoxy-D-glucoe attached to hydroxyapatitie NPs with doxorubicin (Chemotherapeutic agent)
NP Absorption Investigations	MTT assay to determine cell killing effect utilizing different coated NPs Cell absorbance via technetium attachment and use of SPECT gamma camera in vitro and in vivo samples
Measured Outcomes	
• Cell toxicity	Decreased viability when utilizing Glc-NPs vs. non-Glc NPs (highest in MC4-L2 line: 50.2% vs. 71.8%)
• Cellular Absorption	Increased absorbance seen with technetium labelling when compared glycosylated doxorubicin and technetium molecules.
Study Strengths	Good control standards selected for comparisons (doxorubicin without NP attachment in cell toxicity analysis; isolated technetium in cell absorption investigations).

Study Limitations	MTT assay acts as an indirect method of reviewing improved cell line uptake, with chemotherapeutic agent relying on cell division to instigate its cell killing effect, hence varying results across different cell lines. Whilst technetium investigations attempt to demonstrate increased cell absorbance with glycosylation, there is no distinction between uptake and absorbance. Furthermore, the given single P value for this test does not explain which tested molecules show 'significance' given there is at least 6 statistical tests performed. The in vivo investigations were only commented on in the discussion section with no actual results tabulated, save for a blurred diagram; with no contributions made to any of the paper's points.
Conclusions	Limiting evidence that glycosylation improves NP tumor uptake in breast cancer cell lines
Cheng et al. [86]	*2018*
Cell lines	u-87 MG and SVG p12 cell lines (glial cells)
Carbohydrate Analogue used	1-Thio-B-D-glucose sodium salt solution
NP Absorption Investigations	Confocal Fluorescence Microscopy
Measured Outcomes	
• Glc-NP absorbance & Metabolism	Fluorescence comparisons showed absorbance of Glc-NPs in cancer cells with GLUT overexpression; whilst no fluorescence noted in NPs without glucose moieties. Interestingly when mixed with cytoplasmic enzymes – a drop in fluorescence levels confirmed glucose metabolism
Study Strengths	Use of 'control' NPs for comparison and differing Glc-NP concentrations for investigation with fluorescence microscopy. Novel idea of measuring cell cancer aggression through metabolism.
Study Limitations	Fluorescence microscopy imaging demonstrates very sparse amounts of NPs present and not very convincing. When performing glucose metabolic reactions; enzymes were extracted from cells, which is disappointing as it does not convey any information regarding actual cell uptake and intra-cellular metabolism.
Conclusions	Increased Glc-NP absorption with potential of measuring its metabolism as means of cancer aggression
Pia et al. [84]	*2018*
Cell lines	HeLa cell line (cervical cancer)

Carbohydrate Analogue used	3 different glucose functionalized monomers conjugated at C1 or C6 glucose positions, used either as RAFT copolymers or single chain polymer NPs (10nm diam)
NP Absorption Investigations	Fluorescence-activated cell sorting (FACS) using DTAF dye and confocal laser scanning microscopy
Measured Outcomes	
• Quantitative NP Absorption	NPs with a free C1 position showed highest uptake, whilst NPs with conjugated or modified C1 moieties had reduced uptake (conjugated C1 NPs absorbed the least).
• Qualitative Confocal Imaging	2-d and 3-d imaging correlates quantitative findings above (found in suppl. material)
Study Strengths	Improved imaging with 3-dimensional figures allowing more accurate representation of NP subcellular localisation. Re-affirms importance of glucose C1 position in transporter uptake.
Study Limitations	FACS used was denoted to detect 'NP uptake', however there was no differentiation between uptake and absorption. There were sparse details regarding the methodology of how uptake was calculated, with no mentions of which scatterplots were utilised to arrive to the results stipulated.
Conclusions	Whilst limited methodology and results revealed to arrive to conclusions mentioned, further re-affirmation that C1 conjugation decreases uptake.
Sun et al. [87]	*2019*
Cell lines	MDA-MB-231 breast cancer cell line
Carbohydrate Analogue used	Glycol-chitosan coated AuNPs
NP Absorption Investigations	Transmission electron Microscopy Photo-acoustic Imaging of cells (Ultrasound)
Measured Outcomes	
• Cellular Absorbance	Photoacoustic imaging with ultrasound demonstrates increased cell absorbance when compared to its control (PEG-AuNP)
Study Strengths	Non-Glc NP control utilised as a comparator. Ultrasound imaging demonstrating depth perception to allow for more convincing images of potential cell uptake of NPs.
Study Limitations	No differentiation between cellular absorption to cell membrane and actual cell uptake Fluorescence microscopy images did not demonstrate convincing cell uptake
Conclusions	Ultrasound used for photo-acoustic imaging demonstrated increased Glc-NP absorbance

Yi et al. [88]	2019
Cell lines	MBA-MB-231 spheroids (breast carcinoma)
Carbohydrate Analogue used	C6 Glucose attached to PEG group onto AuNPs (20nm diameter) with SiRNA
NP Absorption Investigations	Flow cytometry with ALDEFLUOR staining kit (identify high aldehyde dehydrogenase expressing cells); with phloretin GLUT1 inhibitor & confocal microscopy.
Measured Outcomes	
• Cell absorption of NPs	Higher absorption of Glc-NPs compared to control NPs in both cell plates and spheroids. This was significantly reduced when using the GLUT1 inhibitor. Cells with ALDH-high expression (increased glycolytic needs) exhibited increased Glc-NP uptake than ALDH-normal cells.
Study Strengths	Interesting comparison of ALDH subtypes to further consolidate glycolytic pathways increasing GLUT1 expression. Use of spheroid models to attempt to create similar 'in vivo' structures.
Study Limitations	No differentiation between adsorption and cell uptake, with microscopy images showing NPs mostly around the cell periphery.
Conclusions	Highly metabolizing cancer cells allow more selective glycosylated NP targeting.
Li et al. [89]	2019
Cell lines	MDA-MB-231 (breast carcinoma), MCF-10A (breast epithelial cells) & T1 murine cell line (mammary carcinoma). BALB/c mice were tested as *in vivo* subjects.
Carbohydrate Analogue used	3-amino-1-diethylene glycol-alpha-D-glucopyranoside or glucosamine to PDA NPs
NP Absorption Investigations	Quantum Dot NP labelling and confocal microscopy (including use of GLUT1 inhibitor WZB117) NIR LASER irradiation and fluorescence confocal microscopy
Measured Outcomes	
• In vitro/ vivo targeting ability	46-fold and 1.3fold higher uptake of Glc-DEG NPs compared to non-Glc and Glucosamine coated NPs in vitro studies. MTT assays confirmed increased intracellular entry with enhanced cytotoxicity seen in the Glc-DEG NP group. A competition assay performed decreased Glc-NPs entry by >90% after 24-hour incubation of WZB117. In mice models, enhanced tumour absorption compared to other site distribution was seen with similar ratios when comparing the three NP categories. This distribution was most appreciated 8 hours NP injection.

• Intracellular localisation	Red fluorescence of NPs and green fluorescence for endosomes was seen to overlap with a bright yellow signal, pointing towards entry of Glc-NPs. With increased NIR laser time (1 min to 3 min), they attempted to demonstrate increased cytoplasmic presence (rather than remaining inside endosomes/lysosomes)
Study Strengths	In vivo and in vitro attempts to demonstrate increased specificity and uptake, utilizing a control non-Glc NPs as well as varying types of Glc-NPs (with/out DEG chain) and utilizing non-cancerous cell lines for comparison in vitro. Fluorescence changes (green to yellow) gave a better impression of NP internalization via endo/lysosomes.
Study Limitations	No differentiation between cell adsorption and cell uptake. Despite attempts at fluorescence, bright red NP fluorescent markings were still seen at the periphery of cells, making internalization conclusions questionable
Conclusions	In vitro and In vivo testing demonstrated improved NP accumulation in tumor cells upon glycosylation; with GLUT1 inhibition results hinting towards a GLUT1 endocytic pathway for these glycosylated NPs.
Wang et al. [90]	*2020*
Cell lines	bEnd.3 cell line (glioblastoma)
Carbohydrate Analogue used	PEG stabilized Heptapeptide nanodisc with glycosylated threonine (50nm size)
NP Absorption Investigations	Forster Resonance energy transfer (FRET) method: DiO, DiI and DiD dyes used Inhibition of endocytic pathways using a range of endocytic inhibitors Fluorescence with confocal microscopy
Measured Outcomes	
• Endocytic Pathways	Chlorpromazine and hypertonic sucrose (Clathrin-related endocytosis) significantly reduces Glc-NP uptake Caveolae associated pathways were excluded (Philipin and genistein did not inhibit uptake)
• Intracellular trafficking	Fluorescence images showed endocytic localisation (early and late endosomes)
• Lysosomal exocytic pathways	GLUT4 vehicle pathways were used to excrete NPs; with fluorescence labelling (Rab8) and inhibition nocodazole reduced efflux

Study Strengths	Use of NP controls, different endocytic-linked and exocytic-linked inhibitors: defining appropriate cell uptake mechanisms. Fluorescent imaging attached is more in depth and convincing when compared to other studies
Study Limitations	It would have been interesting to compare cell absorption rates with those of non-cancerous cell lines using similar inhibition and fluorescence techniques.
Conclusions	Strong evidence of endocytic pathways involved in internalization of NPs in endosomes
Aslan et al. [91]	*2020*
Cell lines	MCF-10A (normal breast tissue0 & MCF-7 Cell lines (breast carcinoma)
Carbohydrate Analogue used	2-deoxy-glucose attached to Au loaded apoferritin (4.08nm diameter)
NP Absorption Investigations	Inductively Coupled Mass Spectrometry (ICP-MS) for quantitative uptake. Indirect measurement through apoptosis analysis using FITC apoptosis detection kit and flow cytometry.
Measured Outcomes	
• Evaluation of NP Absorption	Both non-Glc and Glc-NPs should time-dependent uptake in both cell lines. There was a higher uptake of Glc-NPs, albeit higher in the MCF-F cell lines.
• Evaluation of Apoptosis	Significant apoptotic rate was seen in MCF-7 cell lines (unaffected at MCF-10A) with long exposure times (72 hours) and high concentrations (1mg/ml)
Study Strengths	Use of physiological cell line and non-Glc NPs as standards for comparison. Measurements at different time intervals established a time-dependent uptake rate.
Study Limitations	Distinction between NP cell adsorption vs. internalization not made during study. NP diameter allows for passive diffusion of NPs, affecting cell absorption results.
Conclusions	Dual potential for NPs: enhanced CT imaging results together with triggering of apoptosis. Results also indicate high concentrations and incubation interval allows for selective tumour cell killing.